DIPLOMARBEIT

Experimental realisation and investigation of a six-photon symmetric Dicke state

Ausgeführt am
Institut für Quantenoptik und Quanteninformation
Österreichische Akademie der Wissenschaften

unter Anleitung von o. Univ. Prof. Dr. Anton Zeilinger

durch

Gunther Cronenberg
Alpenlandstraße 2
2380 Perchtoldsdorf

12. Juli 2009

Zusammenfassung

Derzeit können Quantensysteme nur bis zu bestimmten Größen und Komplexitäten beherrscht werden. Der Übergang zu höherdimensionalen und Mehrteilchen-Systemen ist ein notwendiger und herausfordender Schritt für Anwendungen. Das in dieser Arbeit präsentierte und auf linearer Optik basierende Experiment erlaubt die Generierung von Sechs-Photonen Dicke Zuständen. Der Aufbau erwies sich während der gesamten Meßdauer als außerordentlich stabil.

Aus den Meßergebnissen konnte der Überlapp (Fidelity) mit den gewünschten Zuständen bestimmt, sowie deren Verschränkung (engl.: genuine multipartite entanglement oder kurz GME) nachgewiesen werden. Darüberhinaus konnte gezeigt werden, dass dieser verschränkte Dicke Zustand als Ressource für kleinere, aber komplett unterschiedliche verschränkte Zustände dienen kann.

Neben einer ausführlichen Beschreibung des Aufbaues und der Charakterisierung wird der Einfluß von unvermeidbaren höheren Ordnungen auf diverse Meßgrößen betrachtet.

Auch die Anwendbarkeit für die verschiedensten Quantenprotokolle, insbesondere für Quantennetzwerke wird gezeigt. Diese Protokolle sind Geheimnisteilung (Quantum Secret Sharing), Quantenteleklonen und Offene Quantenteleportation.

Abstract

Today quantum systems can be controlled and worked with as long as the complexity in terms of particle numbers and their interactions is limited. Going to higher particle and qubit numbers is an essential and challenging step to overcome in the future. In this work an all-optical linear experiment for producing a six-photon Dicke state is presented, which proved to be extremely stable over time, as well as useful applications of it. Besides proving general multipartite entanglement and obtaining the state fidelity it was shown how to use this as a flexible resource for lower-dimensional entangled states, giving one the freedom to navigate through lower-dimensional state space.

Besides giving a detailed description, an extensive analysis of the setup was done where special focus was put on the aspects of higher-order emissions and their effects on various key characterisations like fidelity and visibility.

It was furthermore demonstrated that this six-photon state proves very useful for different quantum protocols such as quantum secret sharing, quantum telecloning and open-destination teleportation, again for a high number of involved parties.

This thesis is divided in five chapters:

- Chapter 1 gives a brief summary of definitions needed from quantum mechanics and the basics from quantum optics. The concept of entanglement is introduced and ways of its measurement and categorisation.
- Chapter 2 describes the physics behind the most important tools used for the state modification in our all-optical setup.
- Chapter 3 presents the motivation for the experiment and the actual layout of the setup with a detailed discussion on the individual components.
- Chapter 4 contains an analysis of the setup through simulations, done both analytically and numerically. Emphasis is put on higher-order effects on the measurement outcomes of the experiment.
- Chapter 5 presents the outcome of the experiment and the means of qualification and quantification of the states produced. Additionally it is demonstrated how different quantum protocols can be employed.

Contents

Chapter 1

Introduction

1.1 Quantum physics and quantum information

Quantum physics, developed in the early twentieth century, revolutionised physics, opened new fields and changed the way we think about nature. In quantum physics many new phenomena emerge which most of the time appear counter intuitive to the mind used to a classical world. But this led to a vast advance in philosophy as well as technology especially through the connection with physics from an information point of view [1]. Seeing what impact information technology has on today's society, the expansion of quantum physics into this field leading to quantum information theory will also have an impact where it is an ongoing progress in finding the limits as well as possible applications [2].

1.2 Quantum mechanics

1.2.1 States and their evolution

A physical system can be described by a state vector in a Hilbert space[1] $\mathcal{H}$. Depending on the system, it can be discrete or continuous, finite or infinite. Examples are the continuous, four-dimensional momentum of a free particle or the discrete energy levels of a bound electron. In the Hilbert space a basis $|i\rangle$ can be given, which is a set of linear independent vectors who span the Hilbert space. It allows to express any state vector $|\psi\rangle$ as a linear combination:

$$|\psi\rangle = \sum_i \alpha_i |i\rangle , \quad |\psi\rangle \in \mathcal{H}. \tag{1.1}$$

Quantum mechanics (QM) is a linear theory from which the *superposition principle* follows: any superposition of states is again a valid state.

[1] This chapter cannot give a complete introduction and as there are many good introductions it will not even try.

When looking at the dynamics of a system, there exist two different but equivalent pictures [3]: the Heisenberg picture, where the time evolution is put into the operators and the states are not time dependent and the Schrödinger picture where the states evolve with time. This time evolution is given by a unitary matrix $U = \exp(iHt)$ where H is the Hamiltonian generating the evolution.

Density matrices

When discussing entanglement as in Section 1.4 it is useful to use the notation of *density matrices* also called *density operators*. Density operators allow to write states conveniently which are not pure but mixed, i.e. in an ensemble. These are states which are not in a superposition but a statistical mixture with different probabilities in some states: $\{(|\psi_i\rangle, p_i) \mid i = 1, ...N\}$. A density matrix ρ for a pure state[2] $|\psi\rangle \in \mathbb{C}^n$ is defined as

$$\rho = |\psi\rangle\langle\psi|, \quad \rho \in \mathbb{C}^n \otimes \mathbb{C}^n. \tag{1.2}$$

The density operator is always a positive operator and $\mathrm{Tr}(\rho) = 1$ holds.

The density matrix contains all information about the system and by calculating the trace one sees that the system is in a pure state if $\mathrm{Tr}(\rho^2) = 1$, whereas it is mixed if less than 1.

1.2.2 Measurements

To get information out of a system one needs to perform a measurement. This reading out of information modifies the state. A measurement on a state is described by a Hermitian measurement operator or observable[3], which is written as a matrix M_k acting on the state[4] $|\psi\rangle$:

$$|\psi_k\rangle = \frac{M_k |\psi\rangle}{\sqrt{\langle\psi| M_k^\dagger M_k |\psi\rangle}} = \frac{M_k |\psi\rangle}{\sqrt{p_k}}. \tag{1.3}$$

The measurement operators fulfil a completeness relation and the outcome probability for a specific value is given in form of p_k. In quantum mechanics only orthogonal measurements can be clearly differentiated, that is with total confidence.

In a simple projective measurement, the commonly known and used form of measurements, the idempotent[5] projector P acts on the state and collapses the state into an eigenvector of the operator with the probability given by the corresponding eigenvalue. The eigenvectors of the projector form an orthonormal basis.

Besides this special kind of measurements the more general description is given by Positive Operator Value Measurement (POVM), which are mentioned for completeness, but they will not be discussed here [4].

[2]The definition for other states exists as well but is omitted here.
[3]The hat commonly indicating an operator is omitted further on.
[4]This formalism is easily extendible for the density matrix formalism.
[5]Idempotent: $PP = P$ and it follows that the eigenvalues are ± 1.

1.2.3 Qubits

The word *qubit* is formed from "quantum bit" to express the expansion of the classical concept of a bit into the quantum world. A classical bit, on which our information society is built, is a unit of binary information that can be either 0 or 1. A qubit is a quantum state with the orthonormal basis $|0\rangle$ and $|1\rangle$, also called computational basis. However with the special property being a cornerstone of quantum mechanics that all superpositions are also valid state vectors:

$$|\psi\rangle = \alpha\,|0\rangle + \beta\,|1\rangle\,, \quad \alpha, \beta \in \mathbb{C}, \quad |\alpha|^2 + |\beta|^2 = 1. \tag{1.4}$$

When measuring the qubit in the computational basis, the possible outcomes are $|0\rangle$ and $|1\rangle$, each with the probability of the square of their factor: $|\alpha|^2$ respectively $|\beta|^2$. α and β are also called (probability) amplitudes and the condition in Equation 1.4 guarantees their normalisation.

Mathematically the structure of a qubit is a representation of the SU(2) group. Opposed to the bit with only two possible values a qubit can be any of infinitely many different states. This means that a qubit can contain infinitely much information, at least theoretically, but there is no way to use this. Measuring the qubit can have only two outcomes and leaves the state collapsed so stored information cannot always be fully read out.

1.2.4 Fidelity

To characterise experimentally produced states many different useful measures exist, for example the purity or the entropy [4]. Another, very often used one is the *fidelity*. For pure states it is defined as the overlap of the actual given state $|\phi\rangle$ with the theoretically expected $|\psi\rangle$, defining a distance between them:

$$F = |\langle\phi, \psi\rangle|^2, \tag{1.5}$$

with $0 \leq F \leq 1$ and $F = 1$ only if $|\phi\rangle = |\psi\rangle$. When written between an arbitrary density matrix ρ and a pure state $|\psi\rangle$ the equation reads: $F = \langle\psi|\,\rho\,|\psi\rangle$ or between two density matrices ρ and σ:

$$F = \left(\mathrm{Tr}\left[\sqrt{\sqrt{\sigma}\rho\sqrt{\sigma}}\right]\right)^2. \tag{1.6}$$

The fidelity thus satisfies the conditions for a positive measure which is also symmetric under the exchange $|\phi\rangle \leftrightarrow |\psi\rangle$.

1.3 The photon as qubit system

The photon, a gauge boson predicted by quantum electrodynamics (QED), is a massless spin-1 particle described by its wavelength λ, position and polarisation state. While the last is a discrete variable, the other two are (in general) continuous.

As any massless spin-1 particle has only transversal polarisation, the helicity can only be plus or minus one corresponding to right and left circular polarisation but of course any linear combination exists. There are many physical systems which can be described by a qubit system. Photons are often used as realisation by exploiting the two possible polarisation modes. This is done by encoding information into the polarisation degrees of freedom. The horizontal $|H\rangle = (1,0)^T$ and the vertical $|V\rangle = (0,1)^T$ polarisation form a natural basis and the polarisation $|\mathcal{P}\rangle$ of a photon can be described by any superposition of the two:

$$|\mathcal{P}\rangle = \alpha \begin{pmatrix} 1 \\ 0 \end{pmatrix} + \beta \begin{pmatrix} 0 \\ 1 \end{pmatrix}, \quad \alpha, \beta \in \mathbb{C},\ |\alpha|^2 + |\beta|^2 = 1. \tag{1.7}$$

There are also other commonly used bases, namely the so called plus-minus (P, M or $+, -$) and the circularly polarised (R, L or $\circlearrowright, \circlearrowleft$) basis:

$$P = \frac{1}{\sqrt{2}}(H + V), \quad M = \frac{1}{\sqrt{2}}(H - V), \tag{1.8}$$

$$R = \frac{1}{\sqrt{2}}(H + iV), \quad L = \frac{1}{\sqrt{2}}(H - iV). \tag{1.9}$$

The photon is a very convenient quantum system because one of the main obstacles to overcome in experiments with entanglement is decoherence. It is the process of information leaking to the surrounding environment and leads to disentangling states (see Section 1.4 and [4]). But luckily the photon is rather easy to handle and more resistant to decoherence than atoms or other heavily interacting systems. Photons are also optimal for communication schemes[6]. The trade off on the other hand is that photons are rather hard to store to have them handy at need, so it is required to have them produced just in time. Besides that, photons do not interact with each other directly, only their bosonic nature can be used to achieve an indirect interaction. An implementation is the famous Hong-Ou-Mandel interference [5], which is needed in quantum computing where two-qubit gates are necessary to build complete algorithms.

Another way to implement a photonic qubit is the Dual Rail mechanism [6]. Here information is encoded with one photon in two spatial modes: The logical qubit is 1 if there is a photon present otherwise it is 0. This offers also the possibility to go to higher dimensions (and leaving the Dual Rail), with the qudit, a logical d when d photons are present. The formalism behind this scheme is the Fock formalism: A state is characterised by its number of photons $|n\rangle$. Photons are added to a mode by applying the creation operator $a^\dagger |n\rangle = \sqrt{n+1}\,|n+1\rangle$ and removed by the annihilation operator $a\,|n\rangle = \sqrt{n}\,|n-1\rangle$. From successive application of the creation operator one obtains:

$$|n\rangle = \frac{\left(a^\dagger\right)^n}{\sqrt{n!}}\,|0\rangle\,. \tag{1.10}$$

[6]This fact is used already since the time of mankind, only nowadays we are increasingly efficient, using single photons.

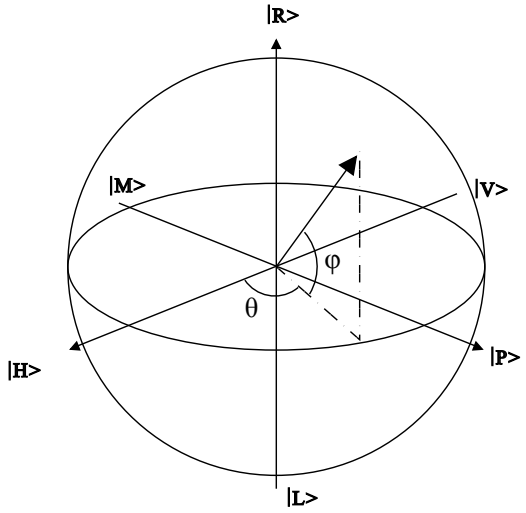

Figure 1.1: The Poincaré sphere is the unit sphere, on which all pure qubit states lay. The three different, orthogonal bases $H/V, P/M$ and R/L are shown and the parametrisation with θ and ϕ of an arbitrary state.

The number operator is given by $n\,|n\rangle = a^\dagger a\,|n\rangle$.

1.3.1 Poincaré sphere

As a qubit is a representation of the SU(2) group, it can be geometrically represented as a point on the *Poincaré sphere* as displayed in Figure 1.1. This corresponds to the qubit having two degrees of freedom, where the chosen representation includes the two parameters θ and ϕ, which uniquely define the state:

$$|\psi\rangle = \cos\theta\,|0\rangle + e^{i\phi}\sin\theta\,|1\rangle, \tag{1.11}$$

with $\theta \in [0, \pi]$ and $\phi \in [0, 2\pi[$.

An orthonormal basis is represented on the sphere by two points laying opposite of each other, which are often indicated by lines. The axes shown in Figure 1.1 are the bases $H/V, P/M$ and R/L described in Section 1.3.

The Poincaré sphere is outside the optics community called the Bloch sphere, but then the angles θ and ϕ are parametrised differently and their origin is relocated [7].

1.3.2 Measurement basis

Often the computational basis is set to correspond with the H/V basis. This means the identification of $|0\rangle$ ($|1\rangle$) with $|H\rangle$ ($|V\rangle$) is made. Measuring the qubit in the H/V basis corresponds to a projection of the state onto the Z axis in the Poincaré sphere. Similar the P/M and R/L bases project onto the X and Y axes.

The expectation value of measuring in one of these bases is calculated as follows:

$$x = \langle H|\,\rho\,|H\rangle - \langle V|\,\rho\,|V\rangle = \mathrm{Tr}(X\rho) \tag{1.12}$$
$$y = \langle +|\,\rho\,|+\rangle - \langle -|\,\rho\,|-\rangle = \mathrm{Tr}(Y\rho) \tag{1.13}$$
$$z = \langle R|\,\rho\,|R\rangle - \langle L|\,\rho\,|L\rangle = \mathrm{Tr}(Z\rho) \tag{1.14}$$

with the following matrices, which are just the Pauli matrices $\sigma_{x,y,z}$:

$$X = \begin{pmatrix} 0 & 1 \\ 1 & 0 \end{pmatrix}, \quad Y = \begin{pmatrix} 0 & -i \\ i & 0 \end{pmatrix}, \quad Z = \begin{pmatrix} 1 & 0 \\ 0 & -1 \end{pmatrix}. \tag{1.15}$$

1.4 Entanglement

According to Schrödinger, *entanglement* is the essence of quantum mechanics. The term entanglement was coined by Schrödinger in 1935 [8]. His work was a direct response to Einstein, Podolsky and Rosen (EPR) [9], who had published a paper featuring the famous EPR-Paradoxon earlier that year. In their work, the authors came to the conclusion that quantum mechanics might not be complete. Still it was not very discussed by the general community until John Bell showed 1964 [10] that reality, locality and quantum mechanics cannot be fulfilled at the same time. As a line of argument he used a system that is entangled thus producing a setting which can discriminate between a quantum mechanical and a local, realistic theory.

Among all new and strange phenomenas that emerge from quantum mechanics, entanglement is one of the most curious and worthwhile studying. Entanglement is a property of a many-particle system when knowledge of some information on one side infers knowledge of some information on the other side as well. It is instructive to look at some examples, the most famous two-party states are the Bell states, named after John Bell, who showed that their correlations are stronger than are allowed by a local, realistic theory:

$$\left|\Phi^{\pm}\right\rangle = \frac{1}{\sqrt{2}}\left(|00\rangle \pm |11\rangle\right),$$
$$\left|\Psi^{\pm}\right\rangle = \frac{1}{\sqrt{2}}\left(|01\rangle \pm |10\rangle\right). \tag{1.16}$$

It should be noted that $|\Psi^-\rangle$ is antisymmetric when exchanging particle one and two whereas the other three Bell states are symmetric. So $|\Psi^-\rangle$ belongs to a singlet and the others form a triplet accordingly to: $2 \otimes 2 = 3_S \oplus 1_A$.

Imagine that one pair, for example $|\Phi^-\rangle$ gets distributed among two parties, the first photon to A and the second to B. If Alice at A measures her photon she immediately knows the polarisation of Bobs photon at B to be $|0\rangle$ if she measured $|0\rangle$ and $|1\rangle$ otherwise. The four Bell states are also maximally entangled. As a

consequence without knowing the measurement outcome of A the state at B is maximally mixed. This can be seen formally when performing a partial trace over A on the systems density matrix $\rho_{AB} = |\Psi^+\rangle\langle\Psi^+|$:

$$\rho_B = \mathrm{Tr}_A(\rho_{AB}) = \frac{1}{2}\begin{pmatrix} 1 & 0 \\ 0 & 1 \end{pmatrix}. \tag{1.17}$$

This is the density matrix of a maximally mixed state being either in $|0\rangle$ or $|1\rangle$, with probability $\frac{1}{2}$ each. There are no coherence terms in the off-diagonal elements.

The properties of the system can be understood such that the information about the state is not localised. The system is also not factorisable into different lower-dimensional states which will be discussed in the next section.

Decoherence

The enemy of entanglement is *decoherence*, which was already briefly mentioned. Coherence refers to the general possibility of interference. Decoherence leads into disentangling a state and originates from interactions with the environment. But as such interactions are uncontrollable most of the time, one loses information about the actual state. Each interaction can be described as a measurement where the result is not recorded. While coherences of the state disappear, the state becomes entangled with the environment. The isolated state thus evolves from being in a superposition to a mixture. For larger systems interactions with the environment are more likely resulting in faster decoherence. But the loss of coherences, at heart of many quantum effects, is the reason for our macroscopic world to appear classical. Detailed information about the interaction with the environment which also includes the classical concept of dissipation can be found in [4].

1.4.1 Bipartite entanglement

When looking at a two-qubit system with particle A and B and assuming a pure state, the state vector looks as follows:

$$|\psi\rangle = \sum_{i,j=0}^{1,1} \alpha_{i,j} |ij\rangle, \quad |\psi\rangle \in \mathcal{H}_{ij} = \mathcal{H}_i \otimes \mathcal{H}_j. \tag{1.18}$$

The state is entangled if there is no way of writing it in the factorised form

$$|\psi_S\rangle = \sum_{i=0}^{1} \alpha_i |i\rangle \otimes \sum_{j=0}^{1} \beta_j |j\rangle, \tag{1.19}$$

which would mean the state is *separable*. Or rephrased: the state is entangled if it is not a product state of one-particle states. Nevertheless, their Hilbert space is the product space of the two single-particle Hilbert spaces as an entangled state can be expressed by a basis therein. An example is the already mentioned Bell state

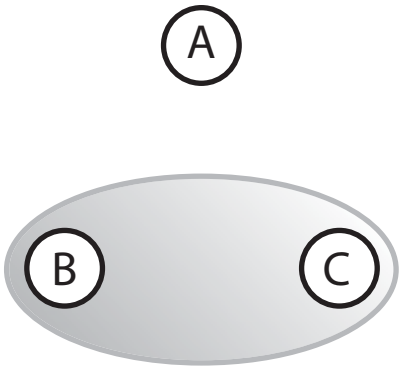

Figure 1.2: A three-party system is shown where the gray area indicates entanglement between party B and C. The whole system is hence biseparable as it can be split up into the subsystems A and BC but it is not possible to separate it in any other way.

$|\Phi^-\rangle = \frac{1}{\sqrt{2}}(|00\rangle - |11\rangle)$, for which no decomposition in form of Equation 1.19 exists as entangled states live in a part of the Hilbert space which cannot be reached by product states. It is not always possible to answer the general question of separability easily when an arbitrary state is given.

1.4.2 Multipartite entanglement

For a quantum system comprised of more than two particles entanglement is harder to quantify and to measure as there is no unique way to do so. It may well be that for example a three-particle system is not separable into a subsystem containing only particle C and one containing A and B: $|\psi\rangle_{ABC} \neq |\psi\rangle_{AB} \otimes |\psi\rangle_C$ but it may very well be separable into a subsystem of B and C and the subsystem of A: $|\psi\rangle = |\psi\rangle_A \otimes |\psi\rangle_{BC}$ (see Figure 1.2). With increasing number of particles, different possible separations exist, for a three-particle system there are four different separations. If none of the separations is possible the system is called *genuine multipartite entangled* (GME). An example for this class is the Greenberger-Horne-Zeilinger (GHZ) state as described below.

As there are numerous ways for a system containing more than two particles to be entangled many different measures exist to quantify entanglement, each one to be more suitable for a special purpose.

1.4.3 Equivalence classes

While for a two-party system entanglement is simple, for many-party systems there are different entanglement classes. This means that while the different classes share the properties mentioned above they do show different behaviour under certain operations. For a three-party system the two different classes [11] are formed by the W state [12] and the Greenberger-Horne-Zeilinger (GHZ) state [13, 14, 15],

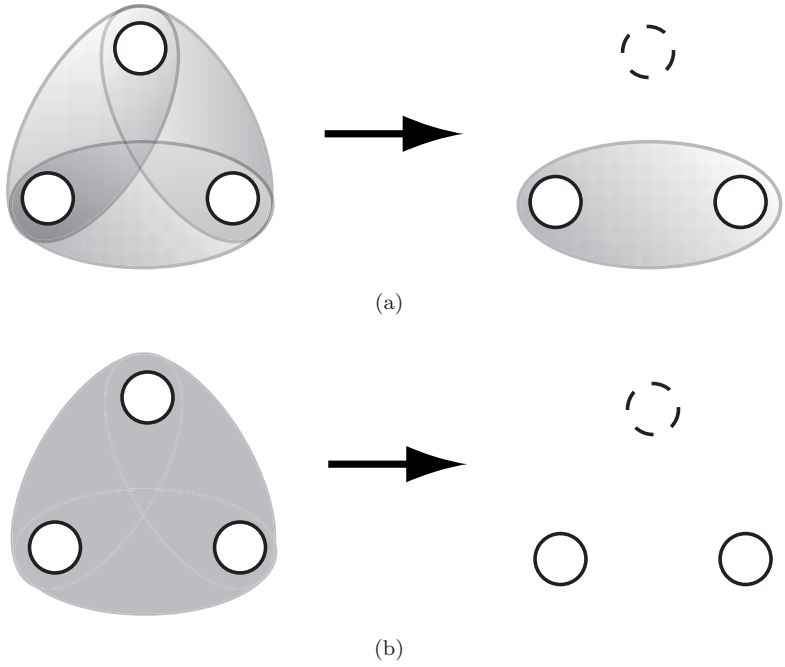

Figure 1.3: Examples for different entanglement classes: (a) shows a W state, where measuring the upper photon leaves the other two still entangled as indicated by the gray area. (b) measuring the upper photon in a GHZ state destroys all entanglement. The behaviour is equivalent for the other photons.

sometimes also called cat state referring to Schrödingers cat[7]:

$$|\mathrm{GHZ}\rangle = \frac{1}{\sqrt{2}}(|000\rangle_{ABC} + |111\rangle_{ABC}) \tag{1.20}$$

$$|\mathrm{W}\rangle = \frac{1}{\sqrt{3}}(|001\rangle_{ABC} + |010\rangle_{ABC} + |100\rangle_{ABC}). \tag{1.21}$$

It can be shown that a GHZ state cannot be transformed into a W state by a LOCC operation nor the other way round. LOCC is a protocol with operation that transform a state only by *local operation and classical communication* [16, 17, 18].

The difference is also manifested when one party gets traced out from a W state, an entangled Bell pair remains, whereas a measurement on the GHZ state removes all entanglement from the remaining two-qubit system (see Figure 1.3). In that sense the W state is called more robust against photon loss than the GHZ.

For higher-party systems more equivalence classes show up, but so far a full theoretical categorisation is a pending task receiving a lot of attention.

[7]Schrödingers cat can be written as a very high n GHZ state with the correspondence of $0 \rightarrow$ life and $1 \rightarrow$ death.

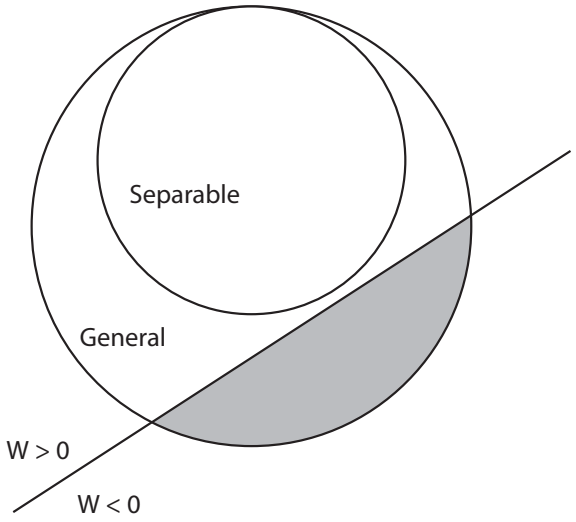

Figure 1.4: The convex state space of the separable states is embedded in the general state space. A projective measurement witness separates the general state space through a flat hypersurface such that the separable states are found on one side only, accordingly to the requirements in Equation 1.22.

1.5 Entanglement witnesses

For the quantification of entanglement different measures are introduced like *entanglement cost* and *relative entropy of entanglement* [19, 20]. Another kind of measure are *entanglement witnesses*. A witness operator $\mathcal{W}$ is constructed in such a way, that it fulfils the following constraints:

- For all separable states the witness should be positive: $\mathcal{W} > 0$.
- For a given entangled state the witness should be negative: $\mathcal{W} < 0$.

This ensures that if the witness is negative, the state is entangled, whereas a positive witness does not grant separability. Given a separable density matrix the witness is calculated by taking the trace: $\mathrm{Tr}(\mathcal{W}\rho) > 0$.

1.5.1 Projective measurement witnesses

Very commonly used witnesses are the *projective measurement witnesses*, they are constructed with a given entangled state $|\psi\rangle$ in mind (as demanded above) on which they are projected (hence the name):

$$\mathcal{W} = \alpha \mathbb{1} - |\psi\rangle\langle\psi|, \quad \alpha \overset{\max}{=} |\langle\phi_{BS}|\psi\rangle|^2, \tag{1.22}$$

with α being the maximal overlap of ψ with all biseparable states ϕ_{BS}. This construction ensures the satisfaction of the imposed conditions.

The state space is a convex set as any superposition of states from the space is again a state in that space. In this state space the separable states form a (again) convex subset B_S of the full space. There, all pure states lay on the boarder of B_S. The witness divides the state space by a flat hypersurface with states in the one part giving a positive witness and a negative one in the other part, as can be seen in Figure 1.4. When all separable states are in the positive part this gives a witness satisfying the conditions in Equation 1.22. It can be shown that for every entangled state such a witness can be found.

As can be seen from Equation 1.22, the construction connects in a very natural way the projective measurement witness with the fidelity described in Section 1.2.4.

1.5.2 Spin-squeezing witnesses

More sophisticated witnesses are the *spin-squeezing witnesses*, or short SSW [21]. Squeezing refers to the redistribution of quantum fluctuations between two non-commuting observables under the conservation of the minimum uncertainty product. In phase space for example the reduction in one parameter, the squeezing, results in the increase of the other parameter in such a way that the total area is preserved.

Spin squeezing is present when in a spin system the variance of one spin component normal to the mean spin is smaller than the standard quantum limit [22].

The spin-squeezing witnesses are constructed on the basis of two-qubit correlations. One advantage is that using such a witness, the number of local measurement settings can be drastically reduced which allows experiments for higher-dimensional states in the first place.

One example is the following witness suitable for the n-particle Dicke states which will be discussed in more detail in Section 5.1.1:

$$\mathcal{W}_{SS} = J_x^2 + J_y^2, \tag{1.23}$$

with the collective-spin operator

$$J_i = \frac{1}{2}\sum_{k=1}^{n} \sigma_i^{(k)} \quad (i = x, y, z), \tag{1.24}$$

k being the qubit label and n the number of qubits of the state. The result of the squaring contains the summation of all possible $n(n-1)/2$ two-qubit correlations and the squares of spin operators which lead with:

$$\sigma_i^{(k)} \cdot \sigma_i^{(k)} = \mathbb{1}, \quad k = 1, \ldots, n, \quad i = \{x, y\} \tag{1.25}$$

to:

$$J_i^2 = \frac{n}{4} + \frac{1}{2}\left(\sigma_i^{(1)}\sigma_i^{(2)} + \sigma_i^{(1)}\sigma_i^{(3)} + \ldots + \sigma_i^{(n-1)}\sigma_i^{(n)}\right). \tag{1.26}$$

As the total squared spin J^2 of a given state is conserved, measuring two components defines the third component. If two increase the third is lowered which corresponds to spin squeezing.

This kind of witnesses forms no longer a flat hypersurface in the state space like the projective measurement witnesses but a curved surface which adapts better to the separable state space.

Chapter 2

Quantum optics

In this chapter I will give an overview of tools needed in the experiment as well as of the methods used to describe it. The first part describes briefly the theoretical framework of classical and quantum optics, both linear and non-linear with focus on the concepts needed for understanding the experiment. In the second part the devices used in the experiment are introduced and their working principles explained.

2.1 Optics

2.1.1 Gaussian beam

The *Gaussian beam* is a three-dimensional solution of the paraxial Helmholtz equation in free space. Our laser beam can be described by such a Gaussian beam as the laser emits light into the TEM_{00} mode (see Figure 2.1), which is characterised by the E- and B-fields being perpendicular to the propagation and the field profiles having a Gaussian shape [23, 24].

The Gaussian beam is fully described by the minimal waist w_0 and the wavelength λ. Other important parameters of the beam propagating through a medium with refractive index n are the waist $w(z)$, which is defined as the transverse distance where the field drops by $1/e$ and the radius of the longitudinal wave front curvature $R(z)$. Both are dependent on the distance z (see Figure 2.2):

$$w(z) = w_0 \sqrt{1 + \left(\frac{z\lambda}{n\pi w_0^2}\right)^2}, \tag{2.1}$$

$$R(z) = z + \frac{1}{z}\left(\frac{w_0^2 n\pi}{\lambda}\right)^2, \tag{2.2}$$

$$z_0 = \frac{n\pi}{\lambda} w_0^2. \tag{2.3}$$

The Rayleigh length, z_0, is the position where the waist has the value of $\sqrt{2}w_0$

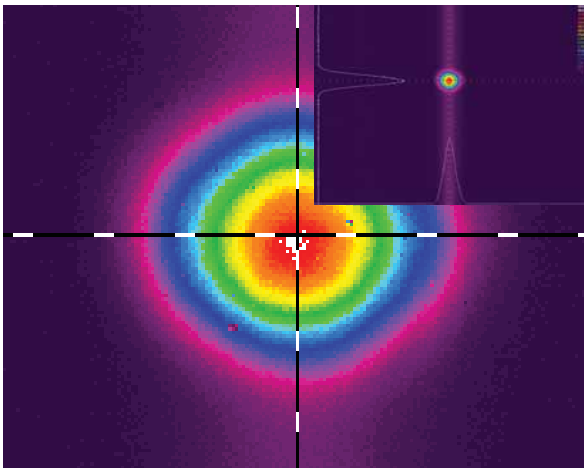

Figure 2.1: The Gaussian beam profile as seen by a Spiricon CCD camera. The width, containing $1/e^2$ of the total intensity, is $\sim 200\mu$m. In the corner the full image is shown as displayed by the camera. The vertical purple rays are just artefacts.

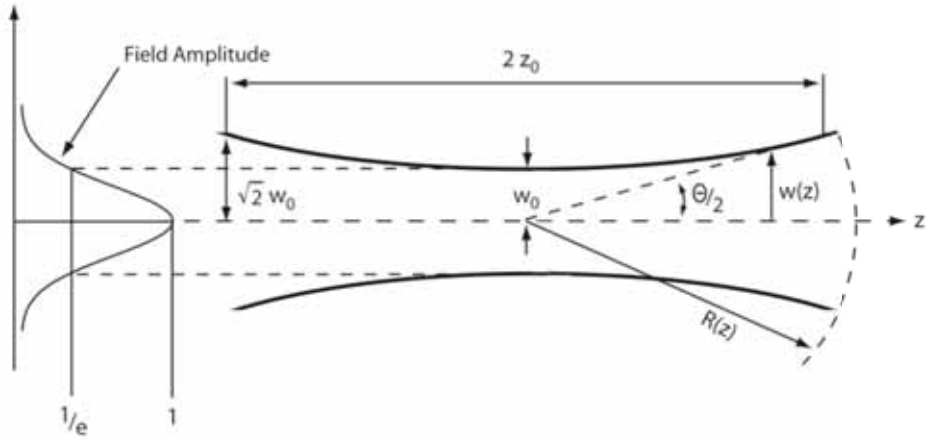

Figure 2.2: A Gaussian beam profile with the waist $w(z)$, the wave front curvature $R(z)$ as well as the divergence angle θ. Picture by R. Prevedel [25].

and the wave front curvature takes its maximal value $R_{\max}$. Within the circular area with radius $w(z)$ 86.5 % of the beam power is contained. The divergence angle θ of the beam, taken as the limit for very large z, is given by:

$$\theta = \frac{\lambda}{n\pi w_0} = \frac{w_0}{z_0}. \tag{2.4}$$

When sending a Gaussian beam through a lens, it still can be described by a Gaussian beam only with different parameters.

2.1.2 Matrix optics

Matrix optics is a very handy formalism to solve problems in the Gaussian optics regime within the matrix formalism. The methods are the same from the matrix optics describing the ray optics regime, only that here the matrices do not act on a vector but in an adapted way to the beam parameter q:

$$\frac{1}{q} = \frac{1}{R} - \frac{i\lambda}{\pi w^2 n}. \tag{2.5}$$

Given q, the waist is obtained by $\frac{1}{w} = -\frac{\pi}{\lambda}\mathrm{Im}\{\frac{1}{q}\}$ and the wave front radius $\frac{1}{R} = \mathrm{Re}\{\frac{1}{q}\}$. The parameter gets modified with the matrix elements A, B, C, D from the typical matrices used in the ray optic regime:

$$q_{\mathrm{out}} = \frac{Aq_{\mathrm{in}} + B}{Cq_{\mathrm{in}} + D}, \tag{2.6}$$

For example a thin lens with focus f is described by the matrix L and the free space propagation by the distance d by the translation matrix T:

$$L = \begin{pmatrix} 1 & 0 \\ -\frac{1}{f} & 1 \end{pmatrix}, \quad T = \begin{pmatrix} 1 & d \\ 0 & 1 \end{pmatrix}. \tag{2.7}$$

All the matrices can be multiplied in the corresponding order to the final matrix M which then can be entered in Equation 2.6:

$$M_{\mathrm{final}} = \ldots L_2 \cdot T_2 \cdot L_1 \cdot T_1 \tag{2.8}$$

2.2 Linear quantum optics

Linear quantum optics (LQO) derives its name from the fact that all covered operations are linear, i.e. all operations can be written as unitary operators:

$$|\psi\rangle_{out} = U\,|\psi\rangle_{in}\,, \quad U^\dagger U = \mathbb{1}, \quad U = e^{iHt}. \tag{2.9}$$

The formalism ensures that the photon number is conserved as the Hamiltonian commutes with the number operator: $[H, N] = 0$ [6]. Linear quantum optics describes many basic devices such as beam splitters, phase controls and general one-qubit gates. Furthermore it has been shown that LQO suffices to employ a quantum computation scheme [26].

2.2.1 Half- and quarter-wave plates

Half- and *quarter-wave plates* are used for changing the polarisation state of photons which corresponds to one-qubit transformations in the polarisation encoding scheme. They are made of (commonly uniaxial) birefringence crystals and use the fact of different refractive indices for different polarisations. They are cut in such a way that their optical axis is perpendicular to the incoming beam. Light with

polarisation parallel to the optical axis, which is the fast axis, travels with the group velocity $v_{\text{fast}} = \frac{c}{n_f}$ where as perpendicular polarised light travels with $v_{\text{slow}} = \frac{c}{n_s}$. This results in a phase shift for the two polarisations along the fast and slow axis. The phase shift contains a global part for both polarisation that is of no importance in most setups and will be omitted here. The other part is a relative phase θ originating from the different velocities. The action of the wave plate on the polarisation along the fast $P_f = (1,0)^T$ and slow axis $P_s = (0,1)^T$ is given by the following matrix[1]:

$$T(\theta) = \begin{pmatrix} 1 & 0 \\ 0 & e^{i\theta} \end{pmatrix}, \quad \theta = \frac{2\pi L}{\lambda}\Delta n, \tag{2.10}$$

where the phase θ is depending on the crystal length L and the difference in the refractive index Δn. The matrix acts on the polarisation state $|\psi\rangle$. For a generally orientated wave plate the incoming beam can be expressed in the basis of the wave plate having two components along the fast- and the slow axis. This corresponds to a basis rotation

$$R(\phi) = \begin{pmatrix} \cos\phi & \sin\phi \\ -\sin\phi & \cos\phi \end{pmatrix}, \tag{2.11}$$

which rotates the beam coordinates into the basis of fast and slow axis. It should be noted that the angle ϕ here is the physical angle by which the optical axis is rotated, not to be confused with the angle in the Poincaré sphere which is just 2ϕ. The full action of a wave plate oriented at the angle ϕ is now described by

$$U_{\text{WP}}(\phi,\theta) = R(-\phi)T(\theta)R(\phi) \tag{2.12}$$

which corresponds to a basis rotation, the phase delay for the slow axis and rotation back into the old basis again. This unitary matrix is also obtained from the following Hamiltonian:

$$H_{\text{WP}} = \theta e^{i\phi} a_H^\dagger a_V + \theta e^{-i\phi} a_V a_H^\dagger \tag{2.13}$$

Half-wave plate

Here the thickness of the crystal is chosen such that the delay of the polarisation along the slow axis is a natural multiple of $\frac{\lambda}{2}$. That is described by Equation 2.12 with $\theta = \pi$. Applying a half-wave plate results in turning the state vector about π around the optical axis laying in the plane spanned by $|H\rangle$ and $|P\rangle$ in the Poincaré sphere.

As an example, with the optical axis set to $\frac{\pi}{4}$, the state $|H\rangle$ gets transformed to $|V\rangle$.

[1] All kinds of different definitions can be found for this matrix, some are more symmetric, but they differ again only by a general phase.

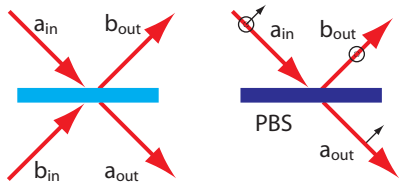

(a) (b)

Figure 2.3: (a) shows a beamsplitter with two input (a_{in}, b_{in}) and two output modes (a_{out}, b_{out}). (b) displays the action of polarising beam splitter on one input mode a_{in}. The horizontal polarisation, indicated by the small arrow, is transmitted, the vertical one, indicated by the ring, gets reflected into the mode b_{out}. The behaviour is equivalent for the other input mode b_{in}.

Quarter-wave plate

The working principle of the quarter-wave plate is identical to the one of the half-wave plate, except that the thickness is now a natural multiple of $\frac{\lambda}{4}$. This is equal to setting $\theta = \frac{\pi}{2}$ in Equation 2.12. Similar in the Poincaré picture the quarter-wave plate rotates the state vector by $\frac{\pi}{2}$ around the optical axis. For example a quarter-wave plate with ϕ set to 45° changes the polarisation from horizontal to right handed circular $|H\rangle \rightarrow |R\rangle$.

2.2.2 Beam splitters

A *beam splitter* (BS) is a probabilistic device and has two spatial input modes a_{in}, b_{in} and two spatial output modes a_{out}, b_{out}. The description is analogous to wave plates, demonstrating the conceptual correspondence between the dual rail description and polarisation encoding [6]. Where wave plates have polarisation modes as input, beam splitters act on spacial modes.

The beam splitter is characterised by η which denotes the probability of a photon entering in mode a_{in} to be found in the output mode a_{out} (see Figure 2.3(a)). Formally the action of a beam splitter can be written as follows [27]:

$$U_{bs} = e^{iH_{bs}\theta}, \quad H_{bs} = e^{i\phi}a^\dagger b + e^{-i\phi}ab^\dagger, \tag{2.14}$$

where the unitary operator acts on the two input modes a_{in} and b_{in}. The transmission of the BS is determined by $T = \eta = \sin^2\theta$ whereas the reflection is $R = 1 - T = \cos^2\theta$.

Most of the time one sets $\phi = \frac{\pi}{2}$ (by applying a general phase) which results into U taking the following form:

$$U = \begin{pmatrix} \cos\theta & \sin\theta \\ -\sin\theta & \cos\theta \end{pmatrix} \tag{2.15}$$

As an example the effect of a balanced 50:50 beam splitter, i.e. $\eta = 0.5$ (together with a global phase) is:

$$a_{\text{in}}^{\dagger} \rightarrow \frac{1}{\sqrt{2}}(a_{\text{out}}^{\dagger} + b_{\text{out}}^{\dagger}), \tag{2.16}$$

$$b_{\text{in}}^{\dagger} \rightarrow \frac{1}{\sqrt{2}}(a_{\text{out}}^{\dagger} - b_{\text{out}}^{\dagger}). \tag{2.17}$$

This action is equivalent to applying σ_x, which is a Hadamard gate, one of the basic gates in quantum computing.

Physically a beam splitter can be realised in many different ways, for example by a crystal usually having the form of a cube assembled from two triangles with a layer in between having a certain thickness which results for part of the beam being reflected, part getting transmitted. The thickness can determine the splitting ratio. Another implementation are dielectric mirrors. Their splitting ratio can be strongly dependent on the wavelength in which case they can be used as dichroic mirrors. Another kind also found in our setup are fibre beam splitter where two fibres are brought together very closely which is done by fibres fusion; part of the wave from one fibre gets transmitted into the second fibre.

2.2.3 Polarising beam splitters

Polarising beam splitters, or short PBS, are similar to beam splitters except that the polarisation modes are not treated equally as the horizontal polarisation is transmitted and the vertical reflected (see also Figure 2.3(b)). The action on the $2_S \otimes 2_P = 4$ spatial and polarisation modes is:

$$\begin{pmatrix} a_{\text{out}}^{H} \\ b_{\text{out}}^{H} \\ a_{\text{out}}^{V} \\ b_{\text{out}}^{V} \end{pmatrix} = \begin{pmatrix} 1 & 0 & 0 & 0 \\ 0 & 1 & 0 & 0 \\ 0 & 0 & 0 & -1 \\ 0 & 0 & -1 & 0 \end{pmatrix} \begin{pmatrix} a_{\text{in}}^{H} \\ b_{\text{in}}^{H} \\ a_{\text{in}}^{V} \\ b_{\text{in}}^{V} \end{pmatrix}. \tag{2.18}$$

Polarising beam splitters are often used as a parity check for two photons in the incoming modes, as only both output modes are populated if the they share the same polarisation [28]. Using only one input mode, a PBS together with a quarter- and a half-wave plate can perform a general polarisation analysis as the PBS projects a state onto the Z axis.

The physical implementation is similar to the beam splitters only that material has to be chosen for which the splitting ratio differs for different polarisations.

2.3 Non-linear quantum optics

Very interesting phenomenas can only be described by *non-linear quantum optics*. In general the photon number is not conserved anymore as opposed to the linear case described before.

The relation between the electric field and the dielectric polarisation is linear for most materials: $P_i(t) = \chi_{ij} E_{j(t)}$, but for non-linear materials the relation can be written as an expansion of the field strength:

$$P_i = \chi^{(1)}_{ij} E_j + \chi^{(2)}_{ijk} E_j E_k + \chi^{(3)}_{ijkl} E_j E_k E_l + \cdots , \tag{2.19}$$

where the $\chi^{(2)}$ term produces the non-linear three mode mixing and is called Kerr non-linearity.

As the non-linearities are very weak for most materials, it was thought until the second half of the twentieth century, that all optical effects could be described by linear optics. That was until the development of the laser, who could eventually provide the high intensities needed for the non-linearities to be significant, decisively proving the existence of phenomena dependent on the intensity.

2.3.1 Second harmonic generation

The up-conversion or *second harmonic generation* (SHG) is a process in a non-linear crystal that converts the laser beam at a given wavelength λ_{in} and produces photons at half the wavelength $\lambda_{out} = \frac{\lambda_{in}}{2}$. This is a degenerate case of the sum frequency generation (SFG), where the two incoming beams have different wavelengths ω_1, ω_2 and they mix classically to a third, outcoming wave with frequency $\omega_3 = \omega_1 + \omega_2$. For the collinear case in which we are interested, the incoming waves are the constituents of one beam and therefore posses the same frequency $\omega_1 = \omega_2$ and polarisation. In an uniaxial crystal, only the versions *o-o-e* and *e-e-o* are possible, where *o* refers to an ordinary polarised beam and *e* to an extraordinary. Hence the upconverted photons have a different polarisation than the incoming. The phase matching condition, coming from the momentum conservation and the frequency condition from energy conservation are for any three wave mixing process:

$$\omega_3 = \omega_1 + \omega_2, \tag{2.20}$$

$$\overrightarrow{k}_3 = \overrightarrow{k}_1 + \overrightarrow{k}_2, \tag{2.21}$$

where $|\overrightarrow{k}| = \frac{2\pi n}{\lambda}$, with n being the refractive index. Due to the degeneracy it follows immediately that the refractive index for the incoming and outcoming wave must be the same. Hence, for SHG it is necessary that the crystal is cut and aligned in such a way, that the refractive index, who is dependent on the angle θ, fulfils $n_{o(e)}(\omega) = n_{e(o)}(2\omega)$.

2.3.2 Spontaneous parametric down-conversion

Spontaneous parametric down-conversion, or short SPDC [29, 30], is one of the workhorses for quantum opticians as it successfully allows for the generation of correlated photon pairs in large numbers [31, 32] that is unmatched by alternative approaches on atomic or solid state systems. The most commonly used crystals for

SPDC are potassium dihydrogen phosphate (KDP), lithium niobate ($LiNbO_3$) and beta-barium borate (BBO).

This effect relies on the non-linear connection between the electromagnetic field and the dielectric polarisation in non-linear materials which can give rise to annihilation of a high energy photon which produces two daughter photons called signal and idler for historical reasons. At higher fields the $\chi^{(2)}$ term in Equation 2.19 becomes significant, leading to the observation of SPDC whereas normally the higher orders can be neglected.

The process is described by the Hamiltonian in Equation 2.22, from which energy and momentum conservation follow similar to 2.20:

$$\begin{aligned} H &= g^* a_s^\dagger a_i^\dagger a_p + g a_s a_i a_p^\dagger, && (2.22)\\ \omega_p &= \omega_s + \omega_i, && (2.23)\\ \overrightarrow{k}_p &= \overrightarrow{k}_s + \overrightarrow{k}_i, && (2.24) \end{aligned}$$

where g in the interaction Hamiltonian is the coupling strength dependent on the crystal length L, the pump power and on the non-linear coefficient. The last equation is also called the phase-matching condition, in a crystal of finite length it is only approximately true and the spectral width of the two-photon state is of order $1/L$. This follows from the full spectral analysis, which yields for the two-photon state:

$$\begin{aligned} |\phi\rangle &= \int\int d\omega_1 d\omega_2 \delta(\omega_p - \omega_s - \omega_i) && (2.25)\\ &\times \operatorname{sinc}\left(\frac{L\Delta k(T,\omega_s,\omega_i)}{2}\right) a_s^\dagger(\omega_s) a_i^\dagger(\omega_i) |0\rangle . \end{aligned}$$

Parametric down-conversion comes in two types: In type-I the crystal is aligned such that the pump beam is extraordinary e polarised and the signal and idler photons are ordinary o polarised, whereas with type-II the pump photon is e polarised as well as the idle but the signal is o polarised. Figure 2.4(a) shows the type-II case: the H polarised photons are emitted into one cone and the V polarised photons into another cone where their angles depends on the angle θ_{pm} between the pump and the optical axis of the crystal. The correlated photons are always on opposite modes relative to the pump beam. At the intersection point of this two cones, it is not possible to tell from which cone the photon originates hence the photon pair is polarisation entangled. The entangled state obtained in the two spatial modes is

$$|\psi\rangle = \frac{1}{\sqrt{2}} \Big(|HV\rangle + e^{i\phi} |VH\rangle \Big)_{ab} \qquad (2.26)$$

in the spatial modes a and b. The two intersection points lay on a line which is perpendicular to the optical axis of the crystal. In a collinear setup, the optical axis is tilted such that the two cones only intersect in one point, resulting in the entangled pair being emitted into the same spatial mode: $a = b$.

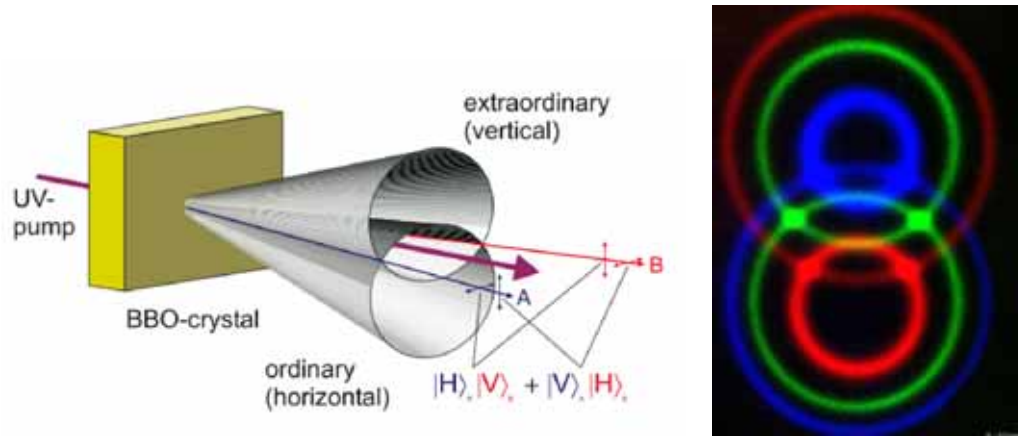

(a) (b)

Figure 2.4: (a) The type-II SPDC scheme. At the intersection of the two cones, the spatial modes A and B, the entangled states are obtained. (b) Three pairs of rings originating from the down-conversion can be seen. They were photographed with three shots taken with different filters such that each time only a specific wavelength was recorded. Picture by P. G. Kwiat and M. Reck.

For the type-I case, the pair of photons is emitted into the same cone with the same polarisation which can be either HH or VV. The cone is centred around the pump beam and the two photons are opposite on the cone. Following the argument from above at two opposite points one obtains the entangled state

$$|\psi\rangle = \frac{1}{\sqrt{2}} \left(|HH\rangle + e^{i\phi} |VV\rangle \right)_{ab} . \tag{2.27}$$

Through local operations on the states from Equations 2.26 and 2.27 any Bell state can be generated.

The pairs are not produced event-ready but randomly as already the name promises. For many application a true single photon source would be most convenient and the SPDC can provide an approximate heralded single photon source, where detection of a photon in one spatial mode signals the existence of a single photon in the other spatial mode.

Walk-off effects

During Type-II pair production in a finitely thin crystal a longitudinal and a transversal walk-off effect can be observed. They result from a pair being produced at a point such that the distance x has to be travelled before leaving the crystal again. The o- and the e-photon have different group velocities. The longitudinal walk-off results from this group velocity mismatch, where a time delay between the two photons linearly depending on x can be observed which reduces the indistinguishability between them and allows labelling if the time difference is

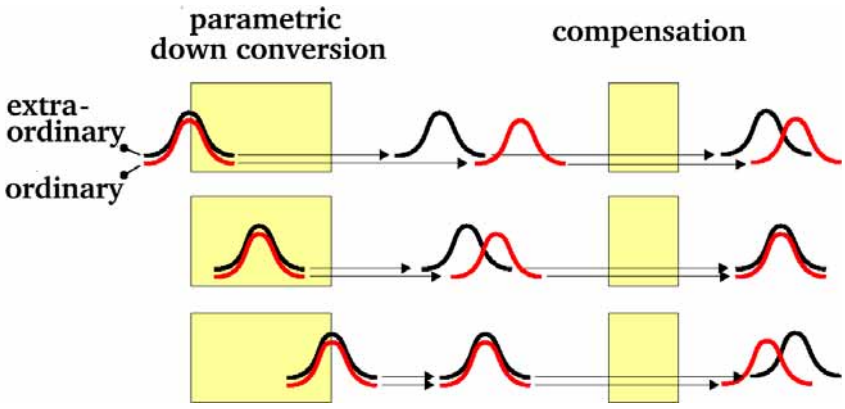

Figure 2.5: The compensation of the longitudinal walk-off for SPDC type-II achieved through a second crystal half the thickness with optical axis rotated by 90 degrees. Figure adapted from [33].

larger than the coherence time $\delta t > \tau$. This would mean that the entanglement of the photon pair is lost. To avoid this, indistinguishability needs to be restored. The effect can be compensated by another crystal of half the thickness with the orientation perpendicular to the first one (see Figure 2.5). It cannot compensate the time delay completely, only for a pair produced in the middle of the first crystal. But half of the photons being observed first will be horizontally polarised, the other half vertically so that no information about their polarisation can be concluded by the time of their arrival.

Similar the transversal walk-off originates from the different directions of the orthogonal polarised photons inside the crystal. The photons' transversal separation depends on x which, in the worst case, introduces a longitudinal separation larger than the photons' coherence length resulting in a defined labelling. Following the same idea from above, this can be avoided by placing a crystal half the thickness behind and the orientation of the optical axis antiparallel with respect to the one from the first crystal. The compensation also ensures in this case the indistiguishability and entanglement is restored. However, the mode with the diverted photons gets smeared out, resulting in a bigger spot size than the other polarisation. When coupling into fibre more of these photons are lost.

These two mentioned solutions compensate either the longitudinal or the transversal walk-off. For the simultaneous compensation an additional wave plate is need that is placed between the two crystals at an angle of 45 degrees. It interchanges the role of the horizontally and vertically polarised photons when they travel through the second crystal which now is oriented identically with the first one both effects are compensated.

There is no SPDC process happening in the compensation crystal due to the fact that the focus of the input beam is located within the first crystal. Thus the

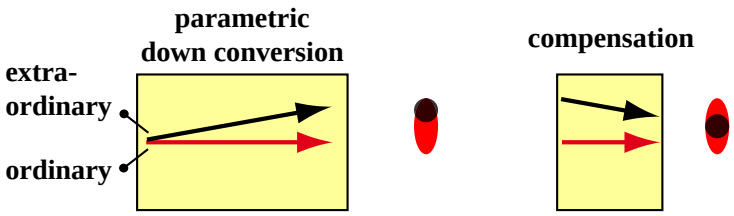

Figure 2.6: The compensation of the transversal walk-off for SPDC type-II achieved through a second crystal half the thickness with optical axis rotated by 180 degrees. As the pump is extraordinary polarised, it follows the black line. Down-converted *o*-photons do not get displaced and a *o*-photon produced at the beginning of the crystal is maximally separated from the *e*-photons. This results in a broader spot for the *o*-photons.

divergence of the beam is sufficiently large that the beam intensities are too low in the compensation crystal for any significant pair-production.

Chapter 3

The Dicke experiment

3.1 Motivation for the experiment

While new insights into the dynamics of entangled multi-particle systems are gained, various multi-qubit experiments have been performed [34, 35] with the main focus on producing GHZ [15, 36], W [37], cluster and graph states [38, 39, 40, 41].

The primary aim of this experiment is to produce an entangled six-photon state namely the symmetric Dicke state. Entanglement of a high N-party state is desirable as it is absolutely necessary for quantum information and computation. Making their advantages usable in technical settings is only possible when one succeeds in controlling and understanding higher particle-number setups. In that sense this experiment tests how well we are prepared for the obstacles that lay ahead on this path.

As entanglement is a valuable resource, we also show the useability of the generated Dicke state for applications implementing diverse quantum information protocols like telecloning, open-destination teleportation and secret sharing bringing us a step closer to quantum networks. Not only is the state worthwhile on its own, it can also be used as a resource for creating lower-dimensional states which belong to different equivalence classes. It allows to flexibly choose between them without any experimental modifications.

Dicke states have been realised using different physical systems such as atomic assembles, ion traps and in linear-optics setups, but only to a small qubit number with photons [42].

The Dicke state

The Dicke states are named after Robert Henry Dicke who introduced such a notion for molecular radiation processes [43]. A Dicke system can be treated as a two level system where the first level is called 0 and the excited level 1. The Dicke state $D_y^{(x)}$ then describes a system with y particles with x excitations with all possible

combinations having the same probabilities. This is the sum of all possible permutations of the state $\left|\bigotimes^x 1 \bigotimes^{y-x} 0\right\rangle$. The Dicke state composes of $\binom{y}{x} = \frac{y!}{x!\cdot(y-x)!}$ components, for the $D_6^{(3)}$ there are 20. In our case we identify the first level 0 with V and the excited level 1 with H:

$$D_6^{(3)} = \frac{1}{\sqrt{20}} \sum_P |HHHVVV\rangle_{123456} \,. \tag{3.1}$$

The Dicke states belong to a different equivalence class than the GHZ states.

3.2 The experimental setup

In this section the layout of the linear-optics setup used for the Dicke experiment is described and detailed information on each particular piece is given. A schematic view of the experiment is shown in Figure 3.1 and a photograph of it can be seen in Figure 3.2. Dealing with the high number of photons, it was necessary to use and align numerous optical elements, as done only by a few other experiments.

Laser

Our laser system from Coherent is built up by first a diode laser which pumps the solid state, frequency doubled Nd:Vanadate ($\mathrm{Nd:YVO_4}$) laser Verdi V-18. The frequency doubling is achieved through second harmonic generation within a LBO crystal which is heated to 150° C to satisfy the correct phase matching conditions. As the name reveals the single output frequency is at 532 nm with a power of 18 Watt. The green light pumps the high power Titanium Sapphire Laser (Ti:Sapphire) named Mira HP shown in Figure 3.3. The high power Mira is mode-locking and produces pulses with a duration of 200 fs with a repetition rate of 76 MHz. Mode-locking means that the different existing modes inside the cavity are interfering in such a way that instead of a continuous wave (CW) leaving the cavity with a constant intensity only pulses with a higher maximum intensity at the same average intensity are emitted periodically. This is achieved by locking the phases of the different modes together [24]. The advantage of working with a pulsed laser is for one that the non-linear effects described in Section 2.3 are dependent on the intensity of the laser. The average output power for the CW and the pulsed case are the same, which results in a higher peak power for the pulsed case. This enhances the probability of the average pair production in the SPDC process needed for a non-negligible observation. Furthermore, using pulses allows a convenient identification and grouping of the detected photons as long as the repetition rate of the laser is smaller than the detectors and logics resolution. If two detectors fire within the same time interval such that our coincidence logic clicks, we know that the two primary photons were produced during the same pulse.

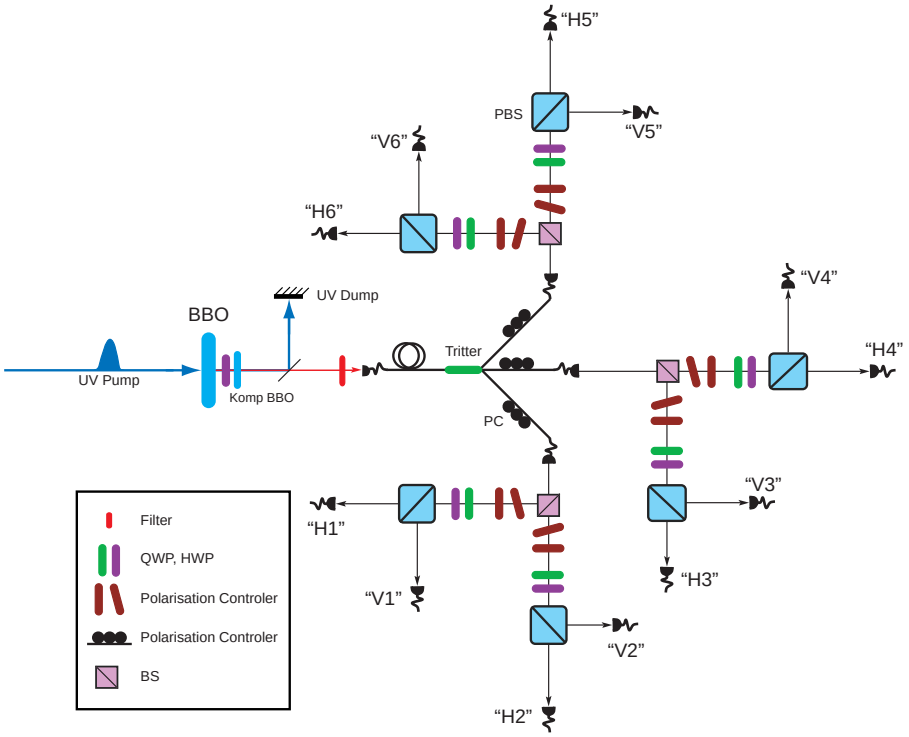

Figure 3.1: The layout of the Dicke experiment showing all optical components. The produced IR photons are being split up into multiple modes and afterwards their polarisation is analysed. For a detailed discussion see text.

A CW laser has ideally one wavelength with no band width but for a pulsed laser only a centre wave length can be given and the band width is determined by the pulse length. The centre frequency of our laser is tuneable and was set to 808 nm during our Dicke experiment which is in the infrared (IR) regime. Our band width was 10 nm and the beam horizontally polarised.

Up-conversion

The up-conversion is done in a lithium triborate (LiB_3O_5) or short LBO crystal, which is a negative biaxial crystal [44]. Its was 2 mm thick and anti-reflection coated to minimise back scattering. It produced 404 nm light from the incident 808 nm beam coming from the laser. During the setup, we noticed a drop in the count rates which had its origin in the burning of the anti-reflection (AR) coating of the LBO. To prevent this during the measurements we mounted the crystal on a motorised translation stage, which continuously moved the crystal perpendicular to the beam such that the illuminated focus point on the crystal changed. The

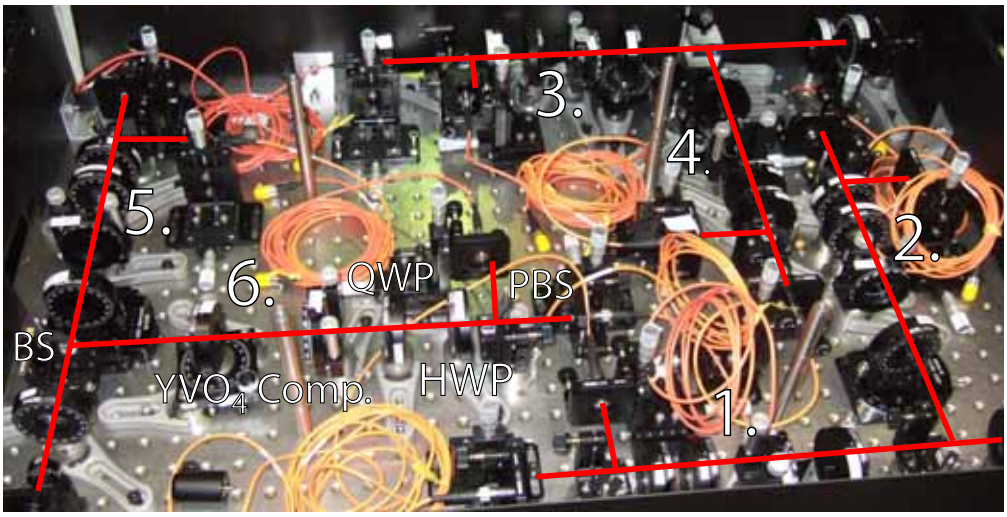

Figure 3.2: The picture shows the Dicke setup from the outcoupling of the single-mode fibres onwards. It was mounted on a breadboard located on top of the optical table. First, each spatial mode is split up by a BS. The resulting six spatial modes are numbered in the photograph. The components are labelled for the sixth arm, which contains two phase-compensating crystals and the polarisation analysis through the combination of QWP, HWP and a PBS each. The orange multi-mode fibres are not yet coated and connected to the detector.

n_o	1.66113
n_e	1.54603

Table 3.1: Refractive indices of the negative uniaxial ($n_o > n_e$) BBO crystal for λ=808 nm [44].

frequency doubled UV pulses had an average CW-power of 1.4 Watt. The power was very stable with fluctuations by only 1-2% over 30 hours.

As can be seen in Figure 3.3, cylindrical lenses were employed behind the LBO to correct for unicircular beam shape which originated from the birefringence of the up-conversion process.

At this stage, the beam contains both UV (404 nm) and IR (808 nm) light. But as the next step is also producing IR at the same wavelength the beam is cleaned beforehand from the IR light originating from our laser with the aid of two dichroic mirrors, deflecting it onto beam dumps. Additionally the mirrors shown in Figure 3.3 are highly reflective for UV-light but not for IR, resulting in a further cleaning of the beam.

Down-conversion

The source of our entangled photons at 808 nm is realised by SPDC as described in Section 2.3.2 (see also Figure 2.4). In our case we used a beta barium borate ($\beta - BaB_2O_4$) or short BBO, crystal with a thickness of 2 mm in a collinear type-II

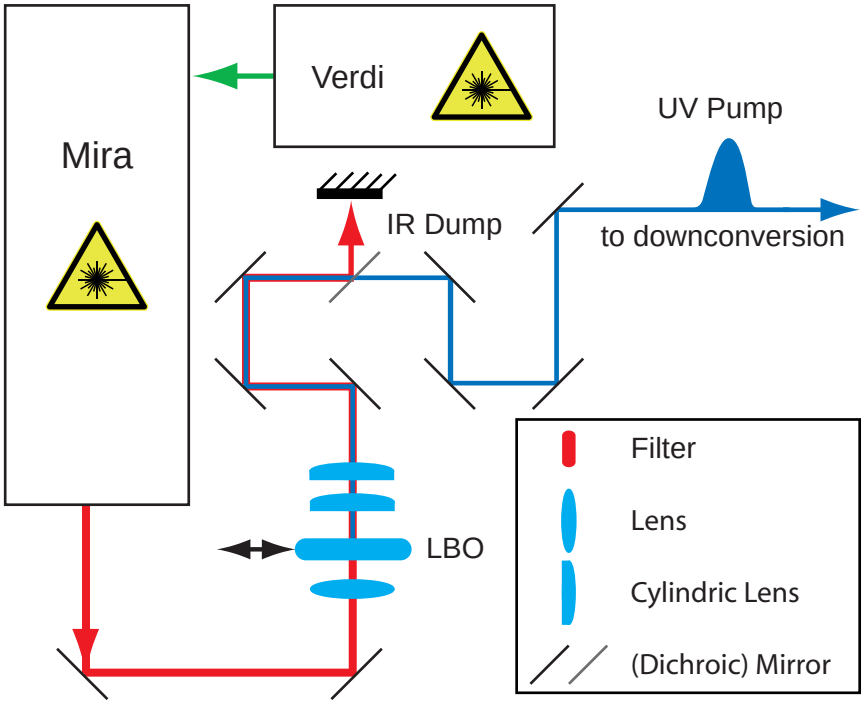

Figure 3.3: The up-conversion part of the setup displaying the path of the laser beam from the lasers through the LBO where the up-conversion takes place and cleaning from the IR light. The beam is then sent to the down-conversion part.

setup (see Figure 3.1). This means that the two down-conversion cones are only intersecting at one point instead of two. Pairs of down-converted photons with no individual transverse momentum are found in this specific spatial mode, populated also by the UV light.

Additionally, walk-off effects in the BBO crystal are observed as described in Section 2.3.2. While the ordinary polarised beam does not get diverted, the extraordinary beam does, which results in a displacement depending on the location of the down-conversion. Maximal displacement happens for photons created at the beginning of the crystal while none can be seen for ones created at the end. To compensate this so-called longitudinal and transversal walk-off effects, a half-wave plate at 45 degrees and another BBO crystal with half the thickness is placed behind with the optical axis aligned like the first BBO. At the half-wave plate, the horizontally polarised photons become vertically polarised and vice versa. The second BBO hence compensates the two walk-off effects.

At this point we have again the UV light at 404 nm together with IR light at 808 nm in the same mode. This time the UV light needs to be removed which is done by a dichroic mirror placed into the beam path. It reflects the UV light to a beam dump but transmits the IR light.

	Mode 1	Mode 2	Mode 3	Total [%]	Total [dB]
Output	36.57%	38.77%	24.66%	98.64	0.059

Table 3.2: The fibre-splitter output efficiency at 808 nm for the fibre tritter which splits one mode into three. The imbalanced ratio is explainable with the fact that it was designed for a different wavelength (see text).

Coupling

At this stage the photons are coupled into a single-mode fibre (with the aid of a single-mode lens) and are propagated to the rest of the setup which was located on top of the setup described so far. The advantage (besides satisfying physical size limitation in the laboratory) is that the single-mode fibre filters out all spatial modes except a specific mode. This spatial mode filtering is essential for the fidelity as otherwise noisy photons enter the setup.

Additionally, before coupling into the single-mode fibre a narrow high-transmittivity interference filter with $\Delta\lambda = 3$nm and centred at 808 ± 1.5 nm is placed in front of the fibre coupler. This spectral selection is necessary as the filtering removes time information from when the pair was created. The coherence time is now much bigger than the pulse duration, so upon detection it is not possible to differentiate between different pairs created by the same pulse. At this point the photons are now temporally, spectrally and spatially indistinguishable.

Due to the walk-off effects (see Section 3.2) that are responsible for smearing our the spatial mode of the vertically polarised photons, more horizontally polarised photons than vertically polarised photons get coupled into the single-mode fibre. This results in an H/V imbalance. Obviously this has an observable effect on the count rates as well on the fidelity of our produced states. A detailed analysis of this influence is done in Section 4.

Fibre beam splitter

At this stage (ideally) six photons are located in the single-mode fibre. As can be seen from Figure 3.1 it is now necessary to split them into three modes with a probability of one third each. This is achieved by a fibre beam splitter with one input mode and three output modes.

The used fibre beam splitter was manufactured by Sifam and was designed for the wavelength of 780 nm. The wavelength mismatch of 28 nm resulted in a modified splitting ratio which can be found in Table 3.2.

The fibre was not polarisation maintaining so it introduced an unknown phase and polarisation rotations to our state. To compensate that effect as well as an unwanted phase shift from the beam splitters we used phase-shifting crystals described in the next subsection and so-called bat ears. Bat ears are devices which are based on the fact that polarisation rotations and phase shifts can be performed by twisting the non polarisation-maintaining fibre.

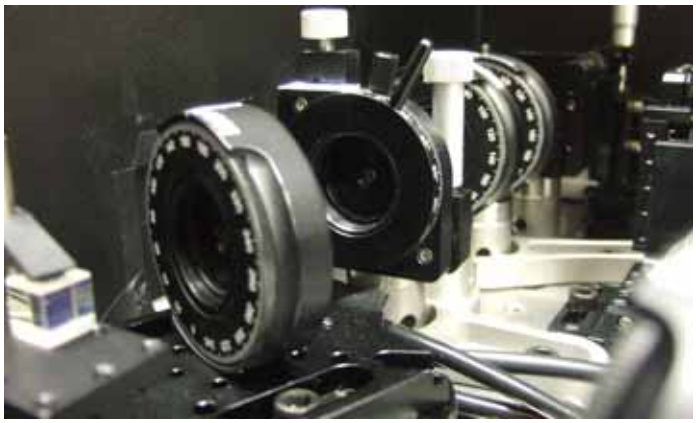

Figure 3.4: Picture showing the phase compensating YVO_4 crystals. The first is tiltable and the second compensates the broadband effects described in the text. The last two mounts contain quarter- and half-wave plates for the final polarisation analysis. On the left side, a PBS can be seen out of focus.

Phase-shifting YVO_4-crystals

After coupling-out of the fibre into free space again, each spatial mode is split up by a beam splitter such that in total six spatial modes are now available and populated. The transmission of these cubes was around 44% and the reflectivity was around 42%.

After the beam splitters birefringent Yttrium-Vanadate YVO_4 crystal were deployed to compensate the phase shift introduced by the fibre beam splitter and the beam splitters seen in Figure 3.1. The working principle is described in more detail in Section 4.3. The thickness of the two crystals employed in each arm was 200 micrometres each and their optical axis were normal to each other.

Measurement bases

Our measurements are realised by recording the output patterns for different so-called local measurement settings (LMS). This means that the measurement can be performed such that each qubit is measured in a specified basis. The measurement M on n qubits is broken into n (different) local measurements:

$$M = M_1 \otimes M_2 \otimes \ldots \otimes M_n. \tag{3.2}$$

The polarisation analysis M_i on the i^{th} qubit is performed with the combination of quarter- and half-wave plate followed by a PBS. They were set up in each of the six spatial modes so that the LMS could be set for each mode individually. The wave plates rotate the desired state into the Z basis and the following polarising beam splitter projects the H and V modes onto two detectors. Exemplary values of the wave plate angles for the X, Y and Z bases can be found in Table 3.3 and angles for some performed non-trivial measurement settings are given in Table 3.4.

target	QWP	HWP
H	0°	0°
V	0°	45°
P	45°	22.5°
M	45°	67.5°
R	45°	45°
L	45°	0°

Table 3.3: To project the target state into the first detector the corresponding wave plate angles need to be set.

	Y+Z	Z+2Y	X-Y	X+Y+Z	X-Y+Z
QWP	0°	0°	45°	22.5°	22.5°
HWP	11.25°	16°	11.25°	20°	2.5°

Table 3.4: The wave plate setting of some, in the experiment used, LMS. The normalisations have been omitted.

Detectors

The twelve modes get coupled into fibres again leading to the detectors. But this time multi-mode fibres are sufficient because the single modes have already been filtered out by the previous single-mode fibre. The multi-mode fibres required an extra coating over their whole length to minimise background light to get scattered into our fibre which would increase the noise. Still it was necessary to shield it from any ambient light sources, especially scattered UV light. Additionally the fibre tips were anti-reflection coated to maximise the coupling-in efficiency of the down-converted IR light.

They are then plugged into our detectors which are so-called avalanche photo diodes on silicium basis (Si-APDs) modules by PerkinElmer which are operated with a reverse bias voltage in excess of their break-down voltage, called the Geiger-mode [45, 46]. They additionally carry the name single-photon detector as they are so sensitive that one photon can trigger an avalanche. The APD modules have an average quantum efficiency of 0.4 meaning that 40% of the single photons arriving on the detection surface will be recorded as an event. Their dark count rate is of the negligible order of 100 events per seconds and it is necessary to protect them from excessive light to prevent any damages. After an event the detector is insensitive to further photons for 50 ns [25]. This time span is called the dead time. It is of no importance for most experiments as the probability of having another photon arriving at the detector within the dead time is negligible. But in our case we require six detectors to be ready when six photons arrive and it turns out that this is only satisfied in 95 percent of all cases (see Section 4.2.1 for a detailed discussion).

Qubit	1	2	3	4	5	6
Detector H	97.99	97.17	78.70	96.57	99.26	80.43
Detector V	92.93	96.24	75.98	94.08	95.04	100.

Table 3.5: Efficiencies of the detectors used for analysing the six qubits. The naming of the detectors is consistent to Figure 3.1. The same input of light was fed into each detector consecutively and the detected count rates recorded. The numbers shown in the table are percent relative to the best detector V6, who saw around 1 million events.

Coincidence logic

The outputs from the detectors are plugged into a coincidence logic with a maximum input of twelve ports. The logic can be programmed to record up to 64 coincidences. Programmed to record every possible six-fold coincidence which are exactly $2^6 = 64$, we had to adapt the measuring program to also exclude unwanted clicks, ie. implement a logical NOT on the other modes. This was possible by setting the polarity of events in the detection logic and could be configured and changed via a LabVIEW programme.

The events were grouped together within the coincidence window which was set to 4.5 ns. So events recorded within one such frame were treated as coincidences. To see coincidences it is necessary to adjust the timing delay between the twelve detectors. As each of the photons travels independent paths of different lengths through the setup, they arrive at the detectors at different times which needs to be considered. Also, the individual detectors process the signal at their own pace which requires additional delay. Only when the delays where chosen correctly high coincidence rates where observed. When the delay was multiples of 13.2 ns away lower coincidence rates could be seen which originated from accidental coincidences by pairs from different peaks of our pulsed laser. The optimal delay was found by scanning the coincidence rate over the delay time.

We also investigated the detection efficiency, which is the quantum efficiency, relative to each other. This was done by coupling light into a fibre and attaching the fibre to the different detectors. The obtained efficiency relative to the best detector can be seen in Table 3.5.

Chapter 4

Simulations

4.1 Introduction

Simulations were crucial for our experiments as there are a few key elements that need to be addressed with this setup. First it was necessary to discuss if the experiment was feasible or even possible to realise at all. Due to the nature of the SPDC process we needed to estimate the rate of observed events as well as their quality which is also greatly influenced by higher-order emission. Through an intensive investigation the effects of the experimental limitations and requirements of future setups could be assessed. Also the characterisation of the setup was not straight forward and the simulations helped to examine the parameters.

Additionally, a rather novel method [47] was used to compensate an unquantified phase introduced by various components in the setup, especially the single-mode fibre. This method proved to be very sensitive in the laboratory so a detailed analysis facilitated the setup.

4.2 Higher-order effects

Simulations were done approximatively and in two separate ways: First by analytic simulation by hand as well as by using Mathematica and second numerically in MatLab. Both approaches had their advantages and drawbacks. The analytical approach had the advantages of being able to vary parameters and plot their dependencies which was only possible for a few points in the numerical case due to the long simulation time which each set of parameter required.

As already mentioned previously the nature of our down-conversion process causes not only three-pair emissions but also higher-order emissions which extend our Hilbert space beyond the six-photon Dicke state space. This ultimately affects the quality of the experimentally produced state.

The probability for N-pair production is p^N where all $2N$ photons are emitted into the same spatial mode and propagated through the setup. From three-pair

emission only the cases are post-selected where one photon ends up in each spatial mode. The probability for this to happen is: $\frac{6!}{6^6} \sim 0.015$. So from all photons produced by three-pair emission only 1.5 % end up as Dicke states with one photon in each of the six spatial modes.

In an ideal setup with no photon loss and number-resolving single-photon detectors it would be possible to discriminate the higher-order terms through post-selection making the procedure insensitive to them. Of course we do have losses in the setup and non-ideal detectors which are furthermore not number resolving. The following part will focus on the consequences that result thereby. Our detectors, instead of being number resolving, can be simulated by a so-called "bucket detector" which refers to the behaviour of recording an event with probability

$$p_{\mathrm{det}} = 1 - (1 - p_1)^N, \tag{4.1}$$

when N photons are entering. p_1 is the detector sensitivity towards one photon and p_{det} is the overall probability that at least one photon is detected. Losses in the setup itself are minimal except for the coupling into the fibres. In general these losses can be propagated through the setup and integrated into the detection efficiency. So when talking about the detection efficiency in this chapter the overall probability of detecting a photon is meant which comprises of the detector efficiency as well as the surviving probability through the complete setup which itself is again only the result of different effects. Sources of loss are mainly the coupling into the fibres but also to a lesser degree the optical elements, for example the (polarising) beam splitters. As only the total efficiency is of interest for the simulation (not for the alignment, of course) the individual contributions remain unmentioned furthermore.

The losses in the setup have the following influence: As an example, a four-pair emission when losing two vertically polarised photons will give an unwanted $D_6^{(4)}$ state upon successful post-selection. This state has no overlap with the $D_6^{(3)}$ state and hence a vanishing fidelity. Events from recording such states lower the experimentally observed fidelity. But the other cases where two differently polarised photons are lost do no harm but even enhance the observation of desired coincidences. In other words, when one H and one V polarised photon out of the four Hs and Vs are lost at any stage, a $D_6^{(3)}$ state is obtained upon successful post-selection. This happens with probability $\frac{1}{2}$ of all two-photon losses only when the photon loss for H and V is balanced, which as will be discussed later is not justified in our experiment. In general a simple approximation shows that N-pair emission gives a valid Dicke $D_6^{(3)}$ state with the probability P:

$$P = \frac{1}{2^N}\binom{N}{3}^2 p_H^3 p_V^3 (1 - p_H)^{N-3}(1 - p_V)^{N-3}, \quad N \geq 3, \tag{4.2}$$

depending on the surviving probability $p_{H,V}$ for the horizontally and vertically polarised photons.

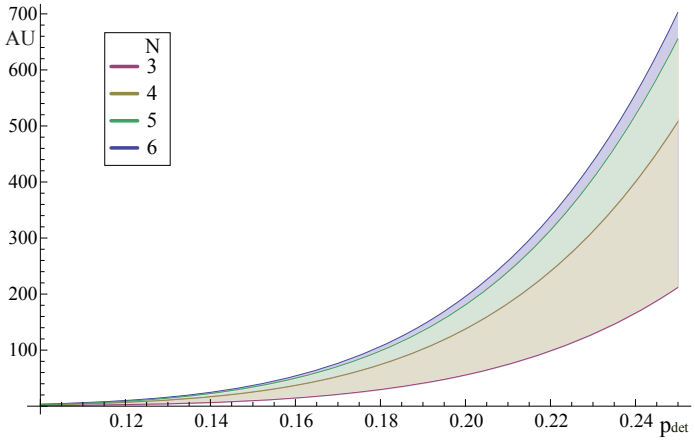

Figure 4.1: The different contributions from N-pair emission to the recorded six-fold coincidences are shown in stacked form. The detection efficiency ranges from 0.1 to 0.25. The values for the vertical axis are given in arbitrary units. The down-conversion efficiency is chosen to correspond to a UV pump power of 1.5 W.

Also the influence of the lacking ability of number resolution can be illustrated with a four-pair emission. When the four vertically polarised photons only occupy two spatial modes then the post-selected event looks like a $D_6^{(2)}$ state. This is true for a measurement in the X basis but only with a probability for other measurement bases. A number resolving detector, however, could always discriminate these states.

4.2.1 Analytical simulation

The first approach was to use Mathematica and to produce the $D_6^{(3)}$ state together with the next higher orders ending up in six modes with the different production probabilities. The fraction of the higher-order emissions are displayed in the Figures 4.1 and 4.2. It can be seen that the higher orders have an enormous impact justifying the further analysis. The detection efficiency is a critical parameter as besides increasing the count rates dramatically (in first approximation to the sixth power) it also allows for a better discrimination of unwanted events. Even with perfect detection the four-pair emission contributes to about 30 percent of all recorded events.

This simulation is an approximation to the real situation in the experiment. It should be mentioned that it also assumes that the setup is symmetric meaning that the photon surviving probabilities are the same no matter which arm they travel. This is a justified assumption for our rough estimation but not entirely true as can be already seen from the imbalanced detector efficiencies in Table 3.5.

The simulation demonstrates how the key parameters manifest themselves in the observed values like the count rates, fidelity and two-qubit correlations.

Once having the simulation running it empowers us to compare the experimen-

tally accessible values with the predictions.

For a more detailed analysis considering the four-pair emission gives some further insight. The rate R_4 of eight photons originating from four pairs being found in six occupied spatial modes is:

$$\begin{aligned} R_4(p_{\mathrm{det}}, p_{\mathrm{prod}}) &= p_{\mathrm{prod}}^4 R_L \frac{1}{10080} \left\{ 4 p_{\mathrm{det}}^5 \left(1 - (1 - p_{\mathrm{det}})^3 \right) \right. \\ &+ \left. 15 p_{\mathrm{det}}^4 \left(1 - (1 - p_{\mathrm{det}})^2 \right)^2 \right\}, \end{aligned} \tag{4.3}$$

with R_L being the repetition rate of the laser and p_{prod} the probability of one-pair emission. The first part is the case when three photons end up in the same mode whereas the second part describes the case where twice two photons are in the same mode. The factors are derived with the binomial formula.

Equation 4.3 does not yet take into account that the polarisation measurement can result in more than six detector clicks. This can happen if two different polarised photons occupy the same mode or when the measurement bases is not set to Z.

Investigating first the case when the local measurement bases is set to Z shows that some of these clicks $E_{8,\mathrm{Good}}$ increase our expected coincidence pattern whereas some $E_{8,\mathrm{Bad}}$ worsen it:

$$\begin{aligned} E_{8,\mathrm{Good}}(p) &= \Big\{ C_{1,s} \cdot 0 + \\ &+ C_{1,d} \cdot p^5 (1-p) \left(1 - (1-p)^2 \right) \\ &+ C_{2,s,d} \cdot p^4 \left(1 - (1-p)^2 \right) p (1-p) \\ &+ C_{2,d,d} \cdot p^4 \cdot 2p^2 (1-p)^2 \\ &+ C_{2,s,s,d} \cdot p^4 \left(1 - (1-p)^2 \right)^2 \\ &+ C_{2,s} \cdot 0 \Big\} / \sum_8 \end{aligned} \tag{4.4}$$

and

$$\begin{aligned} E_{8,\mathrm{Bad}}(p) &= \Big\{ C_{1,s} \cdot p^5 \left(1 - (1-p)^3 \right) \\ &+ C_{1,d} \cdot p^5 (1-p)^2 p \\ &+ C_{2,s} \cdot p^4 \left(1 - (1-p)^2 \right)^2 \\ &+ C_{2,s,d} \cdot p^4 \left(1 - (1-p)^2 \right) p (1-p) \\ &+ C_{2,d,d} \cdot p^4 \cdot 2p^2 (1-p)^2 \\ &+ C_{2,s,s,d} \cdot 0 \Big\} / \sum_8, \end{aligned} \tag{4.5}$$

with $\sum_8$ denoting all possible eight fold coincidences.

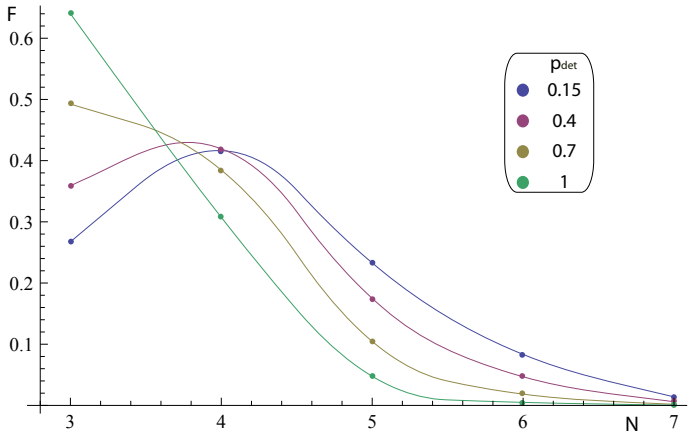

Figure 4.2: The influence of the detection probability p_{det} on the relative N-pair fraction F of the recorded six-fold coincidences. Each graph has been interpolated and normalised for better comparison, as the total sum also raises with p_{det}.

The terms $C_{i;x,y}$ describe the cases where i modes are occupied by more than one photon. The indices $x, y = s, d$ describe if the photons occupying the same mode have the same or different polarisation.

The total six-click rate R_T is the sum of all possible i-pair emission rates:

$$R_T(p_{\mathrm{det}}, p_{\mathrm{prod}}) = \sum_{i=3}^{\infty} R_i. \tag{4.6}$$

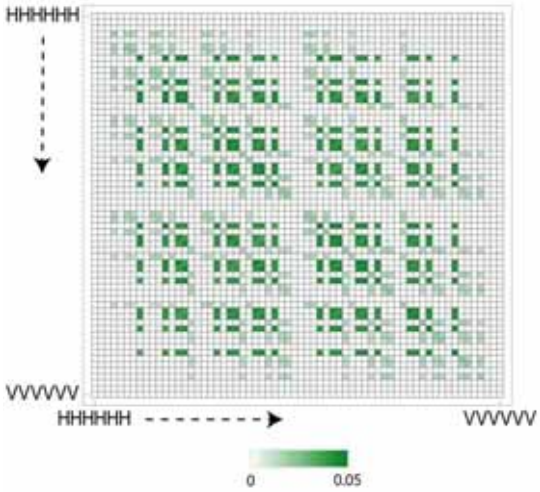

Figure 4.3: The analytically simulated density matrix for the six-photon Dicke state is shown. The simulation includes the next higher order, i.e. events from four-pair emission which are responsible also for the light green populations.

Repetition rate	Dead time	Pulse interval	Singles
76 MHz	50 ns	13 ns	300 kHz

Table 4.1: Properties of our setup which are needed to calculate the influence from the dead time of our detectors on the detection probability of our six-fold coincidences.

Detector dead time influences

When avalanche photo diode detectors register a photon, an avalanche of charge carriers is released. It then takes some time, called the *dead time*, to restore the initial condition during which the detector is insensitive to further photons. For most experiments this has no implications as the probability of two events following each other within the dead time is negligible. But this is not true anymore in our more complex setup. For a successful six-fold event detection we require six detectors to be ready which is not always fulfilled as will be shown. Our detection rate is hence lowered.

A pulsed laser with repetition rate R has an interval $w = 1/R$ between two successive pulses. After a detection, the detector with dead time D is insensitive for n other pulses (using the floor function):

$$n = \lfloor \frac{D}{w} \rfloor - 1, \quad w < D. \tag{4.7}$$

The probability P of N detectors to be ready depends now on their history and is given by:

$$P = (1 - p_s)^{N \cdot n}, \tag{4.8}$$

with p_s being the probability of a photon arriving at the detector per pulse. In our case it is given by the observed single rate S divided by the number of pulses per second.

In the last step a few assumptions are made. For this to be valid, the probabilities of photons arriving at the different detectors should be uncorrelated. In our case this is a justified assumption, as the main contribution to detector clicks come from one-pair and two-pair emission. Together with the loss probability, the fact that we are concerned only about six out of twelve detectors allows us to treat the events as uncorrelated.

When inserting the values for our setup (see Table 4.1) we see that only in 95 percent of all six-fold events arriving at the detector, we find all of them ready to record the photons. This demonstrates, that while it has always been assumed safe to ignore the influence of the dead time, there are cases for which this does not hold but needs to be considered as well.

4.2.2 Numerical simulation

The numerical simulation was done with Matlab and a modified version of an online available *Quantum Optics and Computation Toolbox* [48]. The toolbox allows

to simulate systems using the Fock formalism. Each mode, may it be spatial, polarisation or any other degree of freedom, is characterised by the photon number. For example the state $|0,0,0,1\rangle_A$ corresponds to three photons in mode A (the first element corresponds to the vacuum). The limitation (besides numerical accuracy) was the maximal photon number N, which determined, together with the number of spatial and polarisation modes $n_{\mathrm{sp}}, n_{\mathrm{pol}}$, the size of the used Hilbert space $\mathcal{H}$:

$$\dim(\mathcal{H}) = N^{n_{\mathrm{sp}} n_{\mathrm{pol}}}. \tag{4.9}$$

Simulating a density matrix of the system requires a matrix with $\dim(\mathcal{H})^2$ elements which grows exponentially with respect to the number of modes and polynomial to N. This behaviour influences vastly the resource demands of the computer system and the duration of the simulation. They are the limiting factors of the analysis.

When two modes interact like in a beam splitter or a wave plate, it is necessary that N_{out} for the outgoing modes is at least equal to the sum $N_{in,A} + N_{in,B}$ of the maximal photon number in the incoming modes. This is very crucial for the correct behaviour when interferences happen. Fortunately, the second input mode for our beam splitters was always empty: $N_{in,B} = 0$. The only care had to be taken for the wave plates. Generally both polarisational modes taken as input for the beam splitters were occupied. But as they are located at the end of the setup, the photons are already distributed among the spatial modes. Less photons populate the polarisational modes and the photon number requirement is also fulfilled at this stage.

Due to hardware limitations on available memory as well as the software limitation of 32bit the toolbox was modified by Thomas Jennewein. Additionally the code had to be rewritten to use the density matrix formalism. Still, it was not possible to generate the full density matrix, so the simulation had to be broken into multiple parts. The simulation first evolves two spatial modes and projects them onto the desired basis which allows tracing out the modes. In the second step the same is done with the next two spatial modes until for the final step the remaining two spatial modes are evolved. This eases the memory requirement as at no point more than four spatial modes are evolved and tracked.

The different experimental tools like polarising or fibre beam splitter as well as the half-wave plates were simulated using the respective Hamilitonians described in Section 2. The detection was realised with projectors and a (if necessary partial) trace. To give an insight into the simulations an extract of the code can be found in Appendix C.

Our code included simulating a different coupling into the single-mode fibre after the down-conversion for H and V polarised photons. It was also possible to set different wave-plate angles for each qubit allowing simulation of all different local measurement settings taken in the experiment.

The sources of loss explicitly included in the simulation were: the coupling into the single-mode fibre, the final coupling into the multi-mode fibres and the quantum

efficiency of the single-photon detector modules. The losses at the (polarising) beam splitters were comparably low and were not included in the simulation. The parameters used as input for the simulation were: The squeezing parameter ϵ, which describes the strength of the down-conversion and the coupling efficiency into the single-mode fibre for H and V-polarised photons c_H, c_V in order to simulate the observed coupling imbalance due to the transverse walk-off effect as discussed in Section 2.3.2. Also adjustable was the coupling efficiency into multi-mode fibre at the end: c_{MM} and the quantum efficiency of the detectors with p_{det}.

Higher-order effects on characterisation of the Setup

The characterisation of an experiment is an obvious thing to do as it tells how well the realisation can be done. Most of the parameters used for characterisation were defined in a regime where higher-order terms could be neglected. Due to the inherent nature of our experiment it was necessary to look at the higher-order influences on these parameters.

The quality of a source is normally studied by sending the spatial mode containing the entangled photons into a PBS and registering the singles and double coincidences. By single we mean events when only one detector clicks whereas it is called a double coincidence when both detectors fire simultaneously. The rate of singles over doubles depends on the coupling efficiency of the two couplers. The pair production probability can be inferred from the doubles.

In this case where the Dicke setup was attached directly to the source we could not infer to the coupling efficiency in the above explained way but needed other

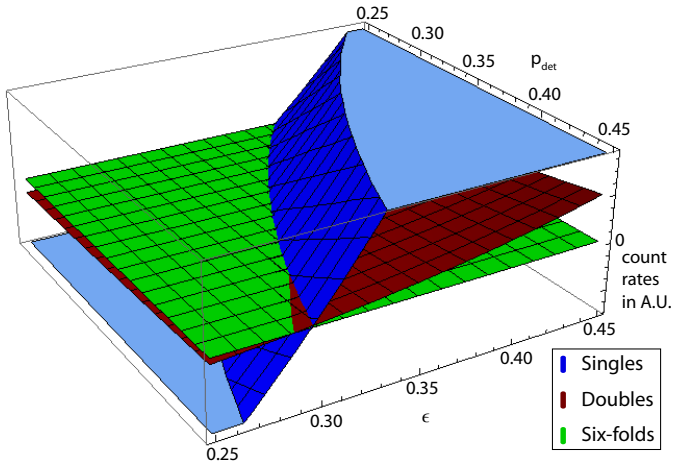

Figure 4.4: The simulation results allow the setup parameters, the squeezing and the detection probability, to be deduced from the count rates, shown as surfaces. By subtracting the experimental single-, double- and six-fold coincidences from the simulated values, all surfaces meet in one point at $z = 0$. The values for the detection efficiency and the squeezing parameter can then be read off.

means of characterisation. The observed single coincidences were recorded when one detector gave a click independently of the others, i.e. four photons in four modes would be recorded as four single-coincidences and six double-coincidences.

To quantify the parameter values we recorded typical values for the one-, two- and six-fold coincidences. They are easily accessible during the setup and allowed scanning over a subspace of the parameter space to find close values for the above mentioned parameters. A scan over the squeezing parameter[1] ϵ and the combination of multi-mode coupling and quantum efficiency $p_{\text{det}} = c_{\text{MM}} \cdot p_{\text{QE}}$ can be seen in Figure 4.4.

The detection after the setup was at a rate of ~ 0.003 six-fold coincidences per second at a maximum UV power of 1.4 Watt. The singles rate was about ~ 1.4 MHz per second and the doubles about ~ 80 kHz. The parameters concluded from the examination of the plots are a squeezing parameter of $\epsilon = 0.32$ and a detection efficiency of $p_{\text{det}} = 0.4$.

Higher-order effects on the fidelity

up to N-pairs	total events/day	fidelity of $D_6^{(3)}$
3	29.34	0.94
4	106.53	0.63
5	151.23	0.58
6	165.88	0.55
7	169.47	
8	170.21	

Table 4.2: Total counts per day and fidelity of $D_6^{(3)}$ dependent on the included higher orders with up to N-pairs. The included H-V imbalanced coupling is included and responsible for the fidelity being less than 1 for $N = 3$.

The simulation empowers us to make predictions about the fidelity to be expected in the experiment. Results of such a simulation are shown in Table 4.2 and Figure 4.5 where the following parameter values were assumed: $c_H = 0.3$, $c_V = 0.15$, $\epsilon = \sqrt{0.12}$, $c_{\text{MM}} = 0.8$ and $p_{\text{det}} = 0.45$.

The predicted fidelity drops significantly by including the next two higher orders ($N = 4, 5$). It actually converges to a lower value than the experimentally observed one which originates from the conservative choice of starting values for the simulation.

To obtain the fidelity 21 local measurement settings (as discussed in Section 3.2) needed to be simulated. The outcome pattern of the coincidences for the Z basis is shown in Figure 4.6, together with the ideal pattern and the experimentally obtained.

[1] The squeezing parameter ϵ describes the strength of the coupling for the down-conversion: $H = (a_s^\dagger a_i^\dagger a_p + a_s a_i a_p^\dagger)\epsilon$. See also Section 2.3.2.

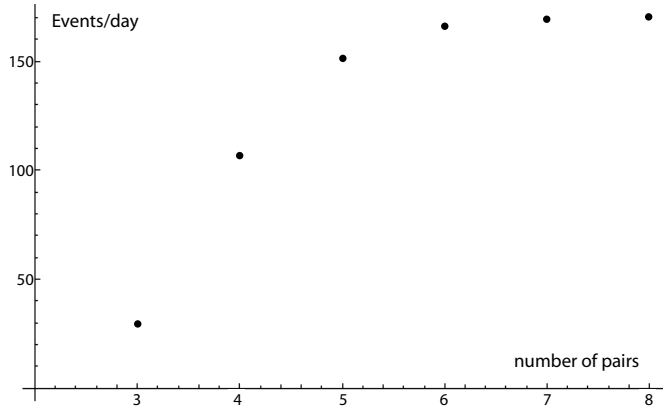

Figure 4.5: Total events per day increasing with up to N-pair production included (see also Table 4.2). As can be seen only the next two highest orders contribute significantly.

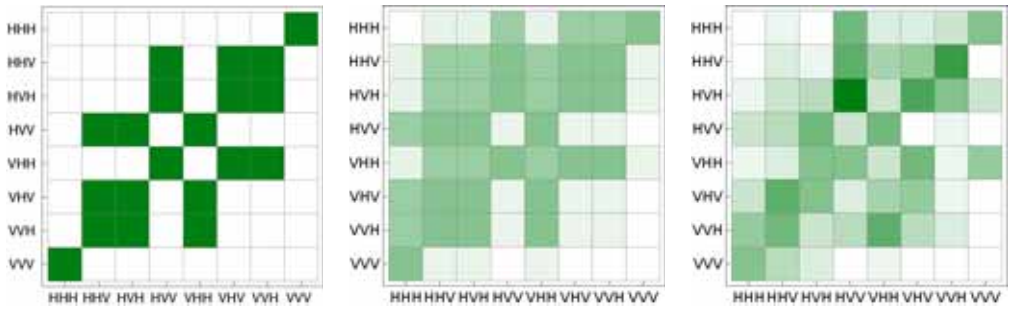

(a) Ideal (b) Simulation (c) Experiment

Figure 4.6: Comparison between the ideal (a), simulation (b) and experimental (c) outcome pattern for the local measurement setting $Z^{\otimes 6}$. The simulation is with up to five-pair emission which leads to additionally expected combinations. The different coupling-in efficiencies for H and V shift the pattern towards the upper left corner. The experimental outcome pattern is in between the ideal and the simulated pattern, showing that the choice of parameters for the simulation was very conservative.

4.3 Phase shift by YVO_4-crystal

As already mentioned our setup introduces various unknown phases and polarisation changes to the states of our photons dependent on which way they travel. This is due to the single-mode fibre which is not polarisation maintaining and the beam splitters which introduce a phase shift upon reflection. To compensate these effects it is necessary to apply an adjustable phase to each photon. In our setup we therefore

n_o	1.9716
n_e	2.1852
d [μm]	200

Table 4.3: Parameters of the YVO_4 crystals

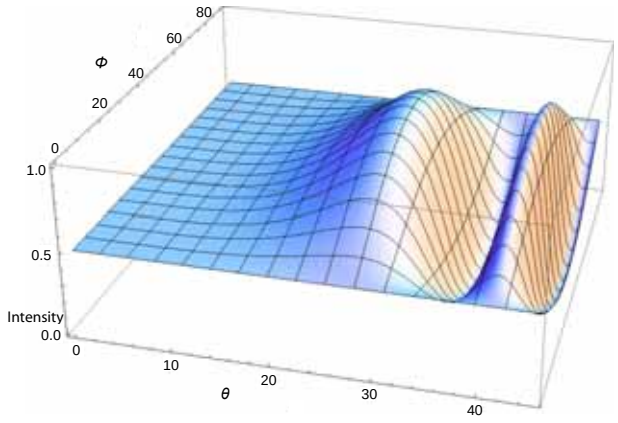

Figure 4.7: The normalised intensity of polarised light after passing two YVO_4 crystals tilted by θ and rotated by ϕ with respect to each other. Only when the intensity is 1, the polarisation is maintained, otherwise the other polarisational mode is populated. The sharp maxima makes the alignment procedure very sensitive to the tilting angle θ.

applied a recent method [47], using Yttrium-Vanadate YVO_4 crystals. This material is birefringent, its properties can be found in Table 4.3. The crystals are cut in such a way that their optical axis lies within the entrance plane. The phase compensation is done by one crystal whose optical axis is chosen to be aligned horizontally. The crystal then only introduces a phase shift to the V component which is dependent on the thickness d of the crystal and the refractive indices n_o and n_e: $\delta = \frac{2\pi}{\lambda}|n_e - n_o|d$ (see discussion in Section 2.2.1). By tilting the crystal around an axis perpendicular to the beam, the photon sees a changing thickness different for the o- and e-beam: $d_{o(e)}(\theta_{o(e)}) = \frac{d}{\cos(\theta_{o(e)})}$. The entrance angle $\theta_{o(e)}$ can be determined through Snell's law. The different path lengths allow to tune the phase. The phase shift is given by:

$$\delta(\theta) = \frac{2\pi}{\lambda}\left|\frac{n_e}{\sqrt{1-[n_l/(n_e\sin(\theta))]^2}} - \frac{n_o}{\sqrt{1-[n_l/(n_o\sin(\theta))]^2}}\right| d. \tag{4.10}$$

The derived equation is only exactly fulfilled for one wavelength λ because n is wavelength dependent. The refractive index can be expressed as a Sellmeier equation [49]:

$$n(\lambda) = \sqrt{1 + \sum_{i=1}^{N} \frac{A_i\lambda^2}{\lambda^2 - B_i}}. \tag{4.11}$$

Because our beam is broadband within ± 1.5 nm the contrast between the H and V output is significantly reduced as can be seen in Figure 4.8. The wavelength dependency of the phase shift originates from the, relative to λ, huge thickness of the crystal. To compensate for this a second YVO_4 crystal is introduced, whose

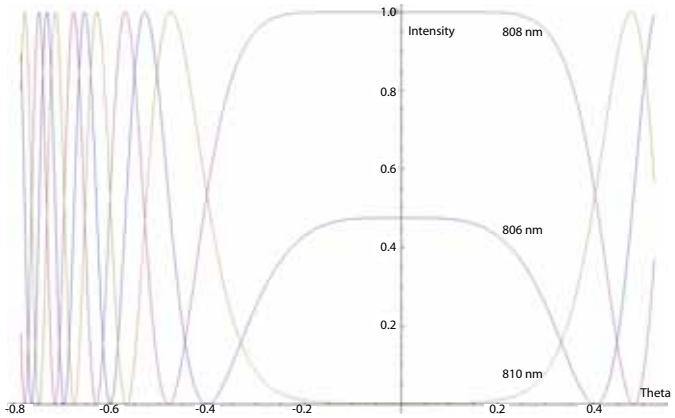

Figure 4.8: Intensity of the horizontal polarisation of 808 nm (purple), 806 nm (blue) and 810 nm (green) photons after passing two YVO_4 crystals which are tilted by θ against each other.

axis is normal to the beam and the axis of first crystal. When the first crystal is tilted, the path length difference is now only of the order of one wavelength. Both crystals together act effectively as a first-order phase compensator.

To align the crystal in the setup we used the previously described behaviour. First, we send horizontally polarised light onto the first, tiltable crystal which was afterwards analysed by a PBS and two detectors. In an iterative procedure, the crystal was rotated until the high contrast did not change when it was tilted. This ensures that the optical axis of the crystal is either normal or parallel to the polarisation of the incoming light. To align the optical axis of the second crystal, it is now also put into the setup and rotated until the contrast improves even further due to the compensation of the broadband effect. When the optical axis of the second crystal is perpendicular to the first, the contrast is independent of tilting the first.

Once they are aligned, one can start adjusting the phase compensation of the fibre which is done through two different mechanism: fibre tilting done by the so-called bat ears and by tilting the YVO_4 crystal. First, H polarised light is coupled into the single-mode fibre and a position of the bat ears is found where a high contrast between the H- and the V-detector is given. The not yet aligned tilting angle of crystal is of no influence. In the next step, P polarised light is coupled into the fibre and the measurement basis is also set to detect P and M. Now the contrast is optimised by finding the right tilting angle. The process is very sensitive as the minima and maxima of the phase are close together which can be seen from Figure 4.7. Once this is achieved, the phase compensation is ensured for all bases.

Chapter 5

Experimental results

This chapter will present the outcome of our experiment and how we qualified and quantified our produced states. Additionally it will be demonstrated how different quantum protocols can be employed.

A very commonly used method to analyse a multi-particle state is to use so-called state tomography. This is done by measuring the density matrix, i.e. all possible combinations of outcomes in the configurational basis. But this procedure requires i^{2N} measurements where i is the number of degrees of freedom of one particle and N is the number of particles forming the state. For example a qubit has $i = 2$ and for a qutrit $i = 3$. For higher-particle states this method becomes obviously extremely unfeasible as the number of elements needed to be measured grows exponentially. The six-photon Dicke state would have required 4096 measurements at around 48 hours each. This would correspond to more than 22 years of measurement time. As a consequence we employed other techniques like witnesses (see Section 1.5) to obtain information about our states.

The experiment was conducted with numerous measurements which had special wave-plate settings determining the local measurement basis for each individual qubit. We then recorded all possible six-fold coincidences[1] for each LMS. To obtain statistically significant results it was necessary to record a sufficiently large amount of six-fold coincidences. Theoretical work showed that our spin-squeezing witnesses showed a convergent behaviour for higher events so we recorded between 150 and 300 events for each local measurement setting. Our observed six-fold coincidence count rate was ~ 8 per hour so typically a local measurement setting took around 23 hours. The observed singles rate was around 1.4 MHz and for the two-fold coincidences around 120 kHz. These rates are typical for collinear type-II setups with 1.5 Watt CW-average UV pump power. Our setup was very stable over time, our mere total measurement time was about 1795 hours ($\sim$ 75 days) which was not continuous but had idle periods in between due to external circumstances like air condition

[1] as defined in Section 4.

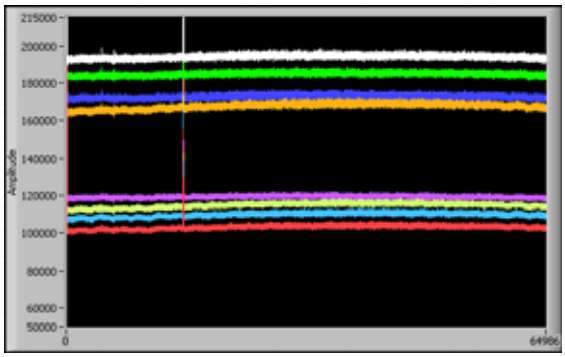

Figure 5.1: The singles count rates, of which eight out of twelve are shown, proved to be extremely stable over a long period, in this case 65000 seconds ($\sim$ 18 hours). The LMS was $Z^{\otimes 2}(X+Y)^{\otimes 4}$. The influences of the different detection efficiencies as well as the H/V imbalance on the singles can be seen. The high spike after one fourth of the time is an artefact without any relevance, due to heavy CPU load while logging into the computer for observation.

failures in the laboratory. During that time no readjustment was necessary. Also the observed event rates were extremely stable. A graph demonstrating the time stability of observed singles during one day can be seen in Figure 5.1. Due to the different generated states described below it was necessary to measure with 33 different, unique local measurement settings (LMS). The ideal six-, five- and four-fold coincidence patterns for most of the LMS can be found in Appendix B.

5.1 Six-photon Dicke state

As already mentioned we produce in our setup symmetric six-photon Dicke states $D_6^{(3)}$:

$$D_6^{(3)} = \frac{1}{\sqrt{20}} \sum_P |HHHVVV\rangle_{123456} \,,$$

being the sum of the 20 different permutations of three H and three V polarised photons.

The fidelity of the state was measured and general multipartite entanglement verified through the use of a spin-squeezing witness.

5.1.1 Spin-squeezing witness for six-photon Dicke state

For the measure of genuine multipartite entanglement (GME), the standard spin-squeezing witness for the six-photon Dicke state $D_6^{(3)}$ is $\langle \mathcal{W}_{SS} \rangle = \langle J_x^2 + J_y^2 \rangle$. This witness proves GME due to the fact that for all six-qubit separable states $\langle \mathcal{W}_{SS} \rangle_{BS} \leq 11.02$. This value is obtained by numerical maximisation of the witness with all the biseparable states (BS): $11.02 \overset{\max}{=} \langle \mathcal{W}_{SS} \rangle_{BS}$. By this construction the spin-

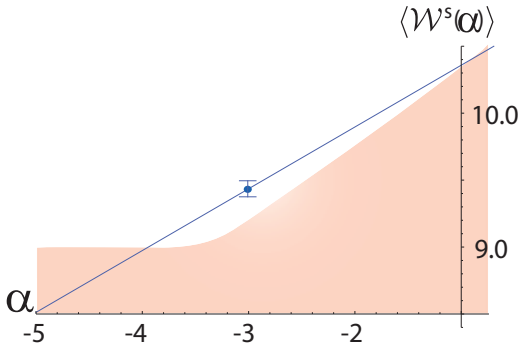

Figure 5.2: The painted area presents the biseparable region containing the values the noise resistant spin-squeezing witness will return for biseparable states. The blue line shows the value of the noise resistant witness for the Dicke state. When the line is in the shaded region the witness fails to resolve genuine multipartite entanglement. By adjusting α, the maximal difference can be found. The point shows the experimental value for ρ_6^3.

squeezing witness fulfils all the conditions stated in Section 1.5. Whenever this limit is exceeded $\langle \mathcal{W}_{SS} \rangle_f > 11.02$ GME is proven for the state $|f\rangle$.

But this spin-squeezing witness (SSW) turns out to be very fragile to noise. As a consequence a noise resistant spin-squeezing witness had to be introduced [50]:

$$\langle \mathcal{W}_{SS} \rangle = 9.2 - \langle J_x^2 + J_y^2 - \alpha J_z^2 \rangle, \tag{5.1}$$

where $9.2 \overset{\max}{=} \langle J_x^2 + J_y^2 - \alpha J_z^2 \rangle_{BS}$ is again obtained by numerical maximisation for all separable states.

This special form is useful as the noise is visible mainly in the Z basis as is known from Section 4. For ideal Dicke states however, $\langle J_z^2 \rangle$ vanishes. By introducing that term with prefactor α, one can optimise the gap between the value for biseparable and $D_6^{(3)}$ states at $\alpha = -3$ (see Figure 5.2) leading to the experimentally observed value

$$\langle \mathcal{W}_{\mathbf{SS}} \rangle = \langle \mathcal{W}_{\mathbf{SS}} \rangle_{\mathbf{BS}}^{\max} - \langle \mathcal{W}_{\mathbf{SS}} \rangle_{\mathbf{D_6^{(3)}}} = \mathbf{-0.24 \pm 0.06}. \tag{5.2}$$

This result ensures GME for our state with the requirement of only three local measurement settings. However, for some values of α the witness fails to distinguish between biseparable and Dicke states. An elaborate discussion of the behaviour and applicability of noise resistant SSW as well of the different decoherence and dephasing mechanisms can be found especially in [50] and also [51]. These papers were motivated by the experiment presented in this thesis and a similar experiment [52].

As theoretically expected, the spin-squeezing witness exhibited a convergent behaviour dependent on the number of measured events. Hence, it was necessary to increase the measurement time to obtain a sufficient large number of events.

The observed coincidence pattern for the three local measurement settings is displayed in Figure 5.3.

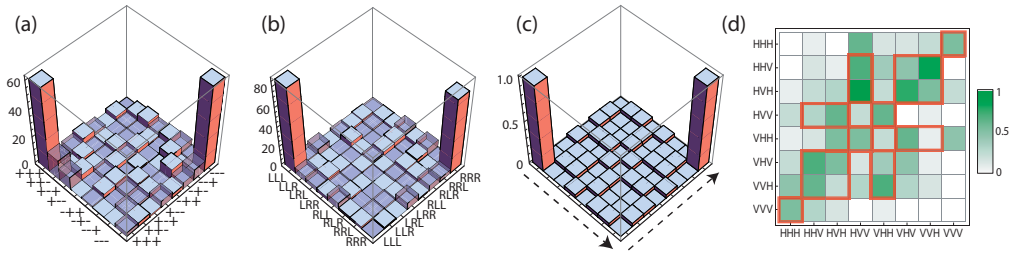

Figure 5.3: The experimental six-photon coincidence pattern for the local measurement settings (a) X and (b) Y are shown. The spurious elements are displayed transparently. In (c) the ideal pattern for these local measurement settings (LMS) is presented for comparison. (d) The experimental outcome for the Z basis is printed. The populations for the ideal $D_6^{(3)}$ state in the Z basis are indicated through the red boxes and are 1.0.

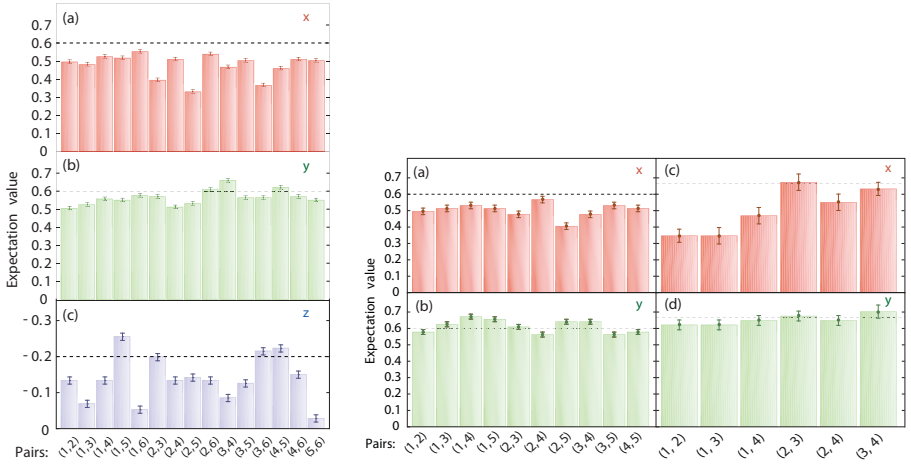

(a) Six qubits

(b) Five and four qubits

Figure 5.4: (a) All possible two-qubit correlations for the six-qubit case are shown which are needed for $J^2_{x,y,z}$ (seen at top, middle and bottom). (b) Analogously for the five-qubit (left) and the four-qubit (right) case, where only $J^2_{x,y}$ where needed. The dashed lines indicate the ideal value.

As already discussed this witness is built from all different two-qubit correlations. The experimental behaviour for the different bases can be seen in Figure 5.4(a). What is striking is the difference in quality: the good behaviour in the X and Y bases opposed to the Z basis. This can be explained through the influence of the different coupling-in efficiencies for the horizontally and vertically polarised photons which manifests itself directly in the Z basis but not in its orthogonal bases. This tendency was already predicted by the simulations.

X	X+Y	X-Z	X+2Z	Z-2X	Z+2Y	X+Y-Z
Y	X-Y	Y+Z	X-2Z	Y+2Z	Z-2Y	X-Y+Z
Z	X+Z	Y-Z	Z+2X	Y-2Z	X+Y+Z	X-Y-Z

Table 5.1: The 21 LMS settings for the fidelity measurement of the $D_6^{(3)}$. Each entry is the setting for all qubits, e.g. $X^{\otimes 6}$. For better reading the normalisation has been omited.

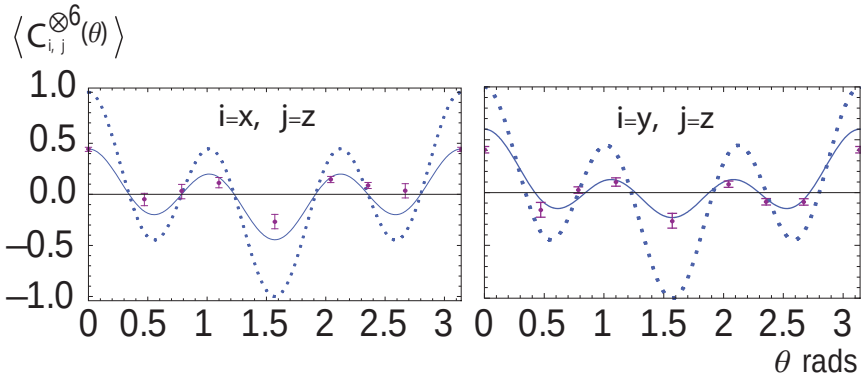

Figure 5.5: The six-photon correlator $\langle C_{i,j}^{\otimes 6}(\theta)\rangle$ for the $D_6^{(3)}$ with $i = x, j = z$ on the left and $i = y, j = z$ on the right. The dotted line is the ideal pattern and the solid line displays the behaviour predicted by simulation.

5.1.2 Fidelity of the six-photon Dicke state

The fidelity of the six-photon Dicke state is given by

$$F = \mathrm{Tr}(\rho_{D_6^{(3)}}\rho_{\mathrm{exp}}), \tag{5.3}$$

where $\rho_{D_6^{(3)}} = |D_6^{(3)}\rangle\langle D_6^{(3)}|$. Expressing $\rho_{D_6^{(3)}}$ into LMS gives 544 different measurements setting which would make realisation unfeasible. Luckily this number could be compactified to just 21 measurement settings which are given in Table 5.1. Thereof the first three LMS, namely X, Y and Z were already taken for the spin-squeezing witness and the data could be reused again.

The experimentally obtained fidelity is

$$\mathbf{F = 0.56 \pm 0.02}, \tag{5.4}$$

which is close to the simulated fidelities ranging from 0.61 for analytical simulation to 0.55 for the numerical simulation (see also Chapter 4.2).

To further examine the features of our state we look at the multi-photon correlator $C_{i,j}^{\otimes N}(\theta)$. The correlation function is defined as the expectation value of the product of local polarisation observables:

$$C_{i,j}^{\otimes N}(\theta) = \bigotimes_{k=1}^{N}\left(\cos\theta\sigma_i^{(k)} + \sin\theta\sigma_j^{(k)}\right). \tag{5.5}$$

For $i, j \in x, y, z$ this probes the correlations in orthogonal planes of the single-qubit Poincaré sphere. Thus it can provide information about the off-diagonal elements of the density matrix. So coherence properties can be learnt for the state in question. For the symmetric six-photon Dicke state the correlator can be written as:

$$\langle C_{i,z}^{\otimes 6}(\theta)\rangle = \frac{1}{8}\left(3\cos\left(2\theta\right) + 5\cos\left(6\theta\right)\right), \quad i = x, y. \tag{5.6}$$

Only due to the coherence of the two-terms, interference can be observed. In Figure 5.5 one can see a comparison of the experimentally obtained values with the ideal pattern as well as with the simulated predictions. Due to the higher-order terms which reside in a higher-dimensional Hilbert space, the correlations and coherences are worsened.

5.2 Projections onto subsystems

The Dicke state $D_6^{(3)}$ can also be used as a resource for other interesting and entangled states. This is achieved by projecting out some qubits in a specific way as will be described below and can be seen for four-photon states in Table 5.2. The remaining qubits are then found to be in specific, useful target states. The remarkable thing is that the states obtainable by out-projection belong to different entanglement classes, meaning that they cannot be converted into each other through SLOCC (see Section 1.4.3). Our produced D_6^3 state can provide a resource for lower-dimensional states where one can navigate through state space and choose flexibly the desired state without the need to modify the setup. This connotes an advantage over experiments starting out already with a lower-dimensional state where the produced state can only be transformed within its equivalence class.

Our setup relies on post-selection, meaning that an event is only recorded when each spatial mode is occupied with the additional condition that not both polarised modes of any spatial mode are populated. Post-selection ensures that the probabilistic splitting of the photons succeeded. Without post-selection the desired four-photon states is only obtained with a probability of $p = \frac{4!}{6^4} \approx 0.019$ when qubit 1 and 2 have the specified outcome displayed in Table 5.2. For the five-photon state the probability is reduced to $p \approx 0.015$.

5.2.1 Five-photon Dicke state

As any Dicke state can be written as

$$|D_N^{(m)}\rangle = (C_N^m)^{-1/2}\left(\left(C_{N-1}^{m-1}\right)^{1/2}|H\rangle\,|D_{N-1}^{(m-1)}\rangle + \left(C_{N-1}^{m}\right)^{1/2}|V\rangle\,|D_{N-1}^{(m)}\rangle\right), \tag{5.7}$$

where C_i^j is the binomial coefficient, projecting out Hs and Vs allows to navigate through the Dicke space. Figure 5.6 shows how to project H and V polarised photons out in order to navigate through the Dicke class. Any $D_N^{(m)}$ state can be

Qubit 1, 2	State
H H	$\overline{W}$
H V V H	$D_4^{(2)}$
V V	W
P M M P	GHZ

Table 5.2: By projecting the first two qubits as shown in the first column, the remaining four qubits are projected into the states shown in the second column.

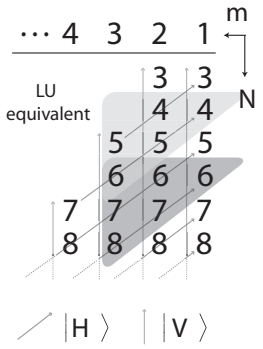

Figure 5.6: Starting out from a higher-dimensional Dicke state $D_N^{(m)}$, the figure shows which lower-dimensional Dicke states can be obtained by projecting out Vs, which moves the state up and Hs, resulting in step wise up and left.

easily transformed into a $D_N^{(N-m)}$ by means of *local unitary transformations* (LU) on the individual qubits.

Two states are obtained by projecting the first qubit onto the H/V basis, namely the $D_5^{(2)}$ when the first qubit gives H and accordingly $D_5^{(3)}$ when it is V. The two states are equivalent under the following local unitary transformations: $\left|D_5^{(3)}\right\rangle = \sigma_x^{\otimes 5}\left|D_5^{(2)}\right\rangle$. The first few of the ten components are:

$$\left|D_5^{(2)}\right\rangle = \frac{1}{\sqrt{10}}\left(|HHVVV\rangle + |HVVVH\rangle + |VVVHH\rangle + |HVHVV\rangle + \ldots\right). \tag{5.8}$$

Spin-squeezing witness for five-photon Dicke state

Analogous to Section 5.1.1, the maximal witness for biseparable states is $\langle \mathcal{W}_{SS}\rangle_{BS}^{\max} = 7.87$ and so the spin-squeezing witness for $\left|D_5^{(2)}\right\rangle$ is:

$$\langle \mathcal{W}_{SS}\rangle = 7.87 - \langle J_x^2 + J_y^2\rangle, \tag{5.9}$$

Measuring this witness experimentally leads to:

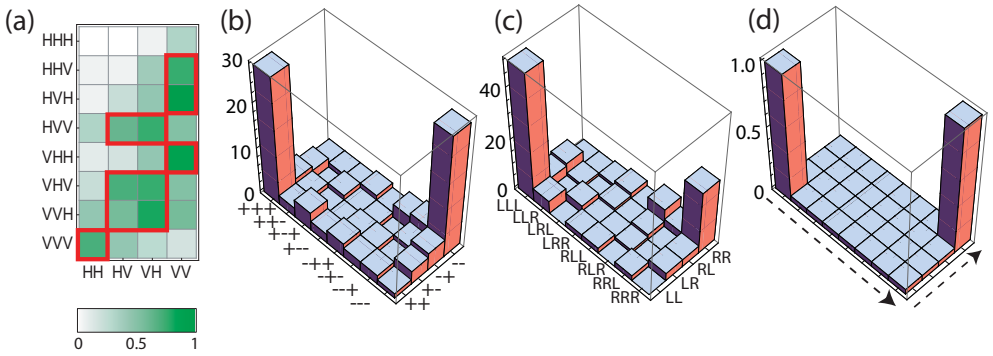

Figure 5.7: The experimental five-photon coincidence pattern for the LMS (a) Z, (b) X and (c) Y are shown. (d) The expected ideal pattern for the latter two LMS is displayed. The populations for the ideal five-photon Dicke state in the Z basis are indicated through the red boxes and are 1.0.

$$\langle \mathcal{W}_{\mathbf{SS}} \rangle_{\mathbf{BS}}^{\max} - \langle \mathcal{W}_{\mathbf{SS}} \rangle_{\mathbf{D_5^{(2)}}} = \mathbf{-0.21 \pm 0.04}. \tag{5.10}$$

Thanks to the good two-qubit correlations the J_z^2-term could be justifiably omitted opposed to the six-photon Dicke state. So only two LMS measurements were needed to prove GME. Their outcome is presented in Figure 5.7. Due to the symmetry of the $\left|D_6^{(3)}\right\rangle$, the choice which qubit should be projected out is completely arbitrary. To demonstrate this experimentally, we projected also the sixth qubit instead of the first one into the H/V basis. Also in this case the evaluation proved GME:

$$\langle \mathcal{W}_{\mathbf{SS}} \rangle_{\mathbf{BS}}^{\max} - \langle \mathcal{W}_{\mathbf{SS}} \rangle_{\mathbf{D_5^{(2)}}} = \mathbf{-0.32 \pm 0.02}. \tag{5.11}$$

5.2.2 Symmetric four-photon Dicke state

Following the scheme and projecting qubit one and two onto H_1V_2 or V_1H_2 leaves the remaining four qubits in a four-photon Dicke state:

$$\left|D_4^{(2)}\right\rangle = \frac{1}{\sqrt{6}} \left(|HHVV\rangle + |HVVH\rangle + |VVHH\rangle + |VHHV\rangle + |HVHV\rangle + |VHVH\rangle\right). \tag{5.12}$$

So far the $D_4^{(2)}$ using photons has only been produced directly in experiment [42]. This state is also resistant against projective measurements and also photon loss as the loss of one qubit leaves the remaining still genuine multipartite entangled.

Spin-squeezing witness for symmetric four-photon Dicke state

Analogous to Section 5.1.1 the spin-squeezing witness for $D_4^{(2)}$ is:

$$\langle \mathcal{W}_{SS} \rangle = 5.23 - \langle J_x^2 + J_y^2 \rangle. \tag{5.13}$$

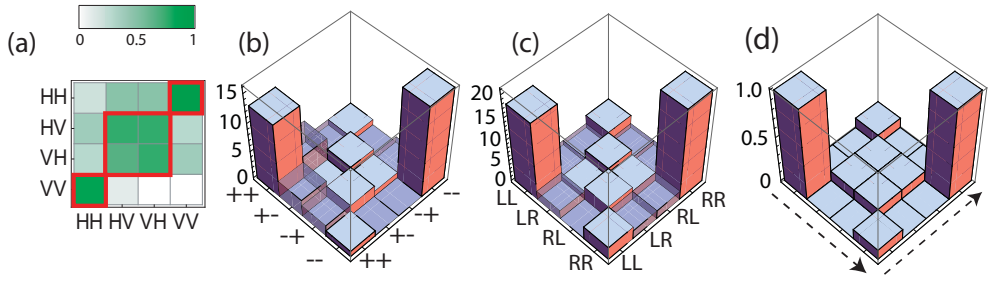

Figure 5.8: The experimental four-photon Dicke state coincidence pattern for the LMS (a) Z, (b) X and (c) Y are shown. (d) The expected ideal pattern for the latter two LMS is displayed. The populations for the ideal $D_4^{(2)}$ state in the Z basis are indicated through the red boxes and are 1.0.

X	X+Z	Y-Z
Y	X-Z	X+Y
Z	Y+Z	X-Y

Table 5.3: Similar to the six-photon fidelity evaluation, the 9 LMS for the $D_4^{(2)}$ case are given. Again normalisations are omitted. Without the last two LMS it is also sufficient for the fidelity measurement of the W state. The fidelity for GHZ_4 is obtained already through the first 5 LMS.

The value on the beginning of the right hand side is given by the maximal expectation value for biseparable states: $\langle \mathcal{W} \rangle_{BS}^{\max} = 5.23$.

The correlations were sufficiently large and gave a value of

$$\langle \mathcal{W}_{\mathbf{SS}} \rangle = \mathbf{-0.16 \pm 0.07}, \tag{5.14}$$

which clearly shows genuine multipartite entanglement for the $D_4^{(2)}$ state. Again no additional J_z^2 was needed and demanding only two local measurement settings. The experimentally obtained coincidence patterns for the two local measurement settings required for obtaining the witness can be found in Figure 5.8.

Fidelity for symmetric four-photon Dicke state

The fidelity measurement for the $D_4^{(2)}$ required 9 LMS which can be found in Table 5.3. The outcome is found to be

$$\mathbf{F = 0.66 \pm 0.05}. \tag{5.15}$$

5.2.3 Four-photon W and $\overline{W}$ state

Like in the case of the $D_4^{(2)}$ state, we once again project the first two qubits into the H/V basis, but this time, when qubit one and two both give H, then the remaining four qubits form a W state. This state can also be called $D_4^{(1)}$. In the case when they both give V, a $\overline{W} = D_4^{(3)}$ state is prepared:

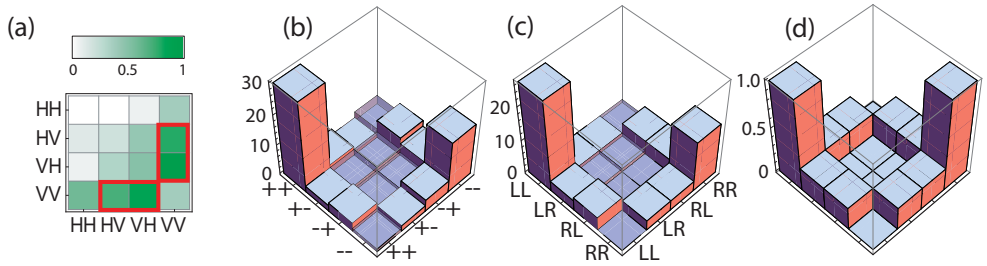

Figure 5.9: The experimental four-photon W coincidence pattern for the LMS (a) Z, (b) X and (c) Y are shown. The non-ideal contributions are displayed transparently. (d) Furthermore the expected ideal pattern for the latter two LMS is displayed. The populations for the ideal W state in the Z basis are indicated through the red boxes and are 1.0.

$$|W\rangle = \frac{1}{\sqrt{4}}\left(|VVVH\rangle + |VVHV\rangle + |VHVV\rangle + |HVVV\rangle\right), \tag{5.16}$$

$$|\overline{W}\rangle = \frac{1}{\sqrt{4}}\left(|HHHV\rangle + |HHVH\rangle + |HVHH\rangle + |VHHH\rangle\right). \tag{5.17}$$

W and $\overline{W}$ are only produced each at half the rate compared to $D_4^{(2)}$ and GHZ but one could quite easily transform them into each other: $|W\rangle = \sigma_x^{\otimes 4}\left|\overline{W}\right\rangle$. This can be realised by applying a HWP set at 45 degrees to each of the four arms.

An ideal state would not be detectable as it would not exceed the four-qubit biseparable bound but due to the imperfections already mentioned, GME could still be proven experimentally:

$$\langle\mathcal{W}\rangle_{\mathbf{BS}}^{\max} - \langle\mathcal{W}\rangle_{\mathbf{W}} = \mathbf{-0.2 \pm 0.1}. \tag{5.18}$$

The experimentally obtained coincidence patterns for the two LMS needed for obtaining the witness are shown in Figure 5.9.

Additionally the fidelity was evaluated which turned out to be

$$\mathbf{F = 0.62 \pm 0.02}. \tag{5.19}$$

For this measurement only 7 LMS were needed [53], which are the same as for $D_4^{(2)}$ but without the need for X+Y and X-Y (see Table 5.3). Hence it was not necessary to perform additional measurements.

5.2.4 Four-photon GHZ state

The Greenberger-Horne-Zeilinger state or short GHZ state is a complementary class to the W and $\overline{W}$ states. It also belongs to the class of cluster states. The GHZ state contains genuine n-party entanglement. It can also be written as a sum of two Dicke states:

$$\begin{aligned} |GHZ\rangle &= \frac{1}{\sqrt{2}}(\left|D_4^{(0)}\right\rangle + \left|D_4^{(4)}\right\rangle) \\ &= \frac{1}{\sqrt{2}}(|HHHH\rangle + |VVVV\rangle). \end{aligned} \tag{5.20}$$

In the experiment we actually produced a locally equivalent state $\frac{1}{\sqrt{2}}(\left|D_4^{(1)}\right\rangle - \left|D_4^{(3)}\right\rangle)$ but it can be transformed into GHZ by applying $H\sqrt{\sigma_z}$ to all qubits and an additional σ_z to the first qubit.

The fidelity of the state is obtained through the first five LMS in Table 5.3 [53] and with its connection to the projection based witness from Equation 1.22 also GME could be proven:

$$\mathbf{F = 0.56 \pm 0.02}, \tag{5.21}$$

$$\langle \mathcal{W} \rangle = \mathbf{-0.06 \pm 0.02}. \tag{5.22}$$

5.3 Quantum protocols

In this section it is shown how the setup can also be used to perform *quantum protocols*, which enable interesting realisations of different networking tasks and applications from different areas like quantum cryptography and communication. Especially teleportation, telecloning and quantum secret sharing are very useful for quantum networks which gain a lot of attention from the community.

5.3.1 Open-destination teleportation and telecloning

Teleportation is a scheme which allows to transmit a desired state ϕ and hence information from a sender A to a receiver B. They share an entangled pair and have access to a classical channel [54]. The sender has to perform a Bell measurement on the subsystem formed by the state ϕ, to be transmitted and its particle of the entangled pair. A then sends the measurement outcome to B over a classical channel. With this information, B can transform its particle to be in the state ϕ.

Open-destination teleportation [55] extends this idea by providing the flexibility of choosing one out of N receivers to whom the state will actually transported. As there are more than two parties involved this can be seen as a quantum network. Whereas teleportation is a transport of information which removes all information about the transmitted state from the sender during this process, cloning aims at distributing information. More precisely quantum cloning is a mechanism to copy information from M senders to N receivers. But quantum mechanics does not allow perfect copies which is formulated in the *no-cloning theorem* [56] so the copies can only be accurate to a certain degree.

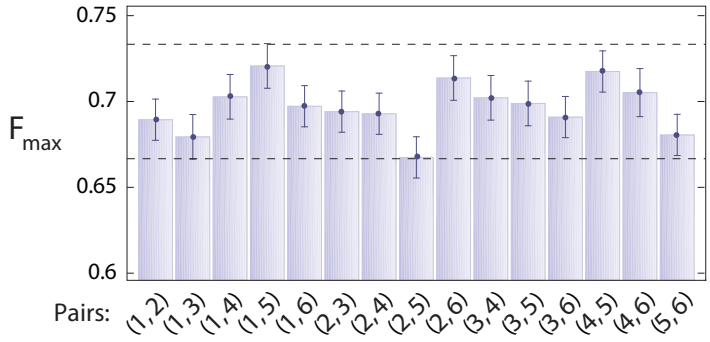

Figure 5.10: Here the experimentally achievable maximal fidelity for each possible two-qubit channel for open destination teleportation is shown. The upper dashed line indicates the ideal value and the lower line the classical threshold.

These protocols are possible with the $D_6^{(3)}$ but first looking at the general case, a state $D_N^{(N/2)}$ is found in the two-photon state

$$\rho = \alpha_N |\psi^+\rangle\langle\psi^+| + \frac{1-\alpha_N}{2}(|HH\rangle\langle HH| + |VV\rangle\langle VV|), \quad \alpha_N = \frac{N}{2(N-1)} \tag{5.23}$$

after tracing out $N-2$ qubits, for $N \geq 4$. The maximal singlet fraction F_{msf} [57] is defined as the maximum of the overlap with the Bell-singlet $\langle F_{\psi^-}\rangle$ under LOCC. The maximum fidelity achievable for teleporting when using ρ as a channel is [58]

$$F_{\max} = \frac{2N-1}{3(N-1)}. \tag{5.24}$$

For our six-photon Dicke state $\langle F_{\psi^-}\rangle = \alpha$ as the two Bell-states are equivalent under LOCC. The maximally achievable teleportation fidelity for six qubits results in $F_{\max} = 0.7\dot{3}$. Any photon pair of our state can be used as a teleportation channel which enables symmetric telecloning with the fidelity limit of $F_{\max}$. As this limit $F_{\max}$ is equal to the limit for universal $1 \to (N-1)$ cloning the $D_6^{(3)}$ is a natural resource for *optimal* symmetric quantum cloning. The experimentally obtained values for any pair can be seen in Figure 5.10 which clearly exceeds the classical limit of 2/3 [59]. Telecloning is now done by making a Bell measurement on the state formed by the state $|\psi\rangle$ to be cloned and the qubit from the $D_6^{(3)}$ of party A (see Figure 5.11). A Bell measurement (BM) is a projection onto one of the four Bell-states defined in Section 1.16. The result of the BM is then forwarded to the other parties who obtain their cloned states by applying local transformations on their qubit conditional on the result. When the other parties cooperate and choose to measure their $N-2$ photons in the H/V basis ρ is projected onto the subspace formed by $\{|HH\rangle, |VV\rangle\}$ or $\{|HV\rangle, |VH\rangle\}$. Hence a perfect channel $|\psi^+\rangle$ is created with the success probability α_N.

One can now choose between telecloning and teleportation [42] with the success probability for the latter on to be $p_s = \alpha_N \geq \frac{1}{2}$. For our Dicke state the ideal value

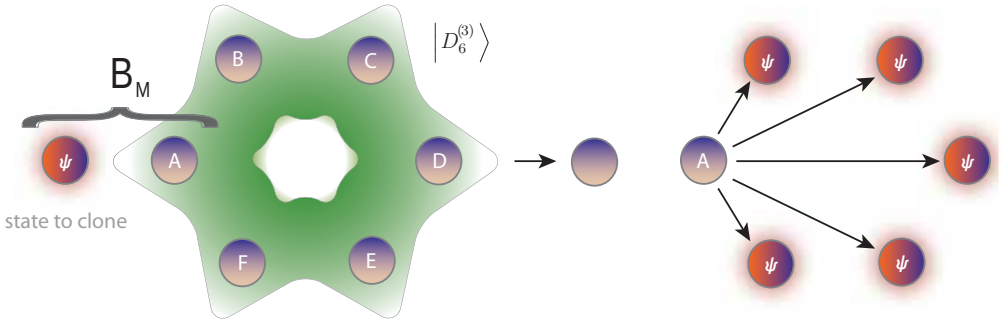

Figure 5.11: Telecloning scheme with the $D_6^{(3)}$: By a Bell measurement on the product of the state ψ with qubit at A, information about ψ can be read out by the remaining parties B-F when acknowledging the outcome. Due to the symmetry involved any qubit can be used for the Bell measurement.

is $p_s = 0.6$ and the experimentally obtained mean value is

$$\bar{\mathbf{p}}_\mathbf{s} = \mathbf{0.55 \pm 0.02}. \tag{5.25}$$

As an example, we chose photons 5 and 6 to form a channel and we found experimentally a mean fidelity of

$$\langle \bar{\mathbf{F}}_{\psi^+} \rangle_{\rho_\mathbf{exp}} = \mathbf{0.71 \pm 0.02}. \tag{5.26}$$

5.3.2 Quantum secret sharing

Secret sharing is a very well known problem in cryptography. It centres around the problematic of different parties which are not to be fully trusted or without the given authority to perform tasks. Instead they gain permission or access only on condition of full cooperation. A famous variant features a few (N) vice-presidents of a bank who need access to the presidents vault during his absence. But access should only be granted when all (or more than a specified number) of them agree. This can be achieved by distributing different keys to each party which do not offer access on their own. But through a suitable algorithm which takes use of all (or possible a large enough subgroup of) keys grants access.

The problem can be generalised to arbitrary number of people forming access sets, in the above example with $N = 3$ only one such set exists which is formed by the three vice-presidents together. It could be modified such that only two persons needed to access the vault which results in three sets. Besides these access sets and non-access sets there can also exist semi-access sets which can obtain partial info about the secret. This is only mentioned for completeness and will not be discussed here. It only needs to be addressed for realisations, in the following case post-processing guarantees that the semi-access set is empty.

There are many classical realisations and protocols for this problem. A very simple one is the following, designed for three parties: Party A and B get a key

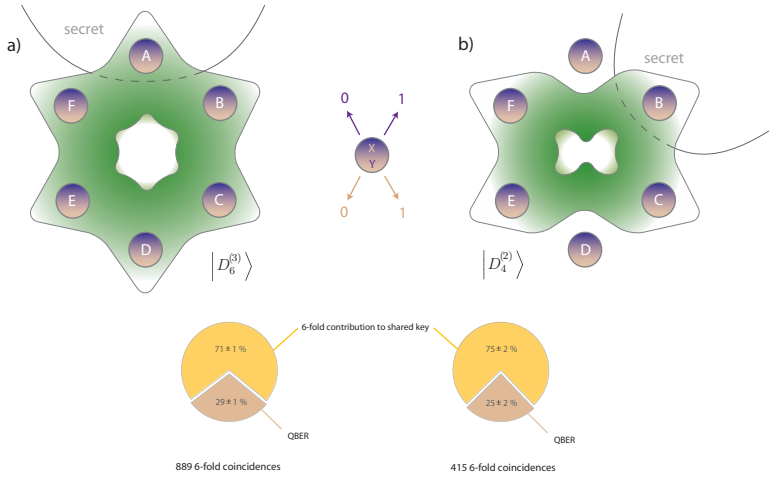

Figure 5.12: Quantum secret sharing scheme for (a) the $D_6^{(3)}$ where qubit A contains the secret which can only be obtained through cooperation of the other five parties. (b) To obtain the $D_4^{(2)}$, qubits A and D are projected onto H and V. Parties C,E and F can reconstruct the key held by B. As this scheme is symmetric, the roles of any party can be exchanged. Below the results are shown for both cases.

each containing random trits such like: `02211020`.... The key distributed to party C is then determined such that the correct key giving access is the sum of all three keys: $x_i = (a \oplus b \oplus c)_i \text{mod} 3$. This example is easily expandable for d-parties by taking qudits and the summation mod(n).

For securing this scheme against eavesdropper the communication of this classical scheme can done via a quantum secret channel using for example the famous BB84-protocol. But the trade-off is a large overhead as many bits and qubits need to be transmitted, once for securing and again for the scheme itself. The solution is combining the secure channel with the secret sharing distribution. Multipartite entangled systems prove to be very usable [60, 61]. We now show that our Dicke setup also offers such an implementation as the distribution of six qubits can be understood as the distribution of keys for $N-1$ parties. It uses the fact of perfect correlations in the maximally conjugate bases of σ_x and σ_y which give $\langle \sigma_{x,y}^{\otimes N} \rangle_{D_N^{N/2}} = 1$. For one bit of the keys a $D_N^{N/2}$ gets sent through our setup and each party obtains one qubit. Each receiving party announces publicly which of the two maximally conjugated bases (X or Y) was used for the measurement. Alice, the secret keeper then announces when the measurement bases were the same and which qubits are thus kept to form the sifted key. The parties $i = 2, .., N$ are only able to obtain the correct key when cooperating as the key is given by $x_1 = \oplus_{i=2}^{N} x_i$ (analogous for the Y basis). The usage of two measurement bases allows for the detection of eavesdropping. Also trying to recover the key from less than $N-1$ parties is not possible. As the Dicke state is completely symmetric, any other party can be the initial one, i.e. play the role of Alice (see Figure 5.12).

To ensure that a smaller subset of the full access set does not even gain some partial information about the key, post-processing can be applied [61, 62]. This ensures an empty semi-access set.

Quantum secret sharing is unidirectionally connected to quantum error correction as from a subset of qubits an unknown qubit can be determined and restored. The efficiency of a setup can be specified through the quantum bit error rate (QBER) which is defined as the ratio of the error rate to the key rate and gives information about an eavesdropper and how much she can know. This scheme was evaluated for both $D_4^{(2)}$ and $D_6^{(3)}$ giving a quantum bit error rate of $\mathbf{25 \pm 2}\%$ for $N = 4$ with producing 415 shared bits and $\mathbf{29 \pm 1}\%$ for $N = 6$ with 889 shared bits.

5.4 Conclusions

In this experiment we were able to realise a symmetric six-photon Dicke state. With the use of a novel, noise resistant spin-squeezing witness, entanglement could be proven with a minimum of local measurement settings. With a very extensive measurement series we further obtained the fidelity for the $D_6^{(3)}$, which is close to the ideally predicted case and can be approximated by our comprehensive simulations. The behaviour of the two-qubit correlations is deduced from the limitations due to the higher-order effects together with the coupling imbalance as well as the detection efficiencies. Production of lower-dimensional states was also done in a methodical way by the appropriate projections of qubits. The obtained states included the five-qubit Dicke state for which genuine multipartite entanglement was demonstrated. This was done by the use of SSW but without the need of noise resistance. Additionally the four-photon states produced included the symmetric four-photon Dicke state $D_4^{(2)}$, the W and $\overline{W}$ state and the GHZ_4 state. For every one of them GME was proven and their fidelities have been obtained. The remarkable feature of this projection onto lower-dimensional state is that they belong to different equivalence classes which cannot be easily converted (that is by means of LOCC) into each other. However, starting out with the $D_6^{(3)}$ and measuring some qubits in a specific way circumvents this and allows to flexibly choose a desired lower particle-number state without any experimental modification.

Our setup could demonstrate the application for different quantum information protocols. Open-destination teleportation and quantum telecloning can be realised with the symmetric six-qubit Dicke state allowing to transmit information between two arbitrary parties respectively from any one to the others. Our $D_6^{(3)}$ state can be used as a resource for another quantum network application: Quantum secret sharing, where knowledge about one qubit holding the key can be obtained from the remaining ones, distributed among different parties who are forced to collaborate.

Chapter 6

Conclusion

In this work an experiment was presented which allows production of a photonic six-qubit Dicke state by using a very stable, all-optical setup. This advance into higher particle-number quantum states is a necessary step for quantum applications and protocols like quantum computation.

General multipartite entanglement was verified by using novel noise resistant spin-squeezing witness which allowed probing with, for high-particle states, reasonable efforts. Furthermore, the six-photon state can be used as a flexible resource for lower-dimensional states. Through different projections of some qubits, the remaining ones can be found in the desired, also genuine multiparite entangled states. Choosing the appropriate projections allowed to navigate through different equivalence classes of states, a possibility not available when starting with states of the same dimensionality. For the most interesting states the fidelity was evaluated.

This setup is sensitive to higher-order emissions of the SPDC process, so also their influence is carefully looked at by using both, analytical and numerical simulations. Additionally, it provides an ideal tool for investigating different decoherence mechanisms.

The very low count rate of five events per hour showed how much this experiment was on the limit of feasibility. This can only be partly improved by a different layout that does not depend on a probabilistic splitting up of the photons. The normal solution of going to higher pump powers comes with the trade off of higher-order emissions that would decrease the fidelity even further. As has been analysed, good detector efficiencies are also an extremely crucial step towards more than six-qubit experiments.

But even when there are many more obstacles to overcome in the future, the road to higher particle numbers promises diverse interesting and rich applications and insights.

Acknowledgements

During the last year I have met and worked closely with great people. For that reason I consider myself to be very lucky and I want to use this opportunity to thank them all.

First of all I would like to thank Prof. Anton Zeilinger who gave me the opportunity to work in his excellent group and in the fascinating area of quantum optics.

I am very thankful to Philip Walther, Thomas Jennewein and Nathan Langford as the discussions with them were both enriching and deepening my understanding of all the different kinds of effects we observed. Also most of the analysis are based on the rewritten toolbox by Thomas Jennewein.

I also thank our collaborators at Queens University very much. The collaboration with them was a true pleasure. Special credit to Mark Tame and Mauro Paternostro for their excellent theoretical work which eased our experimental life and for their ideas of different applications.

I owe great thanks also to Robert Prevedel, who introduced me not only to the beauty of the daily laboratory work but also to tuna salad. He fostered my experimental side and was also there with sensible advice in all kind of situations I faced during the last year.

My work was always a pleasure, for which all the people from the Molekü̈le group as well as from the IQOQI were responsible, but who are too numerous to be listed here.

Furthermore I would also like to thank Stefanie Barz for comments on this work.

Naturally, I want to thank my loving and always supporting parents, Gerald and Isolde, for all their endless patience and encouragement.

Appendices

Appendix A

Published work of this thesis

The results presented in this thesis have been summarised as a publication and are given on the following pages. It has been recently published in Physical Review Letters and can also be accessed as an e-print on the ArXiv server: `http://arxiv.org/abs/0903.2212v1`. The Letter is accompanied by Supplementary Material which can also be found on the following pages.

Experimental Realization of Dicke States of up to Six Qubits for Multiparty Quantum Networking

R. Prevedel,[1] G. Cronenberg,[1] M. S. Tame,[2] M. Paternostro,[2] P. Walther,[1,3] M. S. Kim,[2] and A. Zeilinger[1,3]

[1]*Faculty of Physics, University of Vienna, Boltzmanngasse 5, A-1090 Vienna, Austria*

[2]*School of Mathematics and Physics, The Queen's University, Belfast, BT7 1NN, United Kingdom*

[3]*Institute for Quantum Optics and Quantum Information (IQOQI), Austrian Academy of Sciences, Boltzmanngasse 3, A-1090 Vienna, Austria*

(Received 12 March 2009; published 10 July 2009)

We report the first experimental generation and characterization of a six-photon Dicke state. The produced state shows a fidelity of $F = 0.56 \pm 0.02$ with respect to an ideal Dicke state and violates a witness detecting genuine six-qubit entanglement by 4 standard deviations. We confirm characteristic Dicke properties of our resource and demonstrate its versatility by projecting out four- and five-photon Dicke states, as well as four-photon Greenberger-Horne-Zeilinger and W states. We also show that Dicke states have interesting applications in multiparty quantum networking protocols such as open-destination teleportation, telecloning, and quantum secret sharing.

DOI: 10.1103/PhysRevLett.103.020503 PACS numbers: 03.67.Bg, 03.67.Mn, 42.50.Dv, 42.50.Ex

Multipartite entanglement is at the core of studies probing the foundations of quantum physics and represents a key component in a wide range of quantum-information processing tasks [1]. So far, Greenberger-Horne-Zeilinger (GHZ) [2], W [3], cluster, and graph states [4] have been studied and experimentally investigated [5]. However, other nonequivalent classes of quantum states with interesting symmetries exist [6]. In particular, Dicke states [7] provide a rich opportunity for exploring multipartite entanglement. Recent studies have focused on techniques for generating, detecting, and characterizing these states [8,9] in atomic, ion-trap, [10] and optical [11] settings.

In this Letter we report the experimental generation and investigation of a variety of multiphoton entangled states. We present a flexible linear-optics setup that can produce four-, five-, and six-photon representatives of the important class of Dicke states, as well as four-photon GHZ states. Information is encoded in the polarization degrees of freedom of entangled photons produced by high-order spontaneous parametric down-conversion (SPDC). We show that our generated states are genuinely multipartite entangled by using tailor-made and experimentally favorable witness tools. These new characterization methods are important in virtue of the nonideal nature of the six-photon state: although spurious nonlinear processes affect its quality, quantum features can still be observed and characterized. We also highlight the potential for quantum control in large Hilbert spaces by evaluating protocols such as open-destination teleportation, telecloning, and quantum secret sharing [11–15].

Experiment.—Figure 1(a) shows the setup for the generation of the three-excitation six-photon Dicke state $|D_6^{(3)}\rangle = \frac{1}{\sqrt{20}}\sum_P |HHHVVV\rangle_{123456}$. Here, $|H(V)\rangle_i$ are horizontal (vertical) polarization states of a photon in spatial mode $i = 1, \ldots, 6$, which encode the logical states of a qubit, while $\sum_P$ denotes the sum over all permutations of logical states [16]. In the setup, six photons are probabilistically distributed among the spatial modes by nonpolarizing beamsplitters (BSs): upon detecting one photon in each mode we postselectively observe $|D_6^{(3)}\rangle$. We use higher-order emissions of a collinear type-II SPDC process for the simultaneous production of three pairs of photons [17]. A Coherent Inc. Verdi V-18 laser is combined with a mode-locked Mira HP Ti:sapphire oscillator to reach the energy necessary to observe third-order SPDC emissions. The pulsed-laser output ($\tau = 200$ fs, $\lambda = 810$ nm, 76 MHz) is frequency doubled using a 2-mm-thick lithium triborate crystal, resulting in UV pulses of 1.4 W cw-average. To avoid optical damage to the antireflection coating of the lithium triborate, we continuously translate it with a stepmotor, achieving a very stable source of UV pulses (power and count-rate fluctuations less than 1%–2% over 30 h). The UV pulses are focused onto a 2-mm-thick β-barium borate (BBO) type-II crystal, cut for collinear SPDC. Dichroic mirrors separate the down-converted photons from the UV pump, and a compensator erases walk-off effects. We use high-transmittivity interference filters ($\Delta\lambda = 3$ nm) to spatially and spectrally select the photons, which are coupled to a single-mode fiber guiding them to the Dicke setup of Fig. 1(a). At 1.4 W of UV pump power, we observe $\sim$0.003 six-photon Dicke states per second. Higher power increases the sixfold rate while decreasing the fidelity due to undesired detection events from higher-order SPDC emissions [17].

State characterization.—In order to detect the presence of genuine multipartite entanglement (GME) in our experimental states, i.e., quantum entanglement shared by all the particles involved, we use collective-spin inequalities [9]. Various entanglement witnesses have been found to be well suited to the class of Dicke states [8]. They are experimentally appealing, due to the small number of local measurement settings (LMSs) required, in stark contrast to their more demanding projector-based counterparts. We start with the collective-spin witness $\langle \mathcal{W}^s \rangle_f = \langle J_x^2 + J_y^2 \rangle_f$,

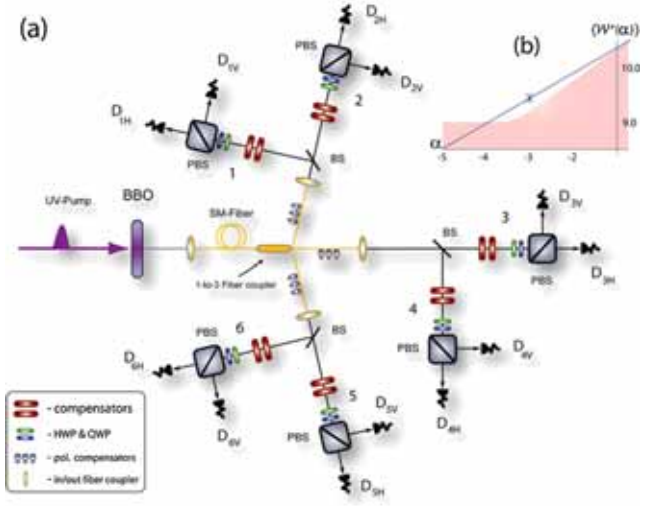

FIG. 1 (color online). (a) Setup for generating the six-photon Dicke state $|D_6^{(3)}\rangle$. Photons are distributed into modes 1,...,6 via a 1-to-3 fiber coupler, followed by 50:50 BSs. The expected probability to find one photon in each spatial mode, corresponding to the state $|D_6^{(3)}\rangle$, is $p \sim 0.015$. The fiber and BSs introduce birefringence, compensated by fiber-squeezers and birefringent crystals. State characterization is performed via polarization analysis of sixfold coincidences by a quarter-wave plate (QWP), a half-wave plate (HWP), and a polarizing beam splitter (PBS), whose output ports are monitored by multimode fiber-coupled single-photon detectors. Each detector signal enters a coincidence logic that records multiphoton coincidences. (b) Biseparability region (shaded) for $\langle \mathcal{W}^s(\alpha)\rangle_{bs}$ and experimental point (predicted line) for $\langle \mathcal{W}^s(\alpha)\rangle_{\varrho_6^{(3)}}$.

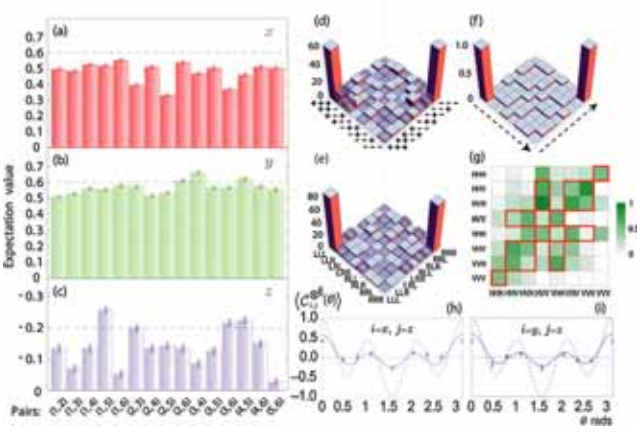

FIG. 2 (color online). Experimental study of the six-photon Dicke state $\rho_6^{(3)}$. (a)–(c) Correlations $\langle \sigma_i^{(j)} \sigma_i^{(k)} \rangle$ for qubit pairs (j, k) $(i = x, y, z)$ for $\langle \mathcal{W}^s(\alpha)\rangle$. Dashed lines are ideal values. (d), (e), and (g) Coincidences for photons measured in $|\pm\rangle = (|H\rangle \pm |V\rangle)/\sqrt{2}$, $|L \text{ or } R\rangle = (|H\rangle \pm i|V\rangle)/\sqrt{2}$, and $|H \text{ or } V\rangle$ (rescaled). (f) Ideal populations for (d) and (e). (h) and (i) Multiphoton correlations. Dashed (solid) lines are the patterns of $\langle \mathcal{C}^{\otimes 6}_{x/y,z}(\theta)\rangle$ for $|D_6^{(3)}\rangle$ (ρ_{sim}). The dots are experimental points.

where f refers to the state over which the expectation value is calculated. Here, $J_i = \frac{1}{2}\sum_{k=1}^{N} \sigma_i^{(k)}$ $(i = x, y, z)$ are collective-spin operators of N qubits with label k, and $\sigma_i^{(k)}$ denotes the i Pauli operator. By using the techniques described in Ref. [18], it can be seen that for any six-qubit biseparable (bs) state $\langle \mathcal{W}^s\rangle_{bs} \leq 11.02$, so that $\langle \mathcal{W}^s\rangle_f > 11.02$ will detect the presence of GME in f. However, due to the nonideal two-qubit correlations upon which $\mathcal{W}^s$ depends [shown in Figs. 2(a) and 2(b) for $\langle J_x^2\rangle$ and $\langle J_y^2\rangle$], our experimental state $\varrho_6^{(3)}$ gives $\langle \mathcal{W}^s\rangle_{\varrho_6^{(3)}} < 11.02$. To obtain a witness that detects GME for a nonideal state, we insert a term proportional to J_z^2, for which $\langle J_z^2\rangle_{D_6^{(3)}} = 0$. This gives the more general witness $\mathcal{W}^s(\alpha) = J_x^2 + J_y^2 + \alpha J_z^2$ $(\alpha \in \mathbb{R})$. We then search for values of α such that $\langle \mathcal{W}^s(\alpha)\rangle_{\varrho_6^{(3)}} > \langle \mathcal{W}^s(\alpha)\rangle_{bs}$. In Fig. 2(c) we show the two-qubit correlations for $\langle J_z^2\rangle_{\varrho_6^{(3)}}$, which contribute to $\langle \mathcal{W}^s(\alpha)\rangle$ shown in Fig. 1(b). A range of α exists where $\langle \mathcal{W}^s(\alpha)\rangle_{\varrho_6^{(3)}} > \langle \mathcal{W}^s(\alpha)\rangle_{bs}$: the gap is optimized at $\alpha = -3$, where $\langle \mathcal{W}^s(\alpha)\rangle_{bs}^{\max} - \langle \mathcal{W}^s(\alpha)\rangle_{\varrho_6^{(3)}} = -0.24 \pm 0.06$, thus confirming GME for our experimental state.

We now further probe the features of $\varrho_6^{(3)}$ and consider the multiphoton correlator $\mathcal{C}_{i,j}^{\otimes N}(\theta) = (\cos\theta\sigma_i + \sin\theta\sigma_j)^{\otimes N}$. This allows the sampling of N-photon correlations in orthogonal planes of the single-qubit Bloch sphere, providing important information about the off-diagonal elements of the density matrix and thus its coherence properties. One finds $\langle \mathcal{C}_{i,z}^{\otimes 6}(\theta)\rangle_{D_6^{(3)}} = [3\cos(2\theta) + 5\cos(6\theta)]/8$, for $i = x$, y. Only the coherences within the Dicke state are responsible for the interference between the trigonometric functions in $\langle \mathcal{C}_{i,z}^{\otimes 6}(\theta)\rangle_{D_6^{(3)}}$ [17,19]. In Figs. 2(h) and 2(i) we compare the ideal coherence signature with that of $\varrho_6^{(3)}$, finding a reduced visibility. We also compare $\varrho_6^{(3)}$ with the behavior of the state ρ_{sim} resulting from a detailed simulation of our setup including multiple-pair emissions and losses [17]. The simulated state spans a Hilbert-space sector which is larger than the 2^6-dimensional space of $|D_6^{(3)}\rangle$. Moreover, the presence of spurious state components in ρ_{sim} affects the ideal populations and coherences, as shown in Ref. [17]. The accuracy of the simulation is confirmed by the behavior of $\langle \mathcal{C}_{i,j}^{\otimes 6}(\theta)\rangle_{\rho_{\text{sim}}}$ shown in Figs. 2(h) and 2(i), revealing good agreement with our data. Our analysis of $\varrho_6^{(3)}$ is strengthened by evaluating the state fidelity $\langle F_{D_6^{(3)}}\rangle_{\varrho_6^{(3)}}$, where the projector $F_{D_6^{(3)}} = |D_6^{(3)}\rangle\langle D_6^{(3)}|$ is decomposed into 544 terms involving Pauli operators, requiring 21 LMSs for their evaluation [20]. We find $\langle F_{D_6^{(3)}}\rangle_{\varrho_6^{(3)}} = 0.56 \pm 0.02$, which agrees well with the value 0.61 from ρ_{sim}. The small discrepancy is due to slightly asymmetric fiber coupling of $|H \text{ or } V\rangle$ due to SPDC birefringence. The setup performances are thus limited by noise from higher-order emissions [17]. Despite such clearly consistent results, the measured fidelity prevents us from unambiguously claiming that our generated state is Dicke-class [21]. As full state tomography is experimentally prohibitive, we complement the fidelity analysis with additional characterization tools.

We now explore the nested structure of Dicke states and their persistence of entanglement by conditionally generating four- and five-photon entangled states via projections of $|D_6^{(3)}\rangle$ [11,22]. For example, by measuring one photon in $|H\rangle$, the five-photon state $|D_5^{(2)}\rangle$ [16] is projected out. This state is equivalent to $\sigma_x^{\otimes 5}|D_5^{(3)}\rangle$, showing that navigation through the Dicke class of states is possible via projections and local operations. Indeed, one can write $|D_N^{(m)}\rangle = (C_N^m)^{-1/2}[(C_{N-1}^{m-1})^{1/2}|H\rangle|D_{N-1}^{(m-1)}\rangle + (C_{N-1}^m)^{1/2}|V\rangle|D_{N-1}^{(m)}\rangle]$ and navigate as shown in Fig. 3(m). We start by experimentally projecting out the five-photon state $\varrho_5^{(2)}$ in modes 2,...,6 [Figs. 3(a)–3(f) show the experimental data]. For five-qubit states we have $\langle \mathcal{W}^s\rangle_{bs} \leq 7.87$ [18], giving $\langle \mathcal{W}^s\rangle_{bs}^{\max} - \langle \mathcal{W}^s\rangle_{\varrho_5^{(2)}} = -0.21 \pm 0.04$, thus detecting GME. To check consistency, we also projected photon 6 in $|H\rangle$, finding $\langle \mathcal{W}^s\rangle_{bs}^{\max} - \langle \mathcal{W}^s\rangle_{\varrho_5^{(2)}} = -0.32 \pm 0.02$.

Next, we project out the four-photon Dicke state $|D_4^{(2)}\rangle$ [16] by measuring one photon in $|H\rangle$ and another in $|V\rangle$. Using $\langle \mathcal{W}^s\rangle_{bs} \leq 5.23$ [8], the correlations for the experimental state $\varrho_4^{(2)}$ in modes 3,...,6 [shown in Figs. 3(g)–3(l)] give $\langle \mathcal{W}^s\rangle_{bs}^{\max} - \langle \mathcal{W}^s\rangle_{\varrho_4^{(2)}} = -0.16 \pm 0.07$, thus detecting GME. Moreover, we have evaluated the state fidelity $\langle F_{D_4^{(2)}}\rangle_{\varrho_4^{(2)}} = 0.66 \pm 0.05$ using 9 LMSs [23]. We complete our study of four-photon Dicke states by assessing a four-photon W state $|D_4^{(1)}\rangle$ (equivalent to $\sigma_x^{\otimes 4}|D_4^{(3)}\rangle$), generated from $|D_6^{(3)}\rangle$ upon measurement of two photons in $|H\rangle$. Experimentally, we project the state $\varrho_4^{(1)}$ into modes 3,...,6 [coincidence counts shown in Figs. 4(a)–4(d)]. Although $|D_4^{(1)}\rangle$ does not exceed $\langle \mathcal{W}^s\rangle_{bs}^{\max}$, for our experimental state we find $\langle \mathcal{W}^s\rangle_{bs}^{\max} - \langle \mathcal{W}^s\rangle_{\varrho_4^{(1)}} = -0.2 \pm 0.1$ due to $\langle J_{x,y}^2\rangle$ being slightly larger than their ideal values, thus detecting GME. We further characterize $\varrho_4^{(1)}$ by evaluating $\langle F_{D_4^{(1)}}\rangle_{\varrho_4^{(1)}} = 0.62 \pm 0.02$, using 7 LMSs [24]. Finally, a state locally equivalent to $|\mathrm{GHZ}_4\rangle = (1/\sqrt{2}) \times [|H\rangle^{\otimes 4} + |V\rangle^{\otimes 4}]$ can also be generated from $|D_6^{(3)}\rangle$ by measuring one photon in $|+\rangle$ and another in $|-\rangle$. Ideally, this produces $(|D_4^{(1)}\rangle - |D_4^{(3)}\rangle)/\sqrt{2} \equiv \sigma_z^{(1)}(\mathcal{H}\sqrt{\sigma_z})^{\otimes 4}|\mathrm{GHZ}_4\rangle$ ($\mathcal{H}$ is the Hadamard gate). The state fidelity (using 5 LMSs) is $\langle F_{\mathrm{GHZ}_4}\rangle_{\varrho_{\mathrm{GHZ}}} = 0.56 \pm 0.02$, giving a projector-based witness value of $\langle \mathcal{W}\rangle_{\mathrm{GHZ}} = -0.06 \pm 0.02$ [24], thus confirming GME.

Quantum protocols.—Despite the nonideal value of the state fidelity, the symmetries within our six-photon resource make it suitable for several key quantum-networking protocols [11,14], some of which have been demonstrated in four-photon settings. Tracing out $N-2$ qubits, one finds the two-photon state $\rho = \alpha_N|\psi^+\rangle \times \langle\psi^+| + (1-\alpha_N)[|HH\rangle\langle HH| + |VV\rangle\langle VV|]/2$ with $\alpha_N = N/[2(N-1)]$ for $N \geq 4$ [9] and $|\psi^\pm\rangle = (|HV\rangle \pm |VH\rangle)/\sqrt{2}$. Here, the maximal singlet fraction F_{msf} [25], given by the maximum of $\langle F_{\psi^-}\rangle$ under local operations and classical communication, helps in assessing the usefulness of ρ for networking tasks. We consider using ρ as a teleportation channel [11,14], where the maximum fidelity achievable for teleporting an arbitrary state is $F_{\max} = (2F_{\mathrm{msf}} + 1)/3$. For $|D_N^{(N/2)}\rangle$, $F_{\mathrm{msf}} = \alpha_N$; thus $F_{\max} = \frac{2N-1}{3(N-1)}$. Figure 4(e) shows $F_{\max}$ for all pairs of photons from $\varrho_6^{(3)}$ and the ideal value 0.73 (upper dashed line). As any photon pair in $|D_6^{(3)}\rangle$ provides a channel for teleportation, regardless of operations applied to the others, one can

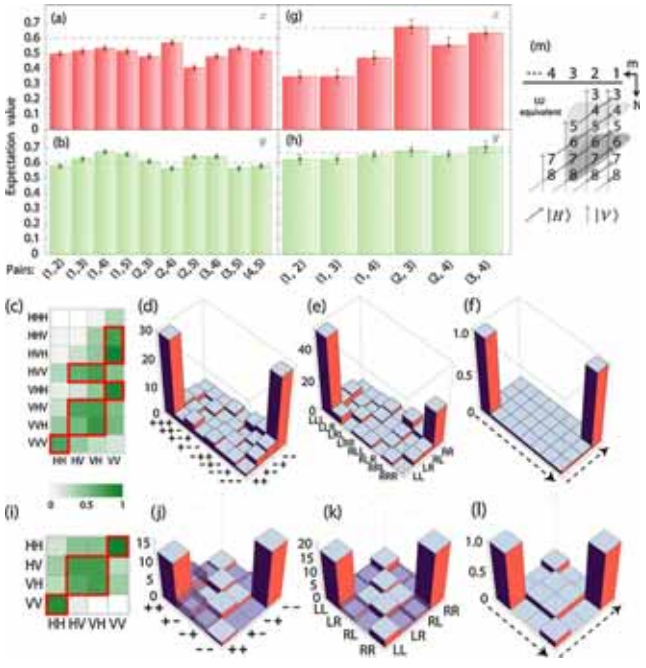

FIG. 3 (color online). Experimental data for the Dicke states $\varrho_5^{(2)}$ and $\varrho_4^{(2)}$. (a) and (b) [(g) and (h)] Correlations $\langle \sigma_i^{(j)}\sigma_i^{(k)}\rangle$ for qubit pairs (j, k) of $\varrho_5^{(2)}$ ($\varrho_4^{(2)}$), with $i = x, y$. (c)–(e) [(i)–(k)] Coincidences for the five (four) photons measured in $|H$ or $V\rangle$, $|\pm\rangle$, and $|L$ or $R\rangle$. (f) [(l)] Ideal populations for $|\pm\rangle$ and $|L$ or $R\rangle$. (m) Navigating the Dicke class by measurement.

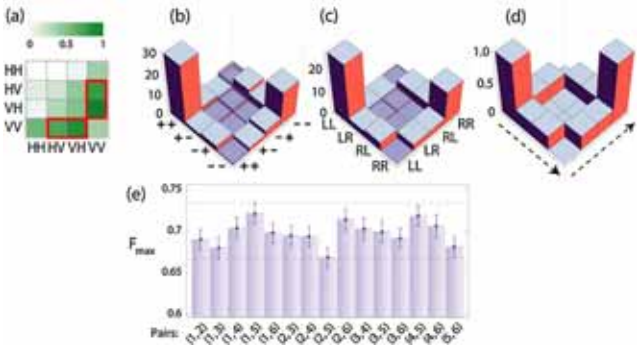

FIG. 4 (color online). Experimental data for the W state $\varrho_4^{(1)}$. (a)–(c) Coincidence counts for $\varrho_4^{(1)}$ in the rescaled $|H/V\rangle$, $|\pm\rangle$, and $|L/R\rangle$ bases. (d) Ideal populations for (b) and (c). (e) Maximum achievable fidelity $F_{\max}$ using pair (i, j) as a channel. The upper (lower) line shows the ideal (classical) value.

use it for telecloning [11–13]. The fidelity limit for universal symmetric $1 \rightarrow (N-1)$ cloning is exactly $F_{\max}$ [13]; thus $|D_N^{(N/2)}\rangle$ is an ideal resource for this task. Following [12], we have evaluated the protocol using $\varrho_6^{(3)}$: Fig. 4(e) shows that the maximum cloning fidelity achievable is consistently above the classical threshold of 2/3 [13]. A perfect $|\psi^+\rangle$ channel for teleportation can be created, with success probability α_N, if $N-2$ photons are measured out of $|D_N^{(N/2)}\rangle$ in the $|H/V\rangle$ basis. This is in contrast to telecloning, where the photons are traced out, resulting in an imperfect channel with fidelity $\langle F_{\psi^+}\rangle_\rho = \alpha_N$. As the core operation needed for telecloning commutes with the $|H$ or $V\rangle$ measurements, one can choose between telecloning and teleportation [11], with the success probability to teleport to any one party given by $p_s = \alpha_N \geq \frac{1}{2}$. Thus $|D_6^{(3)}\rangle$ can be used for open-destination teleportation [11,14]. For $\varrho_6^{(3)}$ we find a mean value $\bar{p}_s = 0.55 \pm 0.02$ very close to the ideal $p_s = 0.6$. As an example, we choose photons 5 and 6, finding a mean fidelity $\langle \bar{F}_{\psi^+}\rangle_{\rho_{\text{exp}}} = 0.71 \pm 0.02$.

Finally, $|D_N^{(N/2)}\rangle$ can also be used for multiparty quantum secret sharing [15], where entanglement ensures that all parties must cooperate in order to obtain a shared secret. The trick is to exploit the perfect correlations in the maximally conjugate bases of $\sigma_{x,y}$. Using $\langle \mathcal{C}_{i,j}^{\otimes N}(\theta)\rangle$, we get $\langle \sigma_{x,y}^{\otimes N}\rangle_{D_N^{(N/2)}} = 1$. Consider the σ_x basis and $x_j \in \{0, 1\}$ as the measurement outcome for the jth photon. If photon 1 is measured, the value of x_1 can only be recovered via $x_1 = \oplus_{i=2}^N x_i$ ($\oplus$ denotes mod-2 addition), implying cooperation of parties $2, \ldots, N$. As $|D_N^{(N/2)}\rangle$ is symmetric, this applies to any choice for the initial party. The same holds for the σ_y basis. When the parties announce their (randomly chosen) bases, a shared key can be distributed [15], with which a designated party encodes the secret. Any set of less than $N-1$ parties cannot recover the key, and although subsets of parties can exist with partial information about x_1 (for instance), any such bias is removable by postprocessing [15,26]. We thus evaluated the expected quantum bit error rate of the generated key (before postprocessing), given by the average error rate of the $\sigma_{x,y}$ bases. We find $25 \pm 2\%$ and $29 \pm 1\%$ for $N = 4$ (415 shared bits) and $N = 6$ (889 shared bits), respectively, over an 82 h period.

Remarks.—We have demonstrated a linear-optics setup able to produce various states from the Dicke class and characterized their properties using new methods. We also evaluated the potential of our six-photon state for multiparty quantum networking. Our work significantly extends the range of attainable quantum states and paves the way toward the experimental study of other six-qubit entangled states [6] (and larger ones) and their use in quantum-information processing.

We acknowledge discussions with J. Kofler, T. Jennewein, and N. Langford, help from B. Rauer, and support from EPSRC, QIPIRC, FWF, EC under the Integrated Project Qubit Application, EMALI, and the U.S. Army Research Funded IARPA.

[1] R. Horodecki *et al.*, Rev. Mod. Phys. 81, 865 (2009).
[2] D. M. Greenberger *et al.*, Am. J. Phys. **58**, 1131 (1990).
[3] W. Dür, G. Vidal, and J. I. Cirac, Phys. Rev. A **62**, 062314 (2000).
[4] H. J. Briegel *et al.*, Nature Phys. **5**, 19 (2009).
[5] D. Bouwmeester *et al.*, Phys. Rev. Lett. **82**, 1345 (1999); M. Eibl *et al.*, *ibid.* **90**, 200403 (2003); Z. Zhao *et al.*, Nature (London) **430**, 54 (2004); H. Häffner *et al.*, *ibid.* **438**, 643 (2005); C.-Y. Lu *et al.*, Nature Phys. **3**, 91 (2007); W. Wieczorek *et al.*, Phys. Rev. Lett. **101**, 010503 (2008); W.-B. Gao *et al.*, arXiv:0809.4277.
[6] F. Verstraete *et al.*, Phys. Rev. A **65**, 052112 (2002); L. Chen and Y. X. Chen, *ibid.* **74**, 062310 (2006); L. Lamata *et al.*, *ibid.* **75**, 022318 (2007).
[7] R. H. Dicke, Phys. Rev. **93**, 99 (1954).
[8] G. Tóth, J. Opt. Soc. Am. B **24**, 275 (2007).
[9] A. Sørensen *et al.*, Nature (London) **409**, 63 (2001); J. K. Stockton *et al.*, Phys. Rev. A **67**, 022112 (2003); J. K. Korbicz, J. I. Cirac, and M. Lewenstein, Phys. Rev. Lett. **95**, 120502 (2005); G. Tóth *et al.*, *ibid.* **99**, 250405 (2007); J. Korbicz *et al.*, Phys. Rev. A **74**, 052319 (2006).
[10] C. Thiel *et al.*, Phys. Rev. Lett. **99**, 193602 (2007); J. K. Stockton, R. van Handel, and H. Mabuchi, Phys. Rev. A **70**, 022106 (2004); A. Retzker, E. Solano, and B. Reznik, *ibid.* **75**, 022312 (2007); I. E. Linington and N. V. Vitanov, *ibid.* **77**, 010302(R) (2008).
[11] N. Kiesel *et al.*, Phys. Rev. Lett. **98**, 063604 (2007).
[12] M. Murao *et al.*, Phys. Rev. A **59**, 156 (1999).
[13] V. Scarani *et al.*, Rev. Mod. Phys. **77**, 1225 (2005).
[14] C. H. Bennett *et al.*, Phys. Rev. Lett. **70**, 1895 (1993); A. Karlsson and M. Bourennane, Phys. Rev. A **58**, 4394 (1998).
[15] M. Hillery, V. Bužek, and A. Berthiaume, Phys. Rev. A **59**, 1829 (1999).
[16] A Dicke state of N qubits and k excitations is given by $|D_N^{(k)}\rangle = (C_N^k)^{-1/2} \sum_P |H\rangle^{\otimes k} |V\rangle^{\otimes N-k}$, with C_i^j as the binomial coefficient.
[17] See EPAPS Document No. E-PRLTAO-103-082929. For more information on EPAPS, see http://www.aip.org/pubservs/epaps.html.
[18] S. Campbell, M. S. Tame, and M. Paternostro, arXiv:0903.3939v1 [New J. Phys. (to be published)].
[19] Dephasing affecting $|D_6^{(3)}\rangle$ leads to only $(\sin\theta)^6$ [18].
[20] The LMSs are $\sigma_{x,y,z}^{\otimes 6}$, $[(\sigma_x \pm \sigma_{y,z})/\sqrt{2}]^{\otimes 6}$, $[(\sigma_y \pm \sigma_z)/\sqrt{2}]^{\otimes 6}$, $[(\sigma_{x,y} \pm 2\sigma_z)/\sqrt{5}]^{\otimes 6}$, $[(\sigma_z \pm 2\sigma_{x,y})/\sqrt{5}]^{\otimes 6}$, and $[(\sigma_x \pm \sigma_y \pm \sigma_z)/\sqrt{3}]^{\otimes 6}$.
[21] In the $\sigma_{x,y}$ bases, for instance, $|D_6^{(3)}\rangle$ has an overlap of $\sqrt{5/8}$ with a six-photon GHZ state.
[22] This was independently investigated in W. Wieczorek *et al.*, Phys. Rev. A **79**, 022311 (2009).
[23] The LMSs are $\sigma_{x,y,z}^{\otimes 4}$, $[(\sigma_x \pm \sigma_{y,z})/\sqrt{2}]^{\otimes 4}$, $[(\sigma_y \pm \sigma_z)/\sqrt{2}]^{\otimes 4}$.
[24] O. Gühne *et al.*, Phys. Rev. A **76**, 030305(R) (2007).
[25] M. Horodecki, P. Horodecki, and R. Horodecki, Phys. Rev. A **60**, 1888 (1999).
[26] S. Gaertner *et al.*, Phys. Rev. Lett. **98**, 020503 (2007).

Supplementary Material

Experimental realization of Dicke states of up to six qubits for multiparty quantum networking

R. Prevedel[1], G. Cronenberg[1], M. S. Tame[2], M. Paternostro[2], P. Walther[1,3], M. S. Kim[2], and A. Zeilinger[1,3]
[1]*Faculty of Physics, University of Vienna, Boltzmanngasse 5, A-1090 Vienna, Austria*
[2]*School of Mathematics and Physics, The Queen's University, Belfast, BT7 1NN, UK*
[3]*Institute for Quantum Optics and Quantum Information (IQOQI), Austrian Academy of Sciences, Boltzmanngasse 3, A-1090 Vienna, Austria*
(Dated: June 11, 2009)

A. SIMULATION OF EXPERIMENTAL STATE GENERATION

In this Section we outline the method used to obtain the simulated state ρ_{sim} corresponding to our linear optical setup and provide details of the relevant parameters in the simulation. The effects of higher-order photon emission, fiber-loss and detector inefficiencies are all included in our study. We break the generation stage into four parts: A, B, C and D, as depicted in Fig. 1. At point A, the state per pump pulse produced by collinear type-II spontaneous parametric down-conversion at the BBO crystal can be modeled by the density matrix [1]

$$\rho \simeq \sum_{i\geq 0} p_i \rho_{ii}. \tag{S-1}$$

Here $\rho_{ij} = |i_H\rangle\langle i_H| \otimes |j_V\rangle\langle j_V|$ with i_H (j_V) representing i (j) photons in the output mode of the down-conversion process with H (V) polarization. The p_i's are the probabilities that i photons are emitted into polarization modes H and V. We have neglected any cross terms involving $|i_H\rangle\langle i'_H| \otimes |j_V\rangle\langle j'_V|$ (with $i \neq i', j \neq j'$) in Eq. (S-1), a simplification which will be discussed later on. The value $p_1 = 0.065$ corresponds to the operating regime of our experiment, with $p_i \simeq (p_1)^i$ [1]. Postselection of *six-fold* coincidence events, *i.e.* the detection of six photons, one at either D_{kH} *or* D_{kV} simultaneously for all modes $k = 1$ to 6, allows us to consider a postselected state subspace, where the first three terms in Eq. (S-1) are not present, as they contain less that six photons overall. On the other hand, we cannot be sure that exactly six photons are generated in the setup when a six-fold coincidence occurs, therefore we write the *reduced* state at point A (upon proper renormalization) as

$$\rho_A = \sum_{i\geq 3} p_i^a \rho_{ii}, \tag{S-2}$$

where $p_i^a = (\sum_{i\geq 3} p_i)^{-1} p_i$. We now account for the propagation across the single-mode (SM) fiber shown in Fig. 1. We define η_s as the combined coupling and transmission efficiency of the SM fiber and ρ_{ri} as the states with less than six photons that result upon photon losses from the state ρ_{ii}. In our experiment we have $\eta_s = 0.5$. This leads to the following transformations

$$\begin{aligned}
&\rho_{33} \rightarrow \eta_s^6 \rho_{33} + (1-\eta_s^6)\rho_{r3} \\
&\rho_{44} \rightarrow \eta_s^8 \rho_{44} + 4\eta_s^7(1-\eta_s)(\rho_{34}+\rho_{43}) + 16\eta_s^6(1-\eta_s)^2\rho_{33} \\
&+ 6\eta_s^6(1-\eta_s)^2(\rho_{24}+\rho_{42}) + (1-21\eta_s^8+48\eta_s^7-28\eta_s^6)\rho_{r4}.
\end{aligned} \tag{S-3}$$

By taking into account all possible ways to lose photons, it is easy to get similar transformations for states up to ρ_{nn}. Postselecting out the ρ_{ri} terms, as they do not contribute to six-fold coincidences, we obtain the reduced state

$$\rho' = \sum_{i\geq 3} p_{ii}\rho_{ii} + \sum_{i\neq j|\ i+j\geq 6} p_{ij}\rho_{ij}, \tag{S-4}$$

where explicit expressions for p_{ij} can be easily obtained using Eqs. (S-3). For example, we have $p_{33} = (p_3^a\eta_s^6 + 16p_4^a\eta_s^6(1-\eta_s)^2 + \dots)$, $p_{34} = p_{43} = (4p_4^a\eta_s^7(1-\eta_s) + \dots)$, $p_{44} = (p_4^a\eta_s^8 + \dots)$, $p_{24} = p_{42} = (6p_4^a\eta_s^6(1-\eta_s)^2 + \dots)$ and similarly for states up to ρ_{nn}. Renormalizing, we have the reduced state at point B (see Fig. 1)

$$\rho_B = \sum_{i\geq 3} p_{ii}^b \rho_{ii} + \sum_{i\neq j|\ i+j\geq 6} p_{ij}^b \rho_{ij}, \tag{S-5}$$

where $p_{ij}^b = (\sum_{ij} p_{ij})^{-1} p_{ij}$. Next, we account for the effects of the 1-to-3 fiber coupler and beamsplitters on the overall photonic state by considering a unitary operation U_g, whose explicit form is not necessary for the present discussion. Applying it to ρ_B gives the state

$$\rho'' = \sum_{i\geq 3} \tilde{p}_{ii}\tilde{\rho}_{ii} + \sum_{i\neq j|\ i+j\geq 6} \tilde{p}_{ij}\tilde{\rho}_{ij}, \tag{S-6}$$

where $\tilde{\rho}_{ij} = U_g \rho_{ij} U_g^\dagger$. We then postselect out from the subspace spanned by each $\tilde{\rho}_{ij}$ the terms that can only contribute to six-fold coincidences. Renormalizing, we have the reduced state at point C in Fig. 1 given by

$$\rho_C = \sum_{i\geq 3} p_{ii}^c \rho_{ii}^c + \sum_{i\neq j|\ i+j\geq 6} p_{ij}^c \rho_{ij}^c, \tag{S-7}$$

where $p_{ij}^c = [\tilde{p}_{ij} \sum_{ij} (\mathrm{Tr}(\rho_{ij}^c)/\tilde{p}_{ij})]/\mathrm{Tr}(\rho_{ij}^c)$. Here we have $\rho_{33}^c = |D_6^{(3)}\rangle\langle D_6^{(3)}|$, with $|D_6^{(3)}\rangle$ the desired pure Dicke

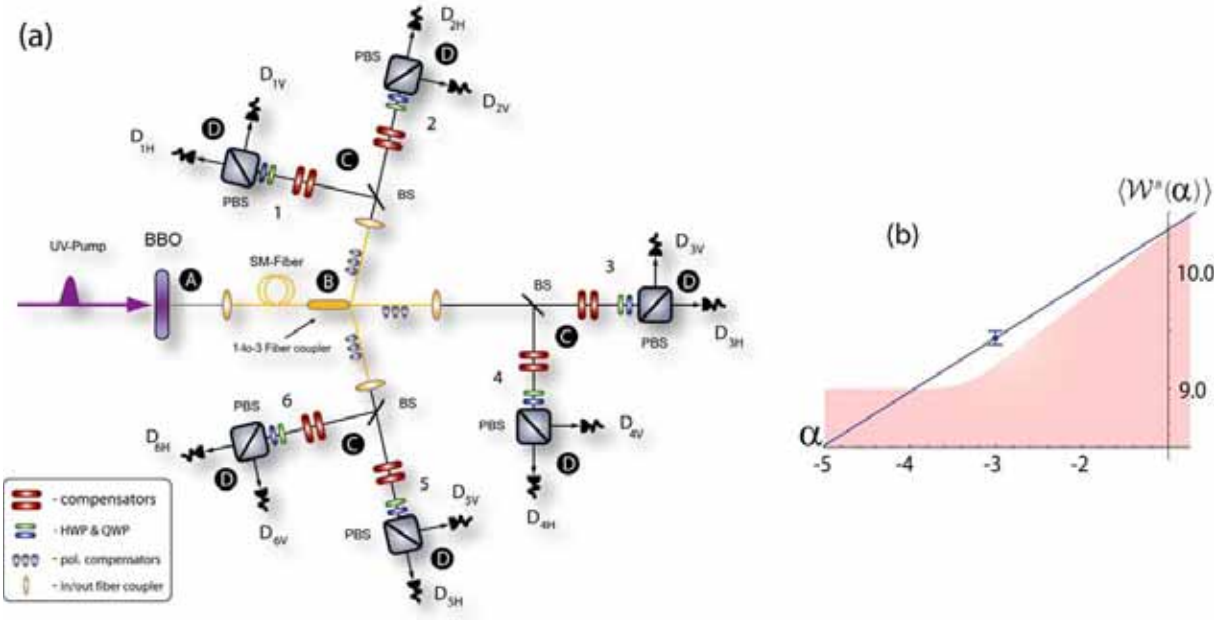

FIG. 1: **(a)**: Setup for the generation of the six-photon Dicke state $|D_6^{(3)}\rangle$. Photons are probabilistically distributed into modes $1,..,6$ via a 1-to-3 fiber coupler, followed by $50:50$ BSs. The simulation is broken down into four parts: A, B, C and D, see text for details. **(b)**: Biseparability region (shaded) for $\langle \mathcal{W}^s(\alpha)\rangle_{bs}$ and experimental point (predicted line) for $\langle \mathcal{W}^s(\alpha)\rangle_{\varrho_6^{(3)}}$.

state. The additional terms in Eq. (S-7) are a result of higher-order photon emission ($i,j>3$ in Eq. (S-1)) and fiber loss up to point C.

We now briefly summarize the final stage, from point C to the detectors at point D. For each mode $k=1\rightarrow 6$, the outputs kH and kV of the polarizing beamsplitter (PBS) are coupled into multimode fibers with efficiency $\eta_m=0.9$ and sent to detectors with efficiency $\eta_d=0.4$. Here, for simplicity we have assumed all efficiencies are the same for each output mode of the PBSs. We lump the efficiencies together, giving a combined efficiency of $\eta_D=\eta_m\eta_d$. For each term in Eq. (S-7) we take the elements $|n_H\rangle_k\langle m_H| \equiv (n!m!)^{-1/2}(\hat{a}_{kH}^\dagger)^n|0\rangle_k\langle 0|(\hat{a}_{kH})^m$ for each mode kH, where $\hat{a}_{kH}^\dagger$ ($\hat{a}_{kH}$) is the creation (annhilation) operator for the mode, and use the standard beamsplitter picture to model photon losses at a detector [2]: $\hat{a}_{kH}^\dagger \rightarrow \eta_D^{1/2}\hat{a}_{kH'}^\dagger + i(1-\eta_D)^{1/2}\hat{a}_{kH''}^\dagger$. A similar procedure is performed on the kV modes. Here kH' (kH'') represents the detected (loss) mode. The loss modes kH'' and kV'' do not lead to six-fold coincidences at the detector modes kH' and kV' and are therefore traced out. We relabel the detector modes $kH'\rightarrow kH$ ($kV'\rightarrow kV$) for convenience, so that they correspond to those of Fig. 1. Upon renormalization, the detected state at point D is then given by

$$\rho_D = \rho_{sim} = \mathcal{N}^{-1}[\sum_{i\geq 3} p_{ii}^d \rho_{ii}^c + \sum_{i\neq j|\ i+j\geq 6} p_{ij}^d \rho_{ij}^c], \quad \text{(S-8)}$$

where $\mathcal{N}$ is a normalization given by the sum of the trace of the states appearing within the square bracket. The density matrix for ρ_{sim}, taking into account higher-order emissions up to four-pairs, is shown in Fig. 2 **(a)** along with its normalized populations in the $|+/-\rangle$, $|L/R\rangle$ and $|H/V\rangle$ bases in **(b)**, **(c)** and **(e)** respectively. As ρ_{sim} contains states which have higher photon occupation number than one, it spans a Hilbert-space sector which is larger than the 2^6-dimensional space of $|D_6^{(3)}\rangle$ (defined by the polarization degrees of freedom H and V). In our model, the detectors are taken to not be photon-number resolving and we project down onto the 2^6-dimensional space via the transforms $|n_H\rangle_k\langle m_H| \rightarrow |1_H\rangle_k\langle 1_H|$, $\forall\ m,n>1$ and similarly for the kV modes. Increased agreement of ρ_{sim} with the experimental state $\rho_{D_6^{(3)}}$ may be found with the addition of corrections due to five-pair emissions and the inclusion of cross terms in Eq. (S-1). However this is at the expense of the simulation time required. At present it was not feasible to quantify the impact of these smaller contributions. However, the current state fidelity between the desired Dicke state and ρ_{sim}, given by $F_{D_6^{(3)}}=0.61$, is very close to the value that we have experimentally reconstructed (0.56 ± 0.02, see main Letter). In addition, the multi-photon correlation patterns show good agreement with the data.

B. SCALABILITY OF SETUP

Count rate.- In principle our setup is scalable in terms

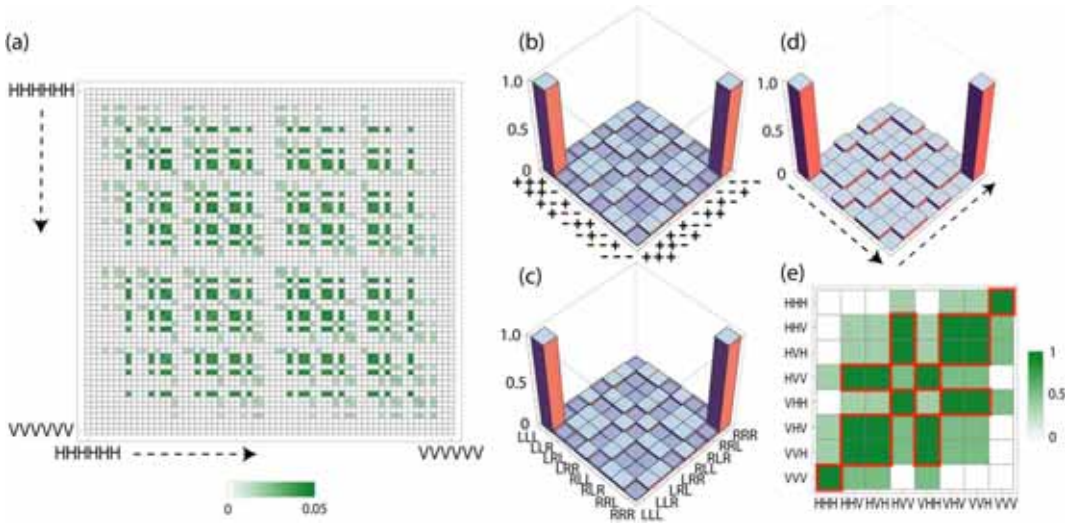

FIG. 2: Analysis of the simulated six-photon Dicke state ρ_{sim}. **(a)** Density matrix for ρ_{sim}. **(b)**, **(c)** and **(e)**: Six-fold coincidences (normalized) for photons measured in $|\pm\rangle = (|H\rangle \pm |V\rangle)/\sqrt{2}$, $|L/R\rangle = (|H\rangle \pm i\,|V\rangle)/\sqrt{2}$ and $|H/V\rangle$. **(d)**: Ideal populations for panels **(b)** and **(c)**.

of the count rate. For instance, by increasing the brightness of the UV-pump beam one can increase the rate of six-photon coincidences in our experimental setup. In this scenario it is important to note that by using an additional network of beamsplitters and detectors, in a so-called split-and-detect strategy [3], noise from the resulting higher-order excitations could be postselected out in a straightforward manner, so that only genuine six-photon down-conversion events are observed. Any additional noise will be due to fiber coupling/transmission losses and detector inefficiencies, as outlined in Section A. In this sense, our setup is ultimately limited by technological challenges, such as reducing photon losses and increasing detector efficiencies. In passing, we also note that the absence of temporal/spatial mode-mismatch makes our setup suitable for studying the effects of unwanted multi-pair emissions in multiphoton-state generation.

Dimension.- In principle our setup is also scalable in terms of the dimension of the generated Dicke state. For instance, by replacing the 1-to-3 fiber coupler in Fig. 1 with a 1-to-n fiber coupler, or an equivalent linear optical circuit using an array of beamsplitters, the setup can easily be generalized to the production of $2n$-qubit Dicke states $|D_{2n}^{(n)}\rangle$. Here the circuit after point C (on the top mode) is replicated at the output of each of the n-modes of the 1-to-n fiber coupler. Note however that the success probability of observing 2 photons in each of the output modes of the fiber coupler decreases exponentially with n. The brightness of the UV-pump beam should then be increased in order to achieve n-pair photon emission rates that lead to $2n$-fold photon coincidence rates sufficient for a given experimental implementation.

C. COLLECTIVE SPIN-BASED WITNESS

In Fig. 1 **(b)** we show the biseparability region (shaded) for $\langle \mathcal{W}^s(\alpha)\rangle_{bs}$ and experimental point (predicted line) for $\langle \mathcal{W}^s(\alpha)\rangle_{\varrho_6^{(3)}}$. Here $\mathcal{W}^s(\alpha) = J_x^2 + J_y^2 + \alpha J_z^2$ with $J_i = \frac{1}{2}\sum_{k=1}^{N} \sigma_i^{(k)}$ $(i = x, y, z)$ as collective-spin operators of N qubits with label k and $\sigma_i^{(k)}$ denotes the i-Pauli operator.

[1] M. H. Rubin, D. N. Klyshko, Y. H. Shih and A. V. Sergienko, Phys. Rev. A, **50**, 5122 (1994); Y. Shih, Rep. Prog. Phys. **66**, 1009 (2003).

[2] R. Loudon, *The Quantum Theory of Light*, 3rd Ed., Oxford University Press, Oxford (2000).

[3] S. Song, C. M. Caves and B. Yurke, Phys. Rev. A **41**, R5261 (1990); P. Kok and S. L. Braunstein, Phys. Rev. A **63**, 033812 (2001).

Appendix B

Outcome matrices

Here, the experimentally direct accessible coincidence pattern are shown for the different LMS for the six-, as well as the five- and four-photon states. To read the figures, the local measurement settings can be found in Table B.1. For example Figure B.2(b) shows the ideal pattern for a $D_5^{(3)}$ which is measured in $X^{\otimes 5}$ as the table indicates $b \to X$ for each qubit. Furthermore the identification $0 \to |+\rangle, 1 \to |-\rangle$ has to be done in that example. Any exceptions are stated in the caption.

a	b	c	d	e	f
Z	X,Y	X ± Y ± Z	X ± Z	X ± 2Z	Z ± 2X
	X ± Y	X ± Y ∓ Z	Y ± Z	Y ± 2Z	Z ± 2Y

Table B.1: This table lists which LMS give the outcomes in Figures B.1, B.2 and B.3. Each LMS is again understood for each qubit, e.g. $Z^{\otimes 6}$.

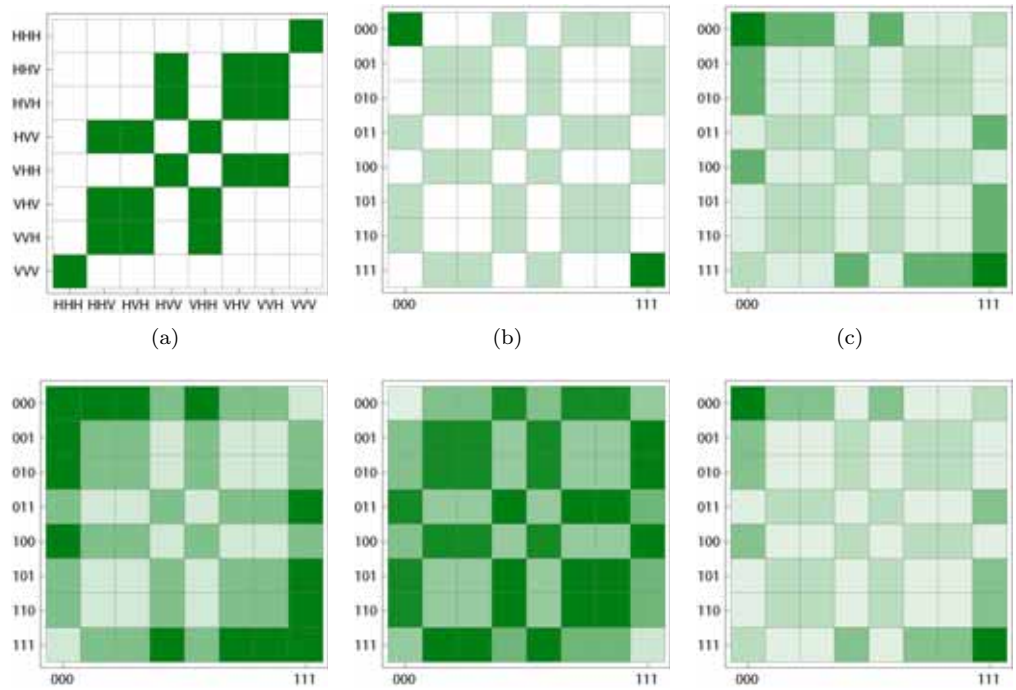

(a) (b) (c)

(d) (e) (f)

Figure B.1: Showing the ideal coincidence patterns for the LMS of the six-qubit Dicke state $D_6^{(3)}$. The correspondence to the bases can be seen from Table B.1.

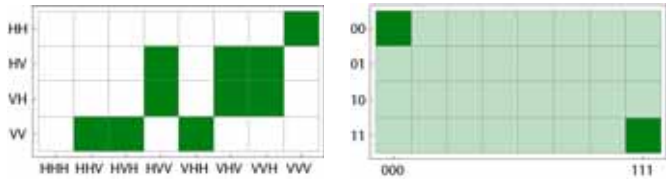

(a) (b)

Figure B.2: Showing the ideal coincidence patterns for the LMS of the five-qubit Dicke state $D_5^{(3)}$. The correspondence to the bases can be seen from Table B.1.

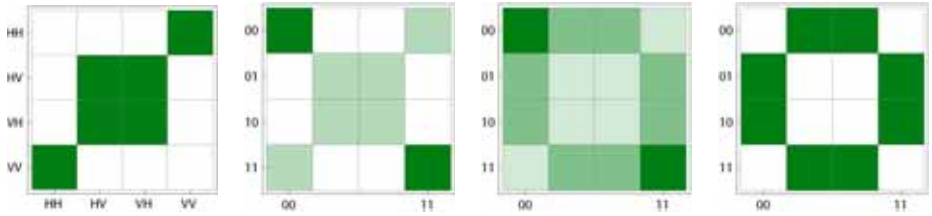

(a) (b) (c) (d)

Figure B.3: Showing the ideal coincidence patterns for the LMS of the four-qubit Dicke state $D_4^{(2)}$. The correspondence to the bases can be seen from Table B.1. The three pattern of the five LMS for the GHZ state are the same except for the Y and Z bases, which can be seen in (d). (So (a) was never recorded for the GHZ state.)

Appendix C

Exemplary code

Here is a short extract form the MatLab code used for the numerical simulation. It is not executable on its own but should only give a feeling and insight into how the various components were implemented. It utilises and extends the online available *Quantum Optics and Computation Toolbox*.

The Fock space dimensionality is set to 9 in the presented code. The code is structured in such a way that the action of wave plates and beam splitters is defined in its first part. Then, the initial state is produced through applying the SPDC Hamilitonian to the vacuum state. Afterwards the different coupling efficiencies into the fibre are implemented. The spatial mode is then split up into three modes, with the probability of one sixth for the first two modes. After applying the wave plates onto the photons in the first two modes, their detection, with the corresponding efficiency, is realised through multiplying with a detection matrix and tracing the modes out. The desired coincidence pattern is defined by this detection matrix which consists of detection and non-detection projectors. The same procedure is applied for the next step where the remaining modes are split again and detected. By modifying the detection matrix, all post-selected events can be obtained with the possibility of varying all parameters according to one's desire.

Listing C.1: Dicke Simulation

```
N=10; % Fock space dimension +1

% load standard functions and operators
standard_defintions_qo_toolbox;

%% Definitions
% Detectors
[bd_proj bd_unproj]=BucketDetector(N, deteffc);

% SPDC process with squeezing parameter epsilon:
H_chi2=(tensor(a,a)+tensor(a',a'))*epsilon;
U_chi2=expm(-1i*H_chi2);
```

```
% Beam splitter (66:33)
eta = acos(sqrt(1/3));
H_bsG = (tensor(a,a') + tensor(a',a))*eta;
U_bsG = expm(-1i*H_bsG);

% Fibre loss different for H and V
% Simulated like a beamsplitter
etaH = acos(sqrt(couplingeffH));
H_bsFLH = (tensor(a,a') + tensor(a',a))*etaH;
U_bsFLH = expm(-1i*H_bsFLH);

etaV = acos(sqrt(couplingeffV));
H_bsFLV = (tensor(a,a') + tensor(a',a))*etaV;
U_bsFLV = expm(-1i*H_bsFLV);


%% Define Input state here
% SPDC states with |H1,V1>
spdc_state=tensor(U_chi2*tensor(vacc,vacc));


% Simulate fibre loss
% Extend Hilbertspace for fibre loss and rearrange to |H1,H2,V1,V2>
intermediate_state=permute(tensor(spdc_state,vacc,vacc),[1,3,2,4]);
intermediate_state=tensor(U_bsFLH,U_bsFLV)*intermediate_state;
% Rearrange to |H1,V1,H2,V2>
intermediate_state=permute(intermediate_state,[1,3,2,4]);
% Tracing out the losses leaves us with |H1,V1>
initial_state=ptrace(intermediate_state,[1 2]);

%from here on no state vector but density matrix

% Apply 66:33 beam splitter to all modes 1 with 2
full_state=permute(tensor(initial_state,vacc*vacc',vacc*vacc')
    ,[1,3,2,4]);
full_state=tensor(U_bsG,U_bsG)'*full_state*tensor(U_bsG,U_bsG);
% permute from |H1,H2,V1,V2> to |H2,V2,H1,V1>
full_state=permute(full_state,[2 4 1 3]);


%% First arm

% Extend Hilbertspace to |H2,V2,H1,V1,H3,V3>
full_state=tensor_high_n(full_state,vacc*vacc',vacc*vacc');
% apply 50:50 beam splitter on H1,H3,V1,V3
U_bs_multi=permute(tensor(U_bs,U_bs),[1 3 2 4]);
U_bs_multi=tensor_high_n(ida,ida,U_bs_multi);
full_state=U_bs_multi'*full_state*U_bs_multi;
```

```
% Measurement on |H2,V2,H1,V1,H3,V3> ie for of U_proj_first2

% Waveplates
U_wp=tensor_high_n(ida,ida, U_HWPG(N,WPangles{1}(2))*U_QWPG(N,WPangles{1}(1)), U_HWPG(N,WPangles{2}(2))*U_QWPG(N,WPangles{2}(1)));
full_state=U_wp'*full_state*U_wp;

% perform partial trace
full_state=U_proj_first2*full_state;

next_state_13=ptrace_high_n(N,full_state);
next_state_13=qo(next_state_13,{[N; N],[N ;N]});


% Extend Hilbertspace for 3rd row of BS, and rearrange from |H2,V2> -> |H2,H4,V2,V4>
next_state_13=tensor(next_state_13,vacc*vacc',vacc*vacc');
next_state_13=permute(next_state_13,[1 3 2 4]);

% Second row of Beamsplitter
next_state_13=tensor(U_bs,U_bs)'*next_state_13*tensor(U_bs,U_bs);

% Exend hilbert space with vacuum in modes H5, V5
next_state_13=permute(next_state_13,[1 3 2 4]);
next_state_13=tensor_high_n(next_state_13,vacc*vacc',vacc*vacc');


U_bs_multi=permute(tensor(U_bs,U_bs),[1 3 2 4]);
U_bs_multi=tensor_high_n(ida,ida,U_bs_multi);

next_state_13=U_bs_multi'*next_state_13*U_bs_multi;


% project onto modes 4 and 5

% Waveplates
U_wp=tensor_high_n(ida,ida,U_HWPG(N,WPangles{3}(2))*U_QWPG(N,WPangles{3}(1)),U_HWPG(N,WPangles{4}(2))*U_QWPG(N,WPangles{4}(1)));
next_state_13=U_wp'*next_state_13*U_wp;

% project onto 4,5 - |H2,V2,H4,V4,H5,V5>
next_state_13=U_proj_second2*next_state_13;

next_state_1345=ptrace_high_n(N,next_state_13);
next_state_1345=qo(next_state_1345,{[N; N],[N ;N]});

%% Third arm
% only H2,V2 left

% add H6,V6 and arrange to H2,H6,V2,V6
next_state_1345=tensor(next_state_1345,vacc*vacc',vacc*vacc');
```

```
111 next_state_1345=permute(next_state_1345,[1 3 2 4]);

    % Apply 50:50 Beamsplitter
    U_bs_last=tensor(U_bs,U_bs);
    next_state_1345=U_bs_last'*next_state_1345*U_bs_last;
116 % permute back to H2,V2,H6,V6
    next_state_1345=permute(next_state_1345,[1 3 2 4]);

    % Waveplates
    U_wp=tensor(U_HWPG(N,WPangles{5}(2))*U_QWPG(N,WPangles{5}(1)),U_HWPG(N,
        WPangles{6}(2))*U_QWPG(N,WPangles{6}(1)));
121 next_state_1345=U_wp'*next_state_1345*U_wp;

    % Probability obtained
    prob=trace(U_proj_third2*next_state_1345);
```

Bibliography

[1] R. P. Feynman, *"Simulating physics with computers,"* International Journal of Theoretical Physics pp. 467–488 (1982). [cited at p. 1]

[2] R. Landauer, *"Information is Physical,"* Physics Today **44,** 23–29 (1991). [cited at p. 1]

[3] J. J. Sakurai, *Modern Quantum Mechanics (2nd Edition)* (Addison Wesley, 1994). [cited at p. 2]

[4] M. A. Nielsen and I. L. Chuang, *Quantum Computation and Quantum Information* (Cambridge University Press, 2000), p. 675 S. [cited at p. 2, 3, 4, 7]

[5] C. K. Hong, Z. Y. Ou, and L. Mandel, *"Measurement of subpicosecond time intervals between two photons by interference,"* Phys. Rev. Lett. **59,** 2044–2046 (1987). [cited at p. 4]

[6] P. Kok, W. J. Munro, K. Nemoto, T. C. Ralph, J. P. Dowling, and G. J. Milburn, *"Linear optical quantum computing with photonic qubits,"* Reviews of Modern Physics **79,** 135 (2007). [cited at p. 4, 15, 17]

[7] N. Langford, Ph.D. thesis, University of Queensland, 2007. [cited at p. 5]

[8] E. Schrödinger, *"Die gegenwärtige Situation in der Quantenmechanik,"* Naturwissenschaften **23,** 844–849 (1935). [cited at p. 6]

[9] A. Einstein, B. Podolsky, and N. Rosen, *"Can Quantum-Mechanical Description of Physical Reality Be Considered Complete?,"* Phys. Rev. **47,** 777–780 (1935). [cited at p. 6]

[10] J. Bell, *"On the Einstein-Podolsky-Rosen paradox,"* Physics 1 pp. 195–200 (1964). [cited at p. 6]

[11] W. Dür, G. Vidal, and J. I. Cirac, *"Three qubits can be entangled in two inequivalent ways,"* Phys. Rev. A **62,** 062314 (2000). [cited at p. 8]

[12] A. Zeilinger, M. A. Horne, and D. M. Greenberger, *NASA Conf. Publ. 3135* (1997). [cited at p. 8]

[13] D. M. Greenberger, M. A. Horne, and A. Zeilinger, *"Going beyond Bell's Theorem,"* in *Bell's Theorem, Quantum Theory, and Conceptions of the Universe*, M. Kafatos, ed., (Kluwer, Dordrecht, 1989), p. 69. [cited at p. 8]

[14] D. M. Greenberger, M. A. Horne, A. Shimony, and A. Zeilinger, *"Bell's theorem without inequalities,"* American Journal of Physics **58,** 1131–1143 (1990). [cited at p. 8]

[15] D. Bouwmeester, J.-W. Pan, M. Daniell, H. Weinfurter, and A. Zeilinger, *"Observation of Three-Photon Greenberger-Horne-Zeilinger Entanglement,"* Phys. Rev. Lett. **82,** 1345–1349 (1999). [cited at p. 8, 25]

[16] F. Verstraete, J. Dehaene, B. De Moor, and H. Verschelde, *"Four qubits can be entangled in nine different ways,"* Phys. Rev. A **65,** 052112 (2002). [cited at p. 9]

[17] L. Chen and Y.-X. Chen, *"Classification of GHZ-type, W-type, and GHZ-W-type multi-qubit entanglement,"* Physical Review A (Atomic, Molecular, and Optical Physics) **74,** 062310 (2006). [cited at p. 9]

[18] L. Lamata, J. León, D. Salgado, and E. Solano, *"Inductive entanglement classification of four qubits under stochastic local operations and classical communication,"* Physical Review A (Atomic, Molecular, and Optical Physics) **75,** 022318 (2007). [cited at p. 9]

[19] D. Bruss, *"Characterizing entanglement,"* Journal of Mathematical Physics **43,** 4237–4251 (2002). [cited at p. 10]

[20] F. Mintert, A. R. Carvalho, M. Kus, and A. Buchleitner, *"Measures and dynamics of entangled states,"* Physics Reports **415,** 207 – 259 (2005). [cited at p. 10]

[21] J. K. Korbicz, J. I. Cirac, and M. Lewenstein, *"Spin Squeezing Inequalities and Entanglement of N Qubit States,"* Phys. Rev. Lett. **95,** 120502 (2005). [cited at p. 11]

[22] M. Kitagawa and M. Ueda, *"Squeezed spin states,"* Phys. Rev. A **47,** 5138–5143 (1993). [cited at p. 11]

[23] W. Demtröder, *Experimentalphysik 2: Elektrizität und Optik*, 5., überarb. u. erw. ed. (Springer, 2009). [cited at p. 13]

[24] B. E. A. Saleh and M. C. Teich, *Fundamentals of Photonics: Second Edition* (Published by John Wiley & Son, Hoboken, NJ, USA., 2007). [cited at p. 13, 26]

[25] R. Prevedel, Master's thesis, University of Vienna, 2005. [cited at p. 14, 32]

[26] E. Knill *et al.*, *"A scheme for efficient quantum computation with linear optics,"* Nature **409,** 46–52 (2001). [cited at p. 15]

[27] A. Zeilinger, *"General properties of lossless beam splitters in interferometry,"* Am. J. Phys. **49,** 882 (1981). [cited at p. 17]

[28] J.-W. Pan, C. Simon, C. Brukner, and A. Zeilinger, *"Entanglement purification for quantum communication,"* Nature **410,** 1067–1070 (2001), 10.1038/35074041. [cited at p. 18]

[29] D. C. Burnham and D. L. Weinberg, *"Observation of Simultaneity in Parametric Production of Optical Photon Pairs,"* Phys. Rev. Lett. **25,** 84–87 (1970). [cited at p. 19]

[30] D. Bouwmeester, A. Ekert, and A. Zeilinger, *The physics of quantum information: quantum cryptography, quantum teleportation, quantum computation* (Springer-Verlag, London, UK, 2000). [cited at p. 19]

[31] P. G. Kwiat, K. Mattle, H. Weinfurter, A. Zeilinger, A. V. Sergienko, and Y. Shih, *"New High-Intensity Source of Polarization-Entangled Photon Pairs,"* Phys. Rev. Lett. **75,** 4337–4341 (1995). [cited at p. 19]

[32] M. H. Rubin, D. N. Klyshko, Y. H. Shih, and A. V. Sergienko, *"Theory of two-photon entanglement in type-II optical parametric down-conversion,"* Phys. Rev. A **50,** 5122–5133 (1994). [cited at p. 19]

[33] G. Weihs, Ph.D. thesis, University of Vienna, 1998. [cited at p. 22]

[34] M. Eibl, S. Gaertner, M. Bourennane, C. Kurtsiefer, M. Żukowski, and H. Weinfurter, *"Experimental Observation of Four-Photon Entanglement from Parametric Down-Conversion,"* Phys. Rev. Lett. **90,** 200403 (2003). [cited at p. 25]

[35] Z. Zhao, Y.-A. Chen, A.-N. Zhang, T. Yang, H. Briegel, and J.-W. Pan, *"Experimental demonstration of five-photon entanglement and open-destination teleportation,"* Nature **430,** 54–58 (2004), 10.1038/nature02643. [cited at p. 25]

[36] W.-B. Gao, C.-Y. Lu, X.-C. Yao, P. Xu, O. Gühne, A. Goebel, Y.-A. Chen, C.-Z. Peng, Z.-B. Chen, and J.-W. Pan, *"Experimental demonstration of a hyper-entangled ten-qubit Schrödinger cat state,"* (2008). [cited at p. 25]

[37] H. Häffner *et al.*, *"Scalable multiparticle entanglement of trapped ions,"* Nature **438,** 643–646 (2005), 10.1038/nature04279. [cited at p. 25]

[38] P. Walther, K. J. Resch, T. Rudolph, E. Schenck, H. Weinfurter, V. Vedral, M. Aspelmeyer, and A. Zeilinger, *"Experimental one-way quantum computing,"* Nature **434,** 169–176 (2005). [cited at p. 25]

[39] C.-Y. Lu, X.-Q. Zhou, O. Gühne, W.-B. Gao, J. Zhang, Z.-S. Yuan, A. Goebel, T. Yang, and J.-W. Pan, *"Experimental entanglement of six photons in graph states,"* Nat Phys **3,** 91–95 (2007), 10.1038/nphys507. [cited at p. 25]

[40] R. Raussendorf and H. J. Briegel, *"A One-Way Quantum Computer,"* Phys. Rev. Lett. **86,** 5188–5191 (2001). [cited at p. 25]

[41] M. Hein, J. Eisert, and H. J. Briegel, *"Multiparty entanglement in graph states,"* Phys. Rev. A **69,** 062311 (2004). [cited at p. 25]

[42] N. Kiesel, C. Schmid, G. Tóth, E. Solano, and H. Weinfurter, *"Experimental Observation of Four-Photon Entangled Dicke State with High Fidelity,"* Physical Review Letters **98,** 063604 (2007). [cited at p. 25, 54, 58]

[43] R. H. Dicke, *"Coherence in Spontaneous Radiation Processes,"* Phys. Rev. **93,** 99 (1954). [cited at p. 25]

[44] V. G. Dmitriev, G. G. Gurzadyan, and D. N. Nikogosyan, *Handbook of Nonlinear Optical Crystals* (Springer-Verlag Berlin, 1991). [cited at p. 27, 28]

[45] S. Cova, M. Ghioni, A. Lacaita, C. Samori, and F. Zappa, *"Avalanche photodiodes and quenching circuits for single-photon detection,"* Appl. Opt. **35,** 1956–1976 (1996). [cited at p. 32]

[46] T. Jennewein, Master's thesis, Universität Innsbruck, 1997. [cited at p. 32]

[47] C. Schmid, Master's thesis, Ludwig-Maximilians-Universität München, 2004. [cited at p. 35, 45]

[48] S. M. Tan, *"A Computational Toolbox for Quantum and Atomic Optics,"*. [cited at p. 40]

[49] M. Born and E. Wolf, *Principles of Optics* (London: Pergamon Press, 1959, 1959). [cited at p. 45]

[50] S. Campbell, M. S. Tame, and M. Paternostro, *"Characterizing multipartite symmetric Dicke states under the effects of noise,"* arXiv:0903.3939 (2009). [cited at p. 49]

[51] G. Toth, W. Wieczorek, R. Krischek, N. Kiesel, P. Michelberger, and H. Weinfurter, *"Practical methods for witnessing genuine multi-qubit entanglement in the vicinity of symmetric states,"* arXiv:0903.3910 (2009). [cited at p. 49]

[52] W. Wieczorek, R. Krischek, N. Kiesel, P. Michelberger, G. Toth, and H. Weinfurter, *"Experimental entanglement of a six-photon symmetric Dicke state,"* arXiv:0903.2213 (2009). [cited at p. 49]

[53] O. Gühne, C.-Y. Lu, W.-B. Gao, and J.-W. Pan, *"Toolbox for entanglement detection and fidelity estimation,"* Physical Review A (Atomic, Molecular, and Optical Physics) **76,** 030305 (2007). [cited at p. 56, 57]

[54] C. H. Bennett, G. Brassard, C. Crépeau, R. Jozsa, A. Peres, and W. K. Wootters, *"Teleporting an unknown quantum state via dual classical and Einstein-Podolsky-Rosen channels,"* Phys. Rev. Lett. **70,** 1895–1899 (1993). [cited at p. 57]

[55] A. Karlsson and M. Bourennane, *"Quantum teleportation using three-particle entanglement,"* Phys. Rev. A **58,** 4394–4400 (1998). [cited at p. 57]

[56] W. K. Wootters and W. H. Zurek, *"A single quantum cannot be cloned,"* Nature **299,** 802–803 (1982). [cited at p. 57]

[57] M. Horodecki, P. Horodecki, and R. Horodecki, *"General teleportation channel, singlet fraction, and quasidistillation,"* Phys. Rev. A **60,** 1888–1898 (1999). [cited at p. 58]

[58] V. Scarani, S. Iblisdir, N. Gisin, and A. Acín, *"Quantum cloning,"* Rev. Mod. Phys. **77,** 1225–1256 (2005). [cited at p. 58]

[59] M. Murao, D. Jonathan, M. B. Plenio, and V. Vedral, *"Quantum telecloning and multiparticle entanglement,"* Phys. Rev. A **59,** 156–161 (1999). [cited at p. 58]

[60] R. Cleve, D. Gottesman, and H.-K. Lo, *"How to Share a Quantum Secret,"* Phys. Rev. Lett. **83,** 648–651 (1999). [cited at p. 60]

[61] M. Hillery, V. Bužek, and A. Berthiaume, *"Quantum secret sharing,"* Phys. Rev. A **59,** 1829–1834 (1999). [cited at p. 60, 61]

[62] S. Gaertner, C. Kurtsiefer, M. Bourennane, and H. Weinfurter, *"Experimental Demonstration of Four-Party Quantum Secret Sharing,"* Physical Review Letters **98,** 020503 (2007). [cited at p. 61]

List of Figures

List of Tables